NUMERICAL STUDIES FOR GASOLINE PARTICULATE FILTER

PERFORMANCE IMPROVEMENT

A Dissertation

by

PENGZE YANG

Submitted to the Office of Graduate and Professional Studies of
Texas A&M University
in partial fulfillment of the requirements for the degree of

DOCTOR OF PHILOSOPHY

Chair of Committee,	Andrea Strzelec
Co-Chair of Committee,	Michael Pate
Committee Members,	David Staack
	Prabir Daripa
Head of Department,	Andreas Polycarpou

May 2019

Major Subject: Mechanical Engineering

ABSTRACT

The improvement in brake thermal efficiency of Gasoline Direct Injection (GDI) engines is accompanied by a significant increase in Particulate Matter (PM) and Particulate Number (PN) emissions as compared to (multi)Port Fuel Injected (PFI) engines. GDI-specific particulate filters (GPFs) with high filtration efficiency and low backpressure are required to meet the stringent PM/PN regulations (Manuscript #1). A 2-D GPF wall filtration model is created to determine the effects of pore size and distribution on the interdependent performance parameters of filtration efficiency and backpressure. Simulation results show a nonlinear change in filtration efficiency as the pore size distribution tightens and determines an optimal pore size distribution, by controlling the quantity of small size (less than $10 \mu m$) pores. Simulation results also inspire a novel filtration wall design with small pores comprising the top 40% of the wall layers and larger pores on bottom 60%. The model predicts that such a wall would result in an 8% increase in filtration efficiency at an expanse of 17.5% pressure drop increase (Manuscript #2). Further work modifies the GPF filtration model by moving away from the traditional unit collector model, to the proposed "throat unit collector" model, to better mimic the microstructure characteristics of GPFs. The throat unit collector model demonstrates its capability of predicting the filtration efficiency of blank sample GPFs accurately and simulating filtration efficiency change due to pore bridging (Manuscript #3). Finally, research on washcoating and ash-driven GPF wall heterogeneity effects on GPF performance was done using a 3D GPF model with particle tracking capability. A User Defined Function (UDF) was implemented to define and update the GPF wall properties and resolve the local particle filtration efficiency. The simulation results indicate the uniform washcoating shows the most promising performance with respect to the filtration efficiency and pressure drop. The

model also suggests that pre-loading an ash cake is one way to achieve a balance between high filtration efficiency and low pressure drop (Manuscript #4), as seen in experimental results in the literature.

ACKNOWLEDGEMENTS

NOMENCLATURE

a	pore size on horizontal direction
b	pore size on vertical direction
a'	side length of throat unit collector cuboid
b'	height of throat unit collector cuboid
d	"circular obstacle" diameter
D	cavity diameter
E	total wall filtration efficiency
k	wall permeability
l	interception length scale
n	number of obstacle layers
P	flow pressure
S	source term
t	GPF wall thickness
u	flow velocity
w	wall thickness
β	Forchheimer coefficient
ε	wall porosity
ε_0	wall porosity before washcoating
η	single collector efficiency
η'	single collector efficiency counting the bridging
μ	channel flow viscosity
ρ	channel flow density
σ	flow shear stress
d_c	unit collector diameter

d_{c0}	unit collector diameter before washcoating
d_P	pore size
$\hat{d}_P$	mean pore size
$\hat{E}$	averaged filtration efficiency counting the obstacle randomness
E_D	Brownian diffusion filtration term
E_I	impaction filtration term
E_R	interception filtration term
k_0	wall permeability before washcoating
k_e	equivalence wall permeability
N_i	particle deposition at zone i
N_{max}	max particle deposition
$N_{injected}$	number of particles injected
$N_{trapped}$	number of particles trapped
u_{wi}	wall velocity at zone i
$u_{w\max}$	max wall velocity
V_{cell}	particle loading on single unit collector in previous time step

CONTRIBUTORS AND FUNDING SOURCES

TABLE OF CONTENTS

LIST OF FIGURES

xiii

LIST OF TABLES

CHAPTER I

INTRODUCTION

Gasoline Direct Injection (GDI) engine operation is essentially a hybridization of (multi)Port Fuel Injection (PFI) and diesel engine operation. It combines direct in-cylinder fuel injection and spark ignition technology together, to achieve high fuel efficiency and low emission simultaneously. For a GDI engine, during the compression and power cycle, the stratified fuel-air mixture grants it a diesel-like lean burn combustion behavior, which effectively brings its fuel efficiency up to about 35%, comparing to 28% fuel efficiency of the homogenous fuel-air mixture in PFI engines. Due to this increased fuel efficiency, GDI engines have seen a rapid adoption by the automotive industry over the past few years and are predicted to have an even deeper market penetration by the 2025 model year (**Figure 1**) [1].
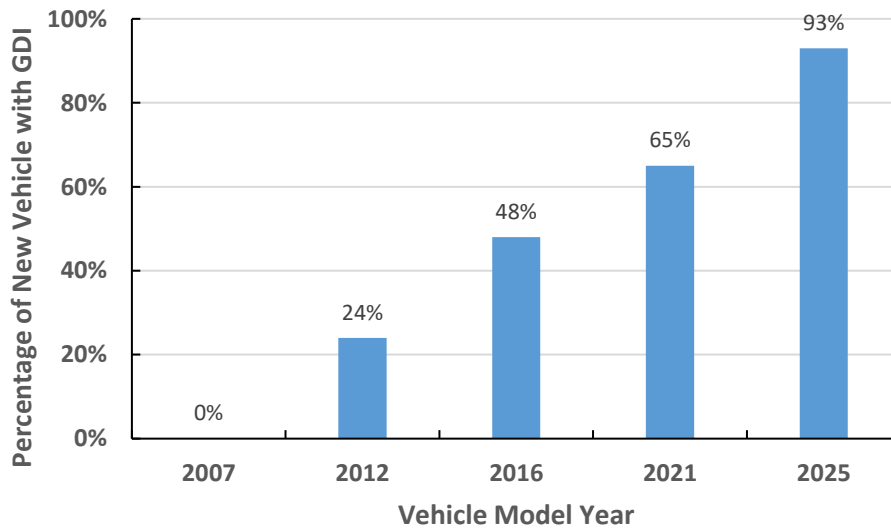
Figure 1. Predicted market penetration of vehicles with GDI engines based on data from[1].

Along with the diesel-like higher fuel efficiency, GDI engines also produce diesel-like particulate emissions. Particulate emissions from internal combustion engine are commonly measured in two ways, Particulate Matter (PM) and Particulate Number (PN). PM is mass based and is regulated in U.S., whereas PN is number based and is regulated in Europe. U.S. is also considering adopting the PN regulatory method. Both PM and PN emissions of GDI engines are higher than PFI engines, which has been shown in numerous experiments in the literature as shown in **Figure 2** [2-4]. Particulates on the scale of 100 nm, such as those from GDI, can penetrate deep and deposit in the fine airways of human respiratory system (**Figure 3**) [5]. Studies also show that long term exposure to fine particulates from exhaust can raise severe cardiovascular issues such as myocardial infarction, heart failure and stroke[6]. The rapid development and deployment of GDI engines have raised concerns regarding their PM and PN emissions and the corresponding adverse effects on environment and human health.
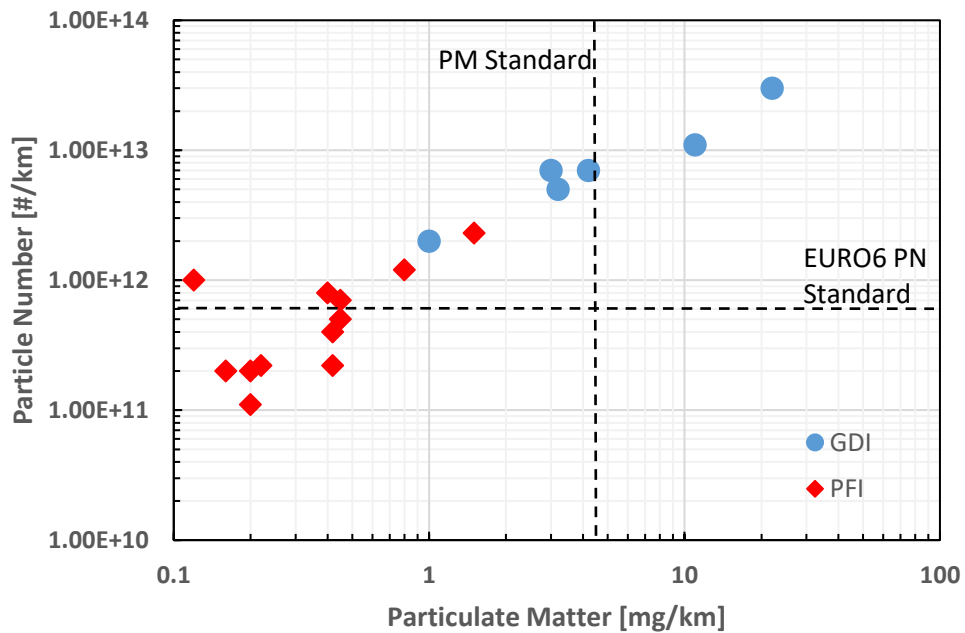
Figure 2. PM and PN emission of GDI engines are higher than PFI engines based on the data from[2].
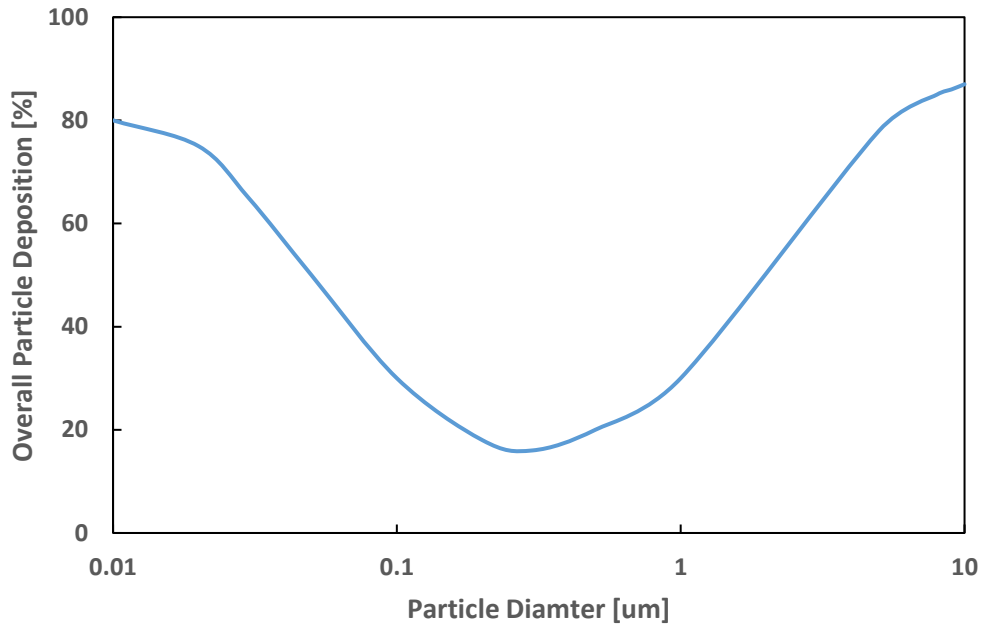
Figure 3. GDI-sized particles have high deposition rate in fine airway based on data from[5].

Countries around the world and their corresponding regulatory agencies have taken actions to propose strict regulations to control the PM/PN emissions, in response to the aforementioned health issues and the well-known environmental problems caused by GDI engines exhaust. Maintaining high air quality has been a priority of the United States Environmental Protection Agency (U.S. EPA), since the Clean Air Act of 1970. Recently, the California Air Resources Board LEVIII and U.S. EPA Tier 3 regulations have reduced the allowable PM emissions from previous level of 10 mg/mil to 3 mg/mil, which is in effect for vehicles in the 2017-2021 model years [7]. In Europe, the current EURO 6 regulation requires PN emission of gasoline engines to be less than $6\times10^{11}\,\#/km$. Emerging automotive markets, such as China and India, are just beginning to create their own regulations to control particulate emissions [4]. All of these new laws and regulations make the design of GDI engines and its exhaust aftertreatment system an extremely timely and

challenging problem, considering that most vehicles equipped with GDI engines in market exceed the EURO 6 PN regulations at cold start [8], as shown in **Figure 4**. Therefore, an advanced filter for GDI exhaust aftertreatment with high filtration efficiency, is necessary in order to meet the new regulations.
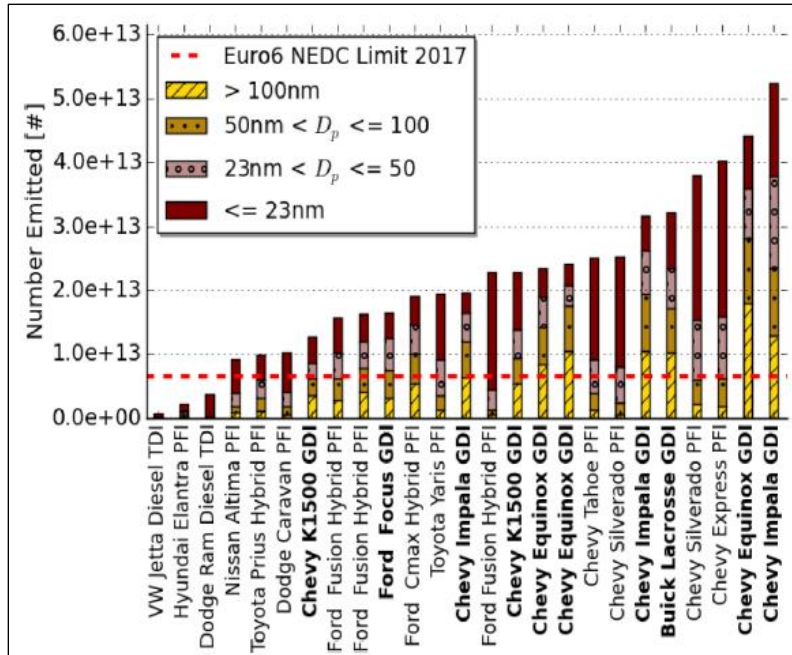
Figure 4. Vehicles PN emission at cold start. Most vehicles at test exceeded EURO 6 PN limit[8].

Ceramic wall-flow particulate filters have long been used to reduce particulate emissions from diesel exhaust. As one of the first wall-flow filters successfully commercialized, Diesel Particulate Filters (DPFs) are well-developed and have been widely applied on diesel vehicles for nearly two decades [3, 9, 10], with high filtration efficiency (>90%). DPFs are made primarily of cordierite or silicon carbide (SiC) ceramics, in a monolith with honeycomb structured porous walls. Cordierite and SiC ceramics are robust and durable enough to sustain the thermal and mechanical integrity of DPFs throughout lifetime. A typical DPF substrate consists of alternatively plugged

channels, half of which are inlet channels with the rest as outlet channels. Particulate-laden exhaust flow enters DPF inlet channels and is forced to pass through the porous wall into adjacent outlet channels, and particulates are mechanically filtered by the wall as this occurs. **Figure 5** Shows an inside look of the DPF channel flow and particulates deposition.

(a)   (b)
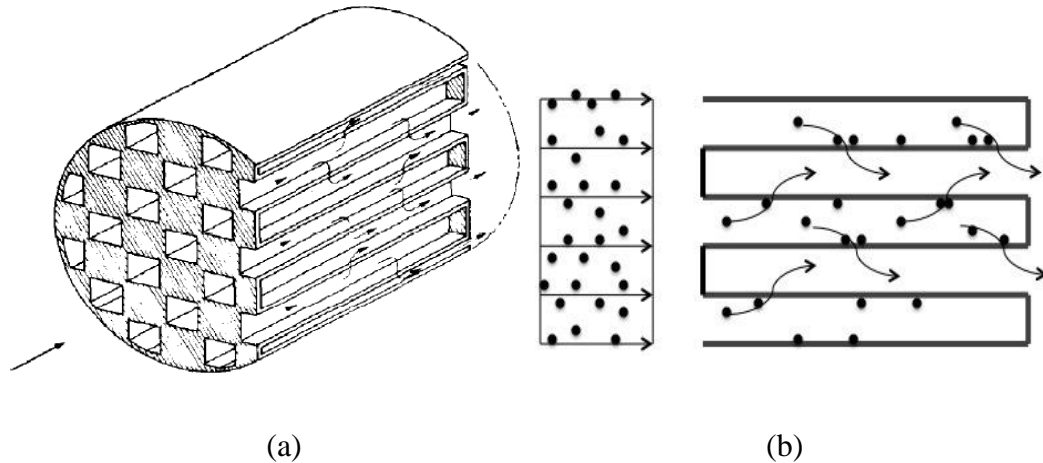
Figure 5. (a) DPF monolith, (b) DPF cross section view showing channel flow inside DPF with particle deposition in and on the porous wall[11].

The initial filtration efficiency of a DPF is quite low, at about 60%. This filtration performance does not meet the diesel PM/PN regulatory requirements. However, a soot cake quickly builds up on the walls in the DPF inlet channels, dramatically boosting the filtration efficiency to >95%. This is because the soot cake has a lower permeability and porosity than DPF wall substrate and plays a dominant role in DPF particle filtration. The soot cake formation along DPF channels is shown in **Figure 6** [12].
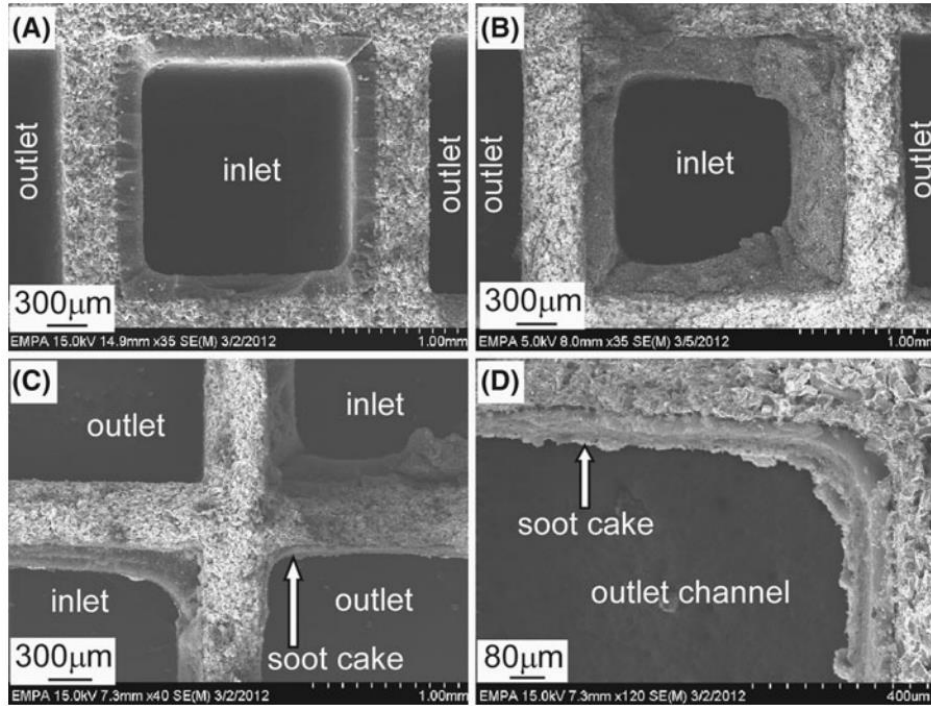
Figure 6. SEM images of typical DPF soot cake formation at different channel locations. (a) Middle part of DPF (b-c) Inlet part of DPF with thicker soot cake (d) Zoom in image of (c)[12].

Previous work in our group (Manuscript #1) suggests that despite the success of DPFs on diesel engines, they cannot be directly implemented on GDI engines for two reasons. First, the concentrations of PM emissions from diesel engines is much higher than GDI engines [2-4]. At the same time, diesel particulates are larger in size and help the rapid formation of the soot cake on the surface of DPF wall which achieves high filtration efficiency [13-15]. Whereas the absence of soot cake due to the smaller size and lower concentration of GDI particulates, makes DPFs insufficient for GDI engines aftertreatment [16]. Second, GDI engines are more sensitive to back pressure [17]. DPFs with high overall pressure drop can choke the GDI engines and lower the power output. Therefore, there is a need for specific GPFs with high filtration efficiency and low pressure drop to meet the ever-stringent PM and PN regulations.

The main objective of this study is to develop and exercise models to search for approaches to increase the GPF filtration efficiency, while keeping the pressure drop low. Analytical modeling of particulate filters has been extensively conducted due to its low cost, ease to adjust filter properties and high fidelity results [10, 13-15]. The foundation of the analytical filtration model is based on the "packed bed" theory, proposed by Payatakes in early 1970s. The theory assumes sequence of mono-sized grains (unit collectors) are connected in parallel to form a packed bed [18]. Lee employed the Kuwabara model of forces on a multiplicity of spheres in a viscous fluid, to simulate the filtration of aerosol particles through a packed bed [19, 20]. Later in 1980s, Bissett proposed a mathematical model of thermal regeneration of a wall flow monolith DPF [9]. Based on Bissett's work, Konstandopoulos and Johnson further developed an analytical model for DPF transient filtration and pressure drop predictions during soot loading [10]. These DPF-oriented filtration models showcase their robustness and credential for the DPF filtration prediction. However for GPFs, these classic filtration models need modification to fit the unique characteristics of GPF substrates and GDI particulates [11]. The classic filtration model assumes homogeneity of the filter wall substrate and derives the unit collector size assuming a constant wall porosity and characteristic pore size. However, for most commercial cordierite filters, the wall substrate pore size can vary in a wide range to establish a certain pore size distribution. To account for this heterogeneity of wall substrate, Gong developed a PDF-based heterogeneous multiscale filtration (HMF) model [21, 22]. The HMF model was proven to be a competent tool to study the microstructure effects of GPFs on GDI-sized particulates filtration behavior. Despite the advance HMF made over the classic filtration model, it is still an analytical model in core using the statistical method to resolve the probability density function of GPF wall pore sizes. More complex interactions between different sized pores, specifically how randomly dispersed small size pores

influence the flow in large pores, still need thorough investigation. Computational Fluid Dynamics (CFD) is a numerical method that can offer high fidelity flow field and particle tracking results in a complex geometry, making it an ideal tool to study the particle-laden flow in the GPF wall substrate, which is done in this study.

Three-way catalyst (TWC) washcoating on GPFs has been gradually adopted by vehicle manufacturers. The TWC washcoated GPFs can save valuable space in the packaging constrained aftertreament system, while potentially achieve the same filtration and catalyst conversion level as the close-coupled TWC and GPF separate devices. Additionally, washcoated GPFs are able to effectively reduce the catalytic precious metal loading, and in turn, reduce manufacturing costs. Given all the advantages of washcoated GPFs, research is still needed to look into how the washcoat impacts the filtration and pressure drop behavior. This study includes an investigation of washcoating strategies for GPFs so as to achieve a balance between high filtration efficiency and low pressure drop.

Ash accumulation is a known problem in DPFs, and its effects on GPFs have begun to be of concern with the wide application of GDI engines and the rigorous PM/PN regulations. Largely composed of non-combustible lubrication oil additives and engine debris, ash particulates are larger on average as compared to GDI exhaust particulates. During the lifetime of a GPF, ash can both penetrate into the substrate walls as well as deposit on top of the walls to form a cake. It is difficult to attain ash-loaded GPF samples due to the high cost of long-term testing on either engine dynamometers or in vehicles. The development of an accelerated aging system allows a rapid simulation of the ash loading procedure and enables more efficient research on ash accumulation [23]. Further modeling and experimental works are included in this study to investigate the accumulation and mobility of ash on filter channel [24]. Although ash accumulation with time has

been shown to be beneficial for filtration efficiency, there is an accompanying increase in the pressure drop across the filter that is an inevitable drawback [7, 25, 26]. Work from Ford demonstrated that there was a specific ash loading for which the filtration benefit outweighed the increase of the pressure drop [26], therefore, this work includes an investigation of the effect of controlled ash distribution (creating an artificial ash membrane or "ash cake") on GPF filter performance.

This dissertation starts off by modifying the classic analytical filtration model, so as to adapt it for the GPF substrate characteristics and GDI particulates properties. In addition to the existing filtration mechanisms of Brownian diffusion, inertia and direct interception, two additional particulate capture mechanisms, namely sedimentation and thermophoresis, were included in the new model.

Knowing that the microstructure of GPF porous wall plays a critical role in particulate filtration characteristics and overall pressure drop [27], a 2D CFD study of the substrate pore size, connectivity and distribution was conducted. The "throat unit collector" model is introduced to better capture the microstructure features of GPFs. Compared to the conventional analytical model, such as HMF, this CFD study provides detailed flow field information and particle motion trajectories within the substrate. This information is crucial in terms of understanding the dynamic interactions between particulates and the wall microstructure, and is able to give direction for a better performing GPF design.

To enable a particle tracking CFD study, a 3D GPF model was also created. This 3D model, along with a custom User Defined Function (UDF) allows thorough investigations of the washcoat/ash-driven permeability non-uniformity of GPF wall and its effects on the GPF performance. The implementation of the UDF enables fast initial definition of GPF wall properties

9

and transient updates. The UDF is also able to solve the particle filtration efficiency effectively. Both steady state and transient simulations were conducted to study the target GPF samples filtration, pressure drop and soot deposition profiles with time.

CHAPTER II

MANUSCRIPT #1

Overview

Gasoline Direct Injection (GDI) is known to produce lower concentrations of smaller particulate matter (PM) as compared to diesel combustion [2]. This results in the absence of soot-cake formation on the filter channel wall and yields changes in filtration behavior as compared to diesel particulate filters (DPF). Therefore, studies of cakeless filtration regimes for smaller sized particulates is of particular interest for GDI PM mitigation. This work investigates the filtration efficiency of laboratory-generated particulates, representative of GDI-sized PM, in uncoated, commercial DPF cordierite substrates of varying porosities. Size-dependent particulate concentrations were measured using a Scanning Mobility Particle Sizer (SMPS), both upstream and downstream of the filters. By comparing these measured concentrations, the particle size-dependent filtration efficiency of filter samples was calculated. A model suitable for predicting filtration efficiency for these non-loaded particulate traps was further developed from a flow field model [28], with soot-cake related filtration approximations removed. The improved model includes additional sedimentation and thermophoretic modes of filtration. Experimental results showed excellent agreement with model predictions. Our study demonstrated that current DPFs cannot be used as a gasoline particulate filter (GPF) due to its low filtration efficiency for GDI sized particles. Further developments of the GPF are essential and the newly developed filtration model can serve well to facilitate the filter design.

Introduction

Internal combustion engines are used ubiquitously in the developed world, and produce harmful emissions as a byproduct of combustion. In particular, the emissions of PM are detrimental to health; those produced by diesel engines have been shown by the World Health Organization (WHO) to cause cancer [29]. Long realizing the detrimental influence of PM, filtration of diesel particulates has been mandated by the United States Environmental Protection Agency (EPA) since 2003. Increasing focus on fuel economy and CO_2 emissions encourages the deployment of GDI engines. GDI engines have improved fuel efficiency compared to traditional homogeneous charge, spark ignition gasoline engines, but also have increased particulate matter emissions. GDI particulate has both lower particle number (PN) concentrations and smaller particulate sizes than that of conventional compression ignition diesel, with its particle size distribution peak at about 50nm [30, 31], compared to the peak at 100nm for diesel [32-34]. **Figure 7** illustrates the differences in the mass (also an indicator of particle size) and number of particle emissions for a variety of exhaust types. It is notable that GDI is the next largest in size and PN to diesel, making it the next logical target of regulations. Currently, no GDI particulate filtration requirement exists in the U.S., but GDI particulates are subject to the preliminary EURO 6 PN standard (<6e+12 #/km). However with the introduction of the more stringent official EURO 6 in 2017(<6e+11 #/km), a breakthrough of the filter technology in terms of GDI sized particulate filtration efficiency and pressure drop is needed in order to meet the new regulation levels.
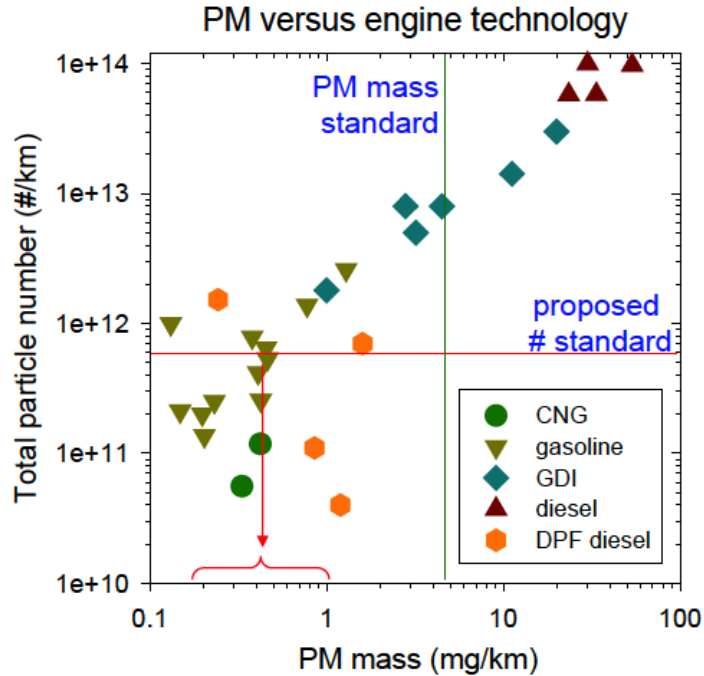
Figure 7. Qualitative differences between particulate emissions of several engine technologies[2].

For comparison, in DPFs, particle-laden flow enters the open channels of the substrate, travels axially through the channel, and is forced to pass through a filter wall by the impermeable plugs to exit the filter, as illustrated in **Figure 8**. The porous material mechanically removes particulate matter, and the captured particulate quickly blocks the pore throats and forms a cake layer on the inlet wall surfaces of the filter. Once established, the cake is responsible for the majority of the filtration, and the filter quickly reaches >95% filtration efficiency. Since GDI particulate are both fewer and smaller than diesel particulate, a soot cake is unlikely to form. Thus, the filtration of GDI particulate will be the function of the cakeless substrate alone.

13
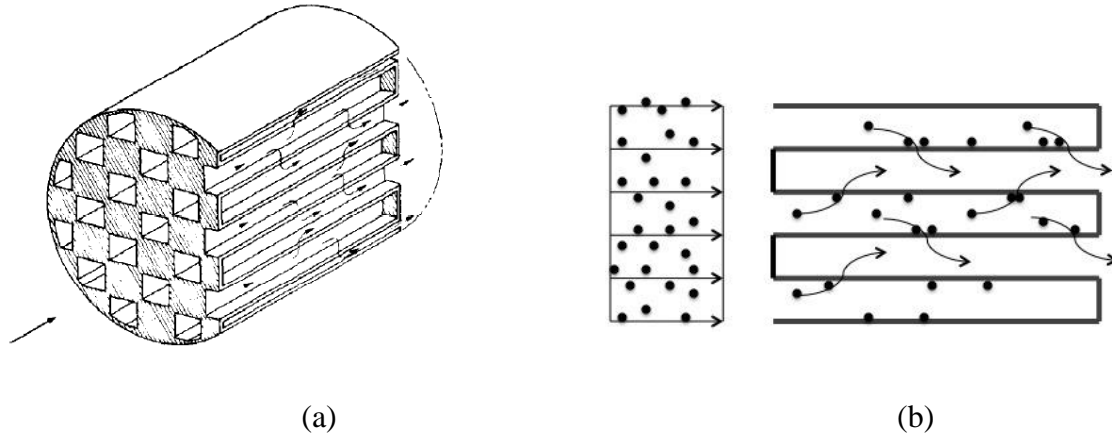
Figure 8. (a) DPF geometry, (b) Illustration of flow through a DPF channel wall.

Research to date has primarily focused on filtration of diesel-sized particulate and has relied upon the filtration done by the soot cake. Only a few experimental studies have been made of filtration of smaller particles like those in the GDI size-range. Researchers such as Saito, Chan, Ito, and Parks [35-38] conducted experiments on engine benches to understand the filter geometry and layout effects on GDI particulate filtration efficiency and pressure drop in Gasoline Particulate Filters (GPF). Richter [39] also investigated the influence of a catalyzed coating of GPF on its performance.

In terms of the filtration modeling, Payatakes proposed a model for the porous media filtration back in 1973, by modeling the pores into numerous mono-sized grains (unit collectors) connecting in parallel to form a packed bed [18]. Payatakes not only studied the effects of properties of a single unit collector on filtration, he also considered the influence of neighboring unit collectors. Later in 1979, inheriting the packed bed filtration concept of Payatakes, Lee's work set a rigid foundation for research in particle-laden gas filtration [19]. Lee employed the Kuwabara [20] model of forces on a multiplicity of spheres in a viscous fluid to model the filtration of aerosol particles from gas by a packed bed. The earliest work on DPF modeling was done by Bissett, who

developed a mathematical model of the thermal regeneration of a wall flow monolith DPF [40]. His analytical solutions to the time dependent temperature, deposition thickness and pressure drop during regeneration are still referred to by researchers to date. Konstandopoulos and Johnson conducted a theoretical study of the performance of a DPF, in terms of pressure drop and particulate collection characteristics [10]. The model they developed assumed the DPF to be an isothermal, perfectly packed bed of spheres at steady-state, and included both Brownian diffusion and direct interception modes of filtration. Further work by Opris and Johnson [28] developed a two dimensional filtration model, that describes the transient nature of the filtration, due to loading. The Opris model built upon the Konstandopoulous model by adding a term for filtration due to inertial impaction. Even though the simulation studies on diesel particulates filtration is quite mature, no model has yet been developed to simulate a GDI sized particulate filtration characteristics in a cake free regime. The major objective of this work is to update and refine an existing DPF filtration model and make it useful for predicting the behavior of filters with no soot cake.

In this paper, a modified filtration model is developed based on Opris model. The soot cake approximations have been removed from Opris model and two additional influence factors, gravity and thermophoresis, were added. The Opris model, which includes Brownian diffusion, direct interception, and inertial impaction modes of filtration, makes an excellent foundation because GDI filtration models will need to shift from reliance on soot cake filtration to deep bed filtration. Additionally, this work experimentally investigates the size-dependent filtration efficiency of simulated GDI-like particulate through commercial cordierite DPF. DPF samples with different porosity and cell density were investigated at two distinguished space velocities in experiments to evaluate the impacts of filter properties and space velocity on the particle filtration efficiency.

Long duration tests were also run to study the temporal characteristics of the particle filtration efficiency. The experimental results were collected and compared to that of the simulation in terms of the size-dependent filtration efficiency, in order to verify the accuracy of the GDI filtration model.

Model Development

To generate a model that simulates the filtration efficiency of non-loaded (cakeless) particulate traps for GDI range PM, we began with the full 2D flow field model by Opris and Johnson as the base model. This model is based on the packed bed filtration hypothesis and was modified to more accurately describe the filtration behavior of filter without a soot cake. These modifications include the removal of cake-filtration related approximations, and the addition of sedimentation [41] and thermophoretic [42] modes of filtration to the pre-existing modes of Brownian diffusion, inertial impaction, and direct interception. The experimental data were then compared to model filtration efficiency predictions.

The overall filtration efficiency, η, is calculated as shown in equations (1) and (2) below, where E_D, E_R, E_I, E_G, and E_T are the specific efficiencies due to Brownian diffusion, direct interception, inertial impaction, sedimentation, and thermophoresis respectively. Each specific efficiency is based on the packed bed model and formulated as a function of sphere and particle properties and gas flow condition. C is the empirical fit factor. In these equations, ε is the filter porosity, w is the channel wall thickness, d_p is the diameter of the particle, d_c is the diameter of the unit collector, and β is the fraction of the filter which is substrate rather than empty space. Usually the d_c can be estimated by $d_c = \dfrac{3}{2}\dfrac{1-\varepsilon}{\varepsilon}p_d$, where p_d is the pore dimeter.

16

$$\eta = 1 - e^{-\alpha} \qquad (1)$$

$$\alpha = \left(\frac{4\beta w}{\pi \varepsilon d_p}\right)\left(C \cdot E_D + E_R + E_I\right) + \frac{-3\beta}{4\left(\frac{d_c}{2}\right)} E_G + E_T \qquad (2)$$

The expressions for E_D, E_R, E_I are elaborated in the Opris and Johnson's paper [28], therefore will not be further discussed here. To consider all possible mechanism, sedimentation as a potential filtration mechanism for GDI particulates is added, though it plays a much lighter role than the aforementioned three. Similarly, future study will use GDI engine dyno as the particle source. Due to the high exhaust temperature and heat transfer phenomenon occurring in the filter, thermophoretic mechanisms need to be considered.

Filtration by sedimentation, described in equation (3), is caused by gravitational effect on particles. Larger, more massive, particles may lose entrainment and be collected by the filter [41].

$$E_G = \frac{\rho_p - \rho_g}{\left(18 \cdot \mu \cdot u\right) \cdot 9.81 \cdot d_p^{\,2}} \qquad (3)$$

Filtration due to thermophoresis occurs at the channel level, rather than in the porous walls of the filter bed. Particles will move due to a temperature gradient. This effect increases with the thermal conductivity of the particle, with the steepness of the gradient, and decreases with flowrate. For equations 4-14, the Reynolds and Nusselt numbers are calculated for the square filter channel. The convective heat transfer coefficient is given by h, the drag coefficient by f, and particle diffusivity by D. K_{th} is a thermophoretic coefficient that describes how strongly a particle will be affected by a thermal gradient. Cu is the Cunningham correction factor. C_c is a correction factor first used by Wang to match experimental data to prediction, with w_c being the width of the square channel, and y_{van} as the van der Waals scale [42].

$$E_T = \frac{C_c \cdot \rho_g \cdot c_p \cdot \text{Re}_{De} \cdot f \cdot K_{th} \cdot v \cdot (T_i - T_w)}{De \cdot h \cdot \bar{T} \left(1 - e^{\left(\frac{-C_a \cdot P \cdot h \cdot L}{\rho_g \cdot Q \cdot c_p}\right)}\right)} \tag{4}$$

$$Q = \frac{-\kappa A}{\mu} \frac{\Delta p}{L} \tag{5}$$

$$\bar{T} = \frac{T_i + T_w}{2} \tag{6}$$

$$h = \frac{k_g \cdot Nu_{De}}{De} \tag{7}$$

$$Nu_{De} = \frac{f \cdot (\text{Re}_{De} - 1000) \cdot \text{Pr}}{8 \cdot \left(1 + 12.7 \sqrt{\frac{f}{8}} \left(\text{Pr}^{\frac{2}{3}} - 1\right)\right)} \tag{8}$$

$$\text{Pr} = \frac{c_p \cdot \mu}{k_g} \tag{9}$$

$$K_{th} = \frac{2.294 \left(\frac{k_g}{k_p} + 2.2 \cdot Kn\right) \cdot Cu}{(1 + 3.438 \cdot Kn)\left(1 + \frac{2k_g}{k_p} + 4.4 \cdot Kn\right)} \tag{10}$$

$$Cu = 1 + \left(\frac{2 \cdot \lambda}{d_p}\right) \cdot \left(1.257 + 0.4 e^{\left(\frac{-0.55 \cdot d_p}{\lambda}\right)}\right) \tag{11}$$

$$f = 0.3164 \cdot (\text{Re}_{De})^{-.25} \tag{12}$$

$$D = \frac{B \cdot T_i}{3 \cdot \pi \cdot \mu \cdot d_p} \tag{13}$$

$$C_c = 0.82 \cdot \left(\frac{w_c}{2 y_{van}}\right)^{1/7} \tag{14}$$

The pressure drop across the DPF substrate wall is governed by Darcy's Law, which can be written as

$$-\nabla P = \frac{\mu}{k} u, \tag{15}$$

Here, u is Darcy's flux and k represents the intrinsic permeability of the porous media.

The implementation of Darcy's law to calculate the pressure drop is further quantitatively defended for typical honeycomb monolith filters by Knostandopoulos and Johnson [10]. Rewriting the Darcy equation to include the properties of our DPF samples, yields,

$$\Delta P = P_i - P_o = \frac{\mu}{k_e} uw, \tag{16}$$

where k_e is the effective permeability of the wall, while u and w are the wall velocity and wall thickness. Although k is an intrinsic property of the wall, we still define effective wall permeability k_e due to the fact that the porosity of wall decreases as deep bed filtration proceeds, and this in turn lowers the effective permeability of the wall, which makes k_e an extrinsic property.

Experimentation

Experiments were done to validate the model and further investigate the time dependent filtration performance of the filters. The experimental setup is represented schematically in **Figure 9**. Filtered building air (1) enters the atomizer (2), then the particle-laden vapor enters gas driers (3) to remove moisture. The dry particulate stream is mixed (4) with make-up air to achieve the experimental flow rates. The particulate concentration can be measured at the inlet or exit of the sample holder (5), and the differential pressure transducer measures the pressure drop across the filter as a function of loading. Particulate concentration is measured by the SMPS, which consists of an electrostatic classifier (6 & 7) and condensation particle counter (8).
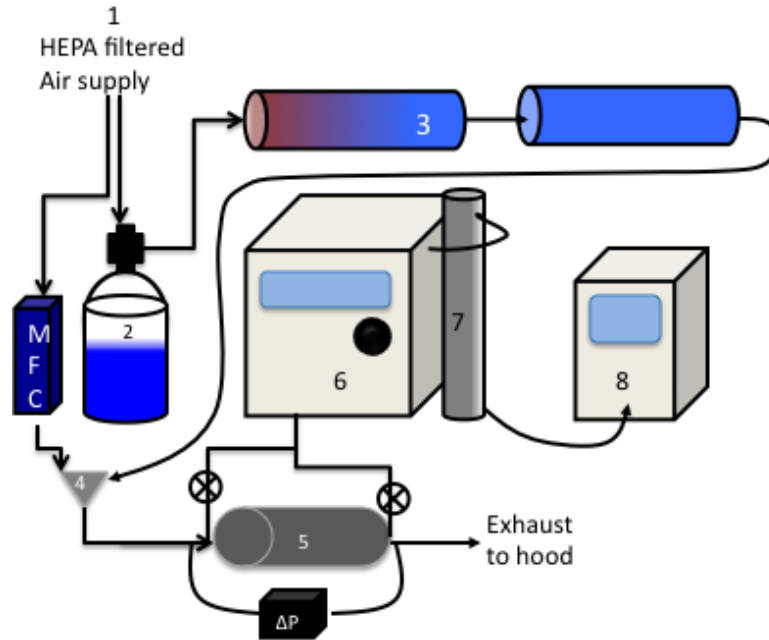
Figure 9. Experimental setup of the filtration and pressure drop characteristic study of filter samples. For each number-labeled devises, (1)Building air supply,(2)Atomizer,(3)Drier,(5)Sample holder,(6-8)SMPS.

Study of Salt Concentration Effect on Particle Size Distribution

Laboratory-generated salt particles rather than soot were used in this study for reproducibility and ease in 'regeneration' of the filters [43]. Particulates were generated by atomizing a salt solution in a TSI Model 3076 atomizer, shown in **Figure 9** , labeled #2. The peak of the particle size distribution lies at ~70 nm, comparable to the typical particle size of GDI soot. The correlation of the peak particle size with salt concentration was studied, in order to determine the solution concentration that generates particle distribution with the desired peak size. Two types of salt, Ammonium Sulfate and Sodium Chloride, were examined and for each salt, several concentrations (0.01 Molarity~0.1 Molarity) were made to study the particle size distribution shift along with the concentration change. The particle size distributions were measured by SMPS.

Study of System Losses

To measure the system loss of particles with the sample absent, we tested the particle size distribution upstream and downstream of the empty sample holder, using SMPS. Seven replicates for each case were performed under the same conditions later used for filtration tests, employing 0.025 M Ammonium Sulfate to produce the aerosol, at both 15,000 hr^{-1} and 30,000 hr^{-1}.

Study of Filtration Efficiency of Samples

Particle size-dependent filtration efficiency of samples was measured by a SMPS, following a protocol similar to that developed by Pacific Northwest National Laboratory (PNNL) [44]. The SMPS was configured up to the sample from either upstream or downstream of the filter sample. By comparing the particle counts as a function of particle diameter for these two locations, the size-dependent filtration efficiency was calculated.

The Mass Flow Controller (MFC) was used to dilute the particle-laden flow out of the atomizer. 15,000 hr^{-1} and 30,000 hr^{-1} space velocities were selected in this study, to simulate the GDI exhaust flow rate in the real situations. Further dilution of the flow will cause a drop of particle concentration down below 100,000 #/cm^3, which makes it hard for SMPS to resolve. We will extend the work to higher flow rates with the addition of a second atomizer in future study.

Three uncoated cordierite wall-flow filters with different porosities were used in this study; 55.8%, 61.1% and 65.0%, with mean pore diameter of 18, 20 and 23 um respectively. The cell density of the samples also varies as 200 CPSI, 300 CPSI, and 200 CPSI with the same wall thickness as 0.3mm (12 mil), displayed in **Figure 10**. For statistical analysis, we tested three different filter samples of each porosity.
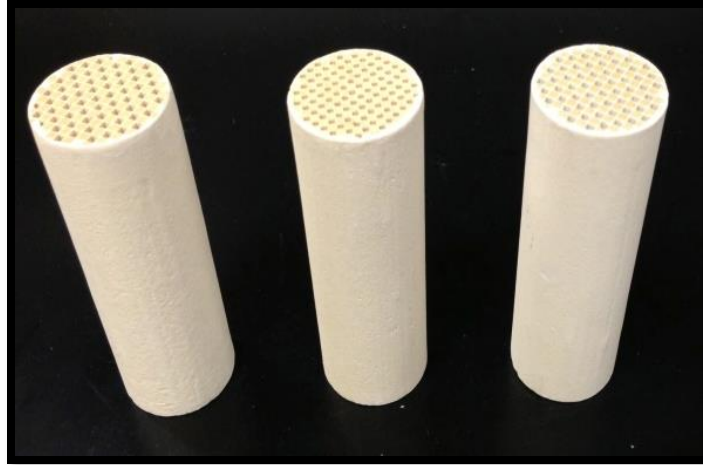
Figure 10. Cordierite DPF samples. From left to right, the samples have porosities of 55.8%, 61.1% and 65.0%.

During the experiment, each filter sample was tested in a fresh, never before used state, and in a standard re-used operating state. The post-regeneration (washing) standard state experiments were run multiple times for statistical analysis. For all cases, the samples were evaluated at hour 0, hour 1, hour 2 and hour 3. A set of extended tests on one filter sample of each porosity was run in order to determine when or if cake formation begins to occur. All tests were repeated at two flow rates representing 15,000 hr^{-1} and 30,000 hr^{-1} space velocities. For regeneration, after each round of testing, the filters were sonicated with heating in a water bath, using distilled, deionized water to remove the accumulated salt.

Results and Discussion

Salt Solution Selection

The particle size distribution was measured by SMPS for each solution and results were put together to highlight the trend, as displayed in **Figure 11** (a). The peak shifts to lower particle diameter as concentration decreases. To illustrate this trend, the distribution peak locations versus

solution concentrations were plotted and fitted with an exponential function in **Figure 11** (b). From the correlation function, the solution concentration can be obtained for any peak particle diameter desired. Thus, 0.025 M Ammonium Sulfate solution was selected to generate the simulated GDI sized particle. The choice of Ammonium Sulfate over Sodium Chloride allows for more spherical particles.
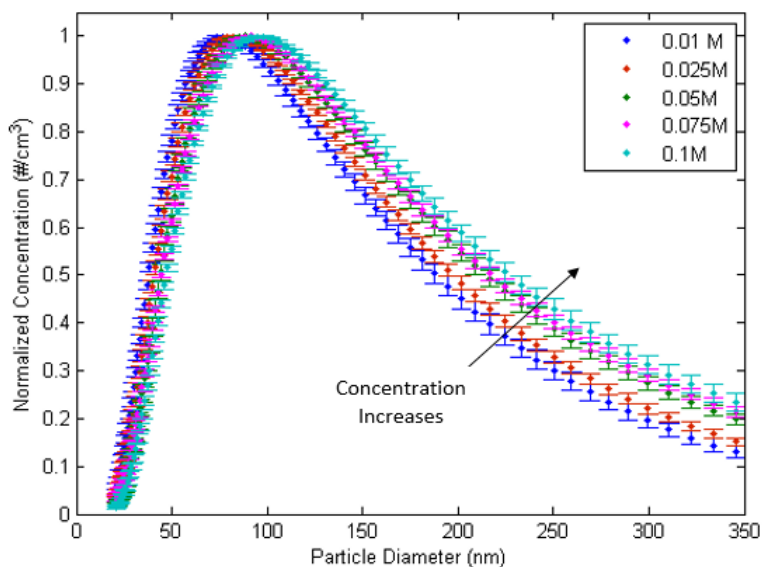
(a) Concentration Effect on Ammonium Sulfate Particle Size Distribution
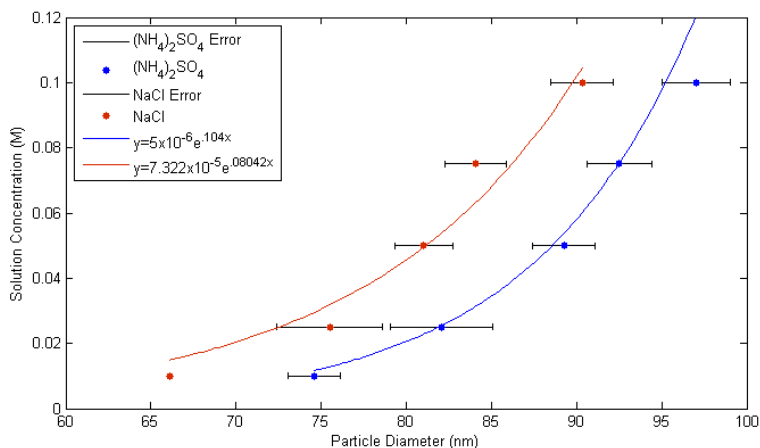
(b) Distribution Peak Location versus Concentration

Figure 11. Effect of solution concentration on particle size distribution.

The normalized particle count differences with error bar for each case, were plotted in **Figure 12**. Overall, the system losses at the higher flow rate were greater than lower flow rate, with the exception of particles diameter above 250nm. This may be due to the greater effect of gravitational sedimentation at the lower flow rate on particles that are larger and heavier. Since the system losses are less than 10% in the 50nm to 150nm particle diameter range of interest, we may safely neglect them.
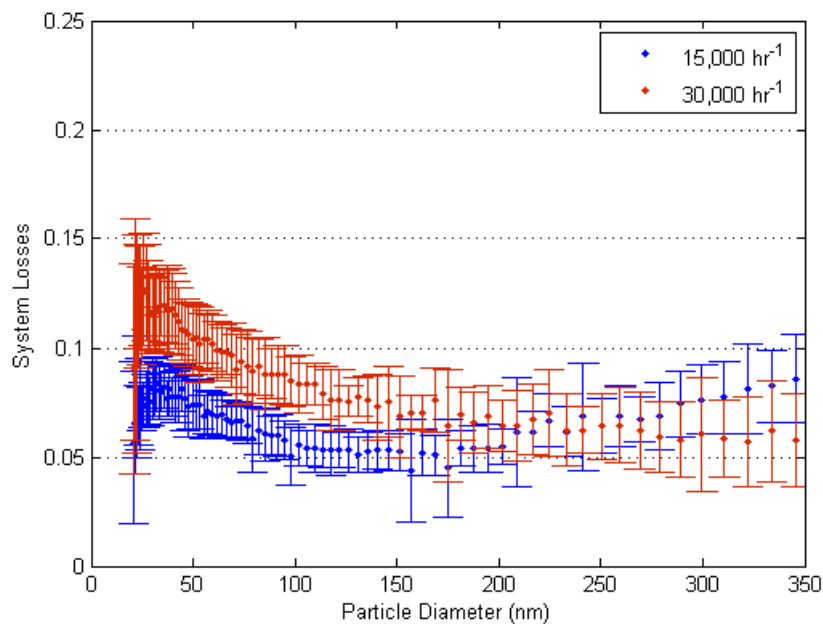
Figure 12. System losses of the empty sample holder.

Filtration Efficiency of Samples

The time dependent filtration efficiency of the 55.8% porosity, 200 CPSI sample was plotted in **Figure 13** (a). For each hour evaluated, filtration efficiency decreases as particle size increases. The reason for it is that Brownian diffusion, as a capture mode, dominates for smaller

size particles and faints as particles become bigger, while the largest particle diameter of interest (150 nm) in this study is not large enough to allow the inertial impaction capture mode come into effect. The filtration efficiency increases most in the first four hours of observation, and continues increasing more slowly after the fourth hour. The consistent, monotonic increase in filtration efficiency is what we would expect as the filter walls accumulate particulate. Evidence of the beginning of cake formation can be seen between hours four and six, and the filter approaches a fully loaded state in eleven hours. Compared to that of the diesel particles cake formation, normally between 30 to 45 min, the GDI sized particles simply takes much longer of time. The discrepancy can be explained that the diesel particles, with peak size at ~150 nm, fall into the accumulation mode of filtration, featured direct interception and inertial impaction as predominant ways of filtration. This allows the diesel particles to be captured by the wall surface the instance filtration process starts, and quickly build up a particulate layer (cake) on the wall surface. On the contrary, GDI sized particles, like what we generated in this study, exhibit nuclei mode of filtration featuring Brownian diffusion. Small particles tend to go with the flow stream and trap within the wall, which makes it hard to form a cake on wall surface.

The hourly filtration efficiency of the 61.1% porosity, 300 CPSI sample, given in **Figure 13** (b), indicates the beginning of cake formation between hour five and hour eight, and approached fully loaded at hour eleven. The results of the 65.0%, 200 CPSI sample are presented in **Figure 13** (c). The filtration efficiency increased with each hour, but the filter did not reach cake filtration by hour eleven. Comparing these three filter samples with different porosity, we can find out that larger porosity usually takes longer time to form a soot cake. This is because filters with larger porosity indicate more void space within the wall and in turn take longer time to fill up those void by particle deposition.

Figure 13 (d) illustrates the sample pressure drop against time. Different markers indicate filter samples with different porosities. An increase of pressure drop of the 55.8% porosity sample can be observed, attributed to the earlier formation of the soot cake. Once a mature cake is formed, the filtration mode switches from deep bed filtration to cake filtration. A pressure drop increase occurs due to the much lower porosity of the cake. Compared to the 55.8% porosity sample, the other two samples barely experienced a pressure drop increase at hour nine, indicating the initial state of cake formation. This time mark matches what we observed in the time dependent filtration efficiency plot. Though particles were continuously trapped in the wall. A mature cake never formed for the 65% samples. What we observe here is contradictory with the typical pressure drop behavior of the diesel particles. As discussed in Opris and Johnson's paper [28], the diesel particle pressure drop can be divided into three stages: transient condition for porous wall, transient condition for particulate layer and steady state condition for particulate layer. While loading, DPF will undergo a rapid increase of pressure drop at the first stage due to the decrease of wall porosity, which doesn't match the result of this study. There are two reasons that might explain the discrepancy. First, GDI particle is about one order of magnitude lower than diesel particles, in both number concentration and mass concentration. Second, the flow rate in our study is lower than the typical diesel engine flow rate. Both reasons combined can lead the filter samples trap much less particles.
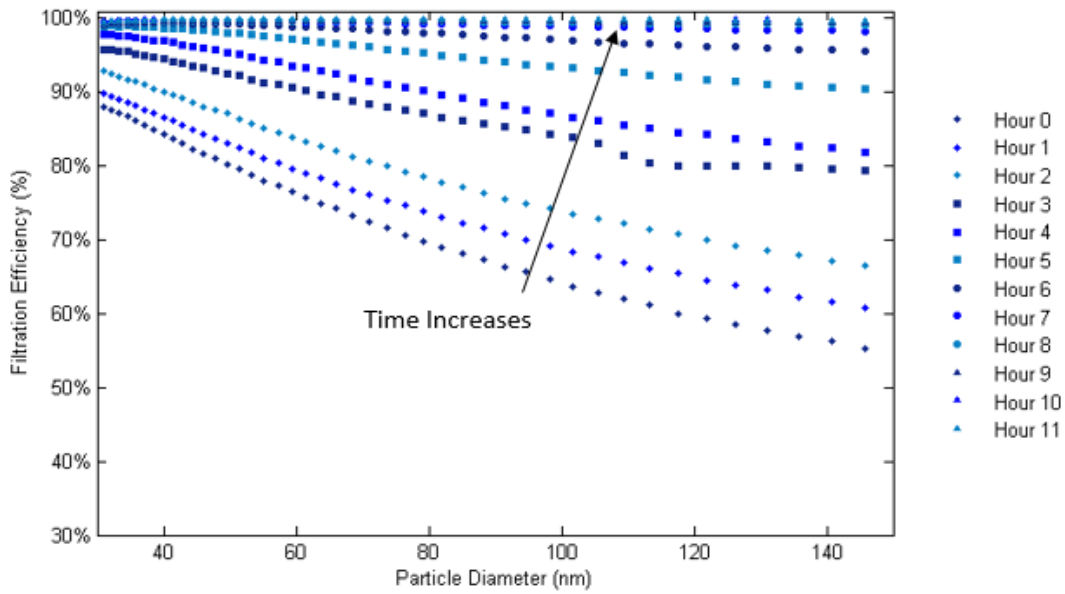
(a) 55.8% porosity, 200 CPSI filter
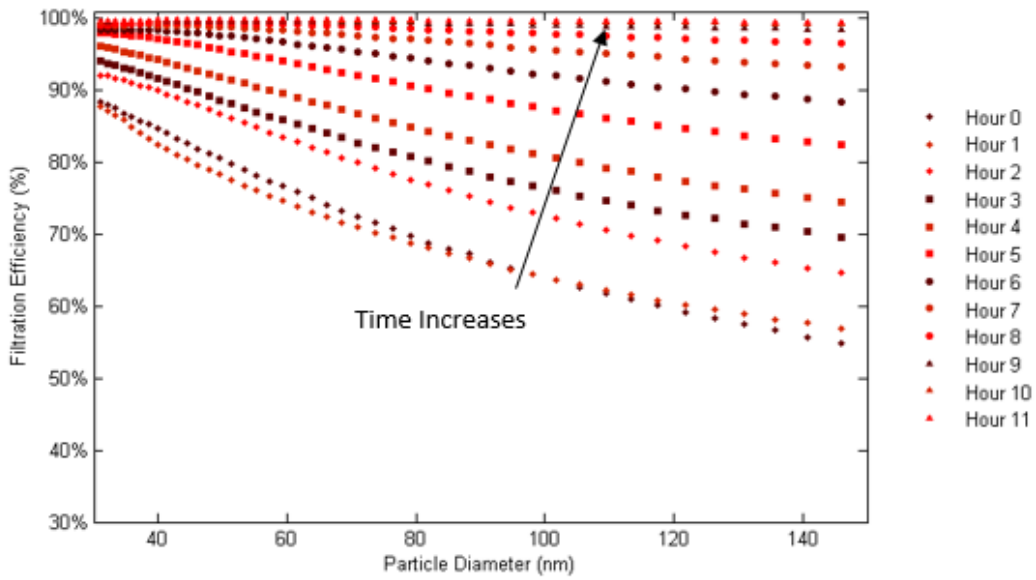
(b) 61.1% porosity, 300 CPSI filter

Figure 13. Filtration efficiency (a-c) and pressure drop (d) as a function of time at 15,000 hr^{-1}.
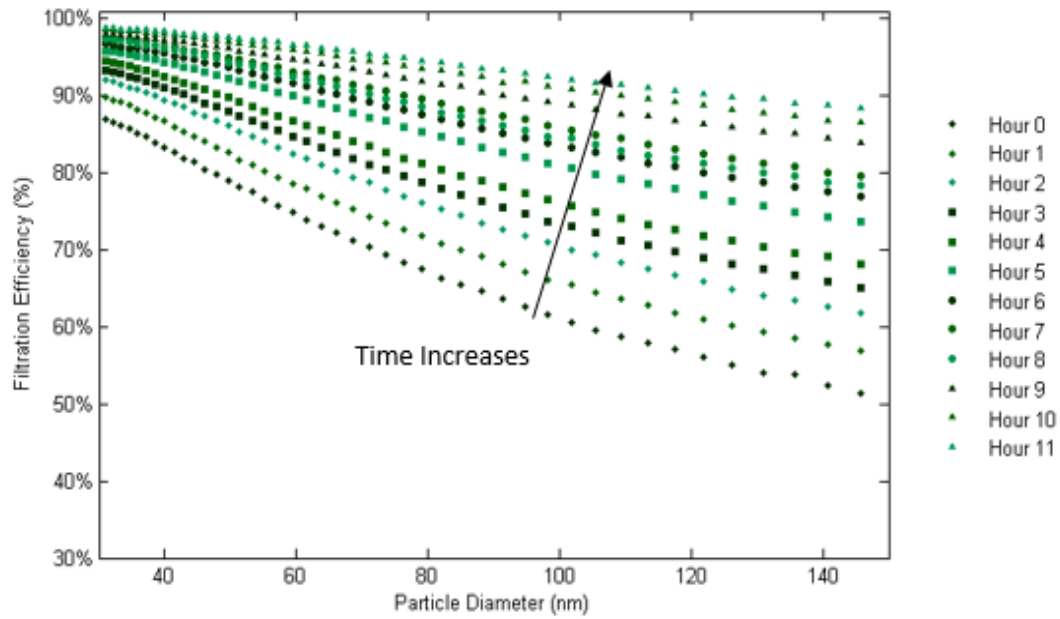
(c) 65.0% porosity, 200 CPSI filter.
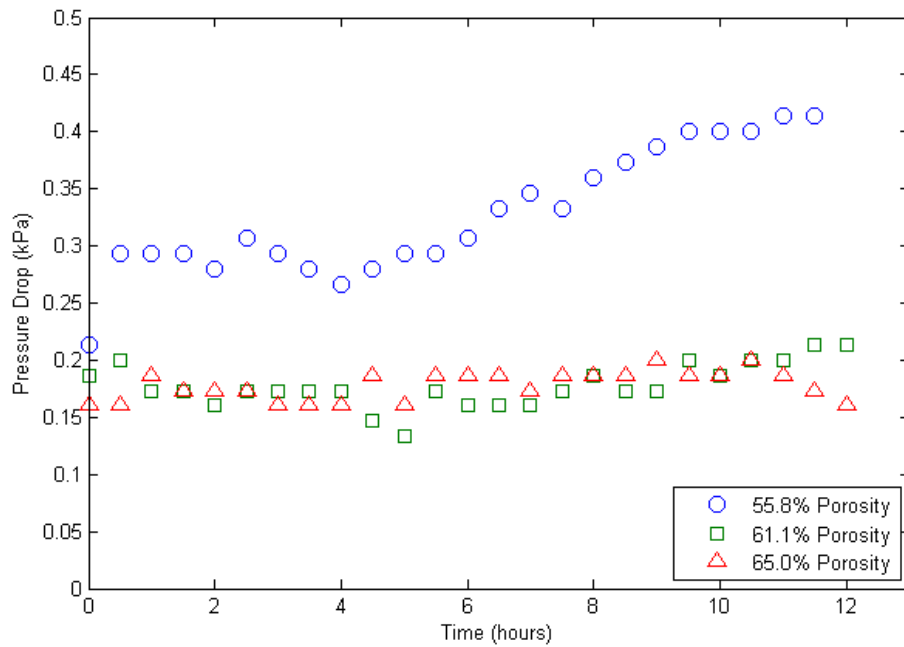
(d) Pressure drop

Figure 13. Continued.

28

Figure 14 and **Figure 15** show the effects of filter porosity and flow rate on the filtration efficiency. The filtration efficiency of the 65% porosity is lower than that of the 55.8% porosity. The most trivial explanation for this is that, at the same cell density, the smaller porosity is, the smaller mean pore diameter is, which indicates pores are easier to be blocked by particle matter and allow fewer particle matter to pass. The 61.1% porosity does not fall between the two, likely due to its higher number of cells per square inch. The higher cell density leads to a low surface velocity at the filter wall, which increases filtration efficiency significantly. Also, for the same filter, lower flow rate leads to higher filtration efficiency, as indicated in **Figure 15**, similarly because lower flow rate means lower surface velocity, which induces higher filtration efficiency.
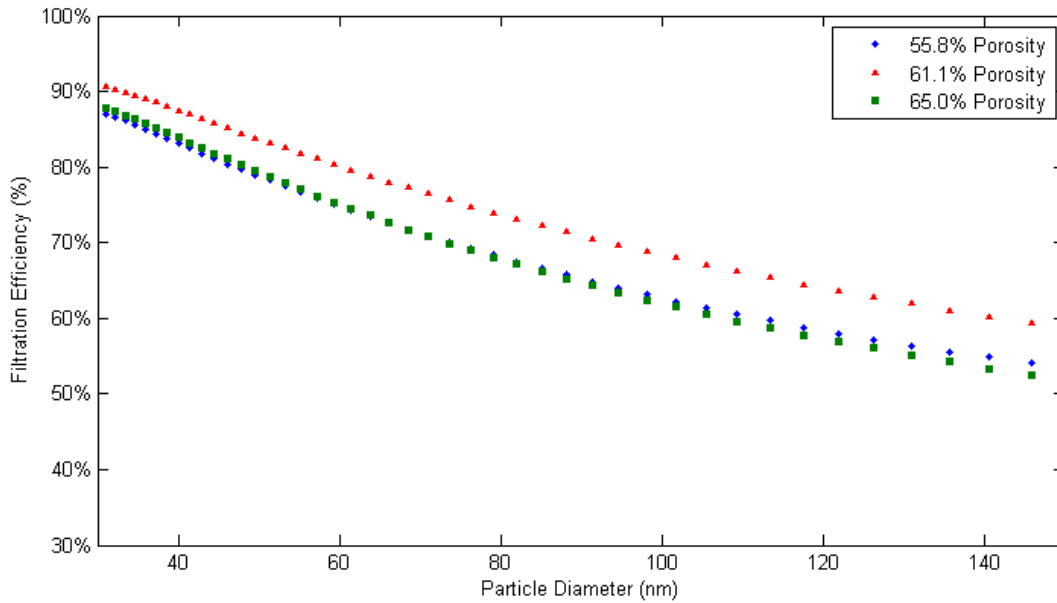
(a) 15,000 hr-1

Figure 14. Effect of Porosity on Filtration Efficiency at (a) 15,000 hr^{-1} and (b) 30,000 hr^{-1}.
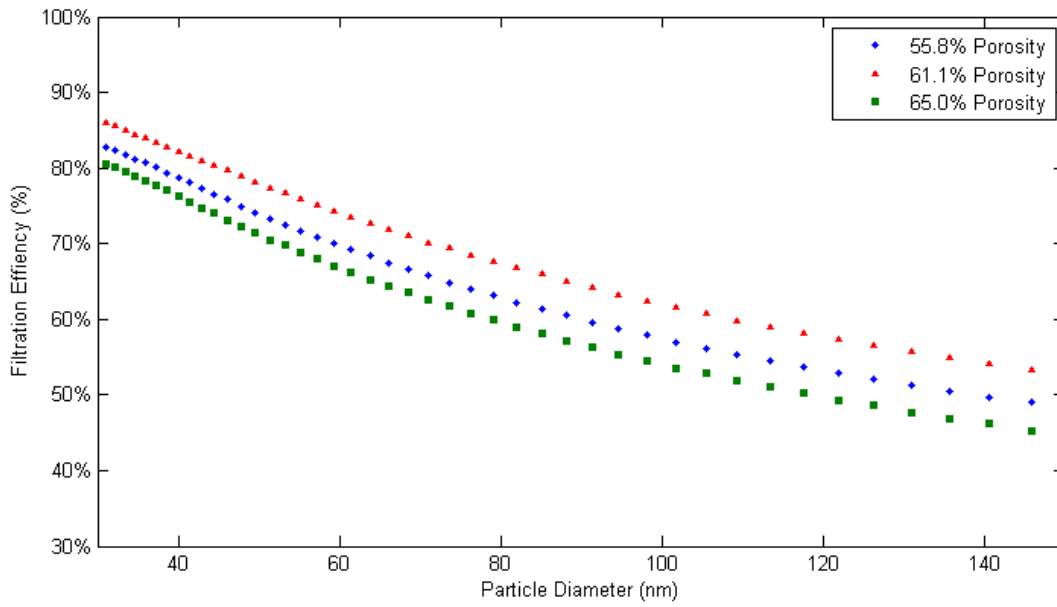
(b) 30,000 hr^{-1}

Figure 14. Continued.
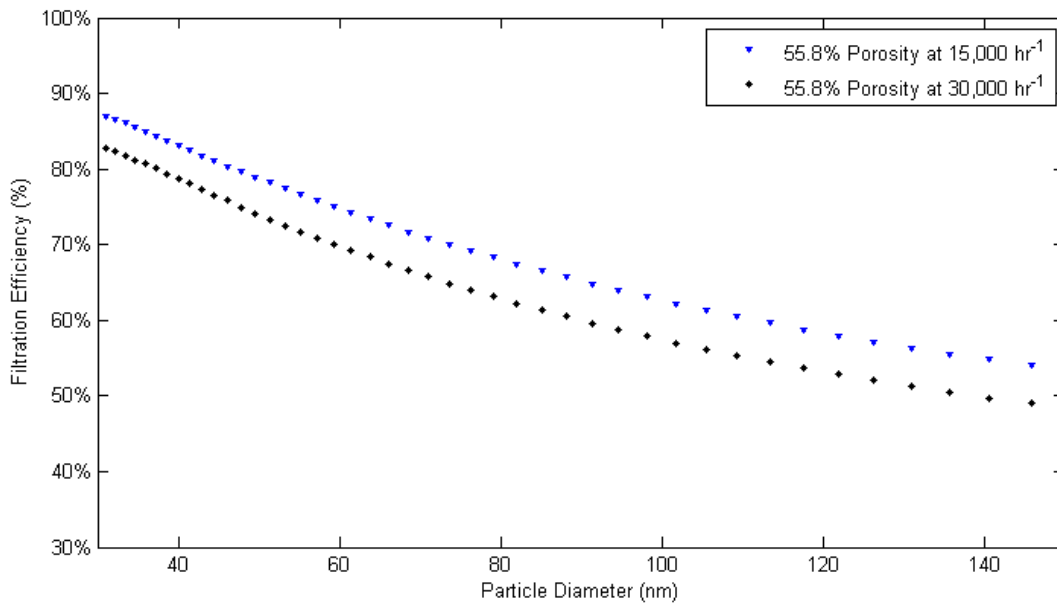
Figure 15. Comparison of 15,000 hr^{-1} and 30,000 hr^{-1} filtration efficiencies for a single filter porosity.

According to Darcy's Law, changes in the pressure drop across the filter wall result from changes in the effective permeability of the wall while loading. The effective permeability presented in the following figures were back-calculated using Darcy's equation. The results, given in **Figure 16**, show the flowrate and loading effects on filter wall permeability. As expected, at the same porosity, increased loading decreases the effective permeability of the filters. This phenomena can be interpreted as following: the effective permeability of cordierite is proportional to the porosity to the power of 5.5, govern by the correlation $k_e = \dfrac{\varepsilon^{5.5}}{5.6} d_f{}^2$ [45]. When particulates gradually accumulate by the filtration effect, the porosity of the wall decreases, so is the effective permeability. Moreover, higher flowrate indicates higher loading rate of particles, which explains why the filter at 30,000 hr^{-1} flowrate had a lower permeability than 15,000 hr^{-1} at later time, though they have the same porosity.
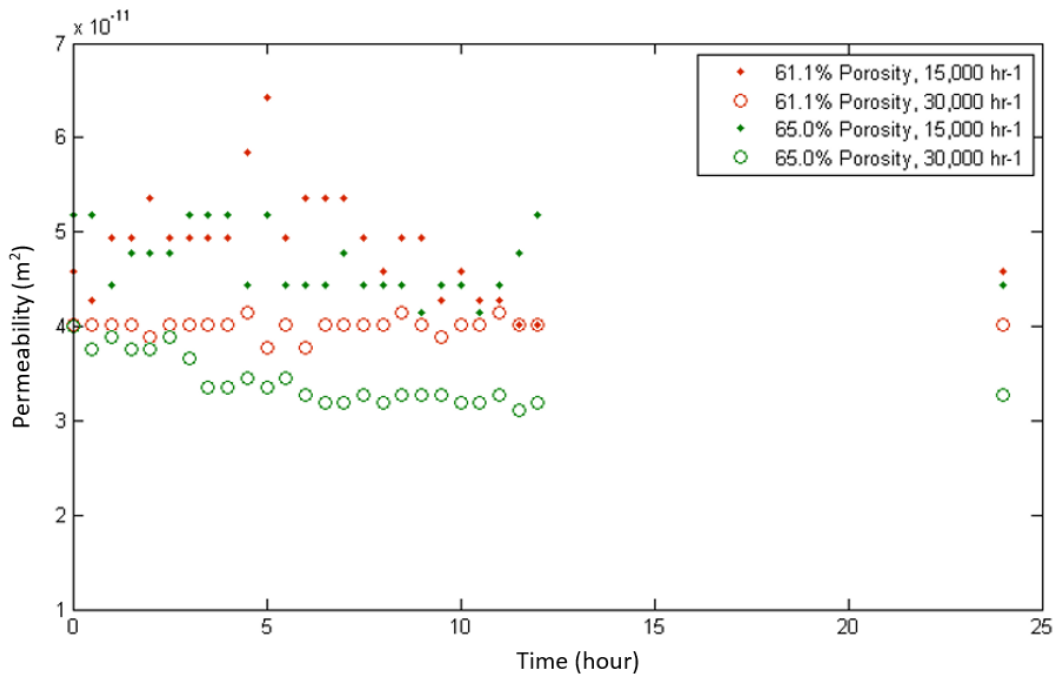
Figure 16. Effect of flowrate on permeability as calculated by the Darcy's Law.

31

In order to validate the new filtration model described previously, size dependent filtration efficiency of samples with different porosities at hour 0 (clean trap) were measured, meanwhile the same filter properties and flow conditions were modeled and simulated in Matlab. **Figure 17** compares experimental data points at 15,000 hr^{-1} and 30,000 hr^{-1} to model predicted filtration efficiency of clean filters given by solid lines. The figure also shows efficiency simulated by the original Opris model for the same fit factor values, denoted by dashed lines. The model validation study clearly reveals a good agreement of predicted filtration efficiency with experiments. The new filtration model proposed in this study shows improved fit to GDI sized particle filtration experiments compared to the Opris model. The over prediction of the modeled filtration efficiency of Opris model is primarily due to the presence of soot cake approximations. Since the soot cake can greatly increase filtration in DPFs, then the removal of soot cake approximations in the model, as done in this study, logically results in a lower modeled filtration efficiency.
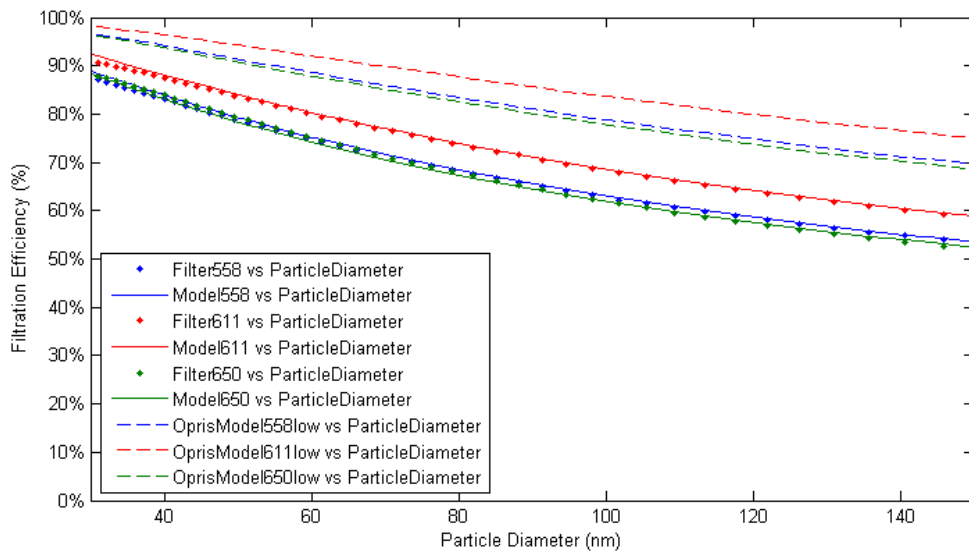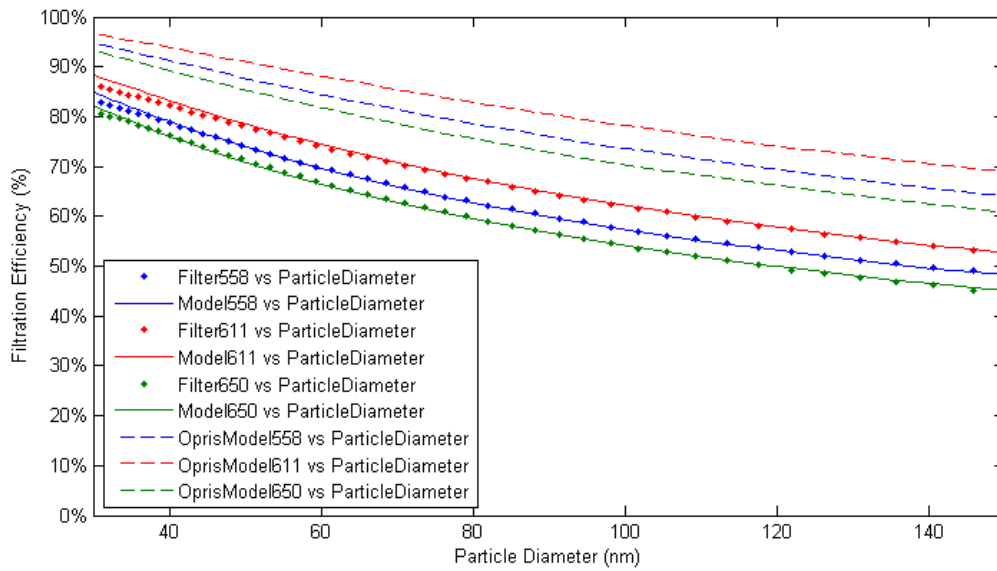
(a) 15,000 hr^{-1}

(b) 30,000 hr^{-1}

Figure 17. Filtration model validation and comparison at (a) 15,000 hr $^{-1}$ and

(b) 30,000 hr $^{-1}$.

Conclusions

This work investigated the size-dependent filtration efficiency of DPFs operating on particulate in the GDI size range. Three porosities (55.8%, 61.1% and 65.0%) of uncoated cordierite commercial DPFs were examined and a model capable of predicting the filtration efficiency as a function of particle diameter and system properties was developed. We demonstrated the impacts of porosity, inlet channel density and flow rates on the filtration efficiency of particulates in the GDI size range. The modified model agrees well with experiment, and represents an improvement over previous models. However, from the extended hour tests, we can see that the current DPF materials will not be sufficient to remove GDI particles from the exhaust. Proof of this is that the DPF samples took several hours to form a soot cake and reach an acceptable >95% filtration efficiency in the absence of any regeneration (since Ammonium Sulfate was employed instead of real exhaust soot particles). In the real situation where the filter is placed close coupled to the engine, cake formation will never happen due to the continuous regeneration conditions resulting from higher exhaust temperatures. Therefore, a DPF without soot cake will not be sufficient as a GPF. To meet the more stringent EURO 6 regulation, major modifications to the current filter technologies are essential and underway. Promising progress of GPFs can be achieved by making modifications from several perspectives, such as, reducing the material porosity, thinning the filter wall, and lowering the wall velocity. All these approaches can effectively increase the filtration efficiency of GDI particles while keep the pressure drop low, an important aspect for GDI engines. The major difficulty is in combing these approaches in the new GPF design and achieve balance between filtration efficiency and pressure drop. Given the accuracy of the new developed filtration model at GDI size range, it can be a useful tool to facilitate

GPF design by providing theoretical analysis before manufacturing prototypes and executing experiments.

CHAPTER III

MANUSCRIPT #2

Overview

The improved brake thermal efficiency of Gasoline Direct Injection (GDI) engines is accompanied by a significant increase in Particulate Matter (PM) mass and higher Particulate Number (PN) emissions as compared to (multi)Port Fuel Injected (PFI) engines. Gasoline-specific particulate filters (GPFs) with high filtration efficiency and low backpressure will be required to meet the future, stringent PM/PN regulations. A 2-D CFD study was performed to determine the effects of pore size and distribution on the interdependent performance parameters of filtration efficiency and backpressure. Simulation results show a nonlinear change in filtration efficiency as the pore size distribution tightens and determine a recommended distribution range, controlling the quantity of small size pores. Pore size distributions beyond this recommended range can cause a filtration performance loss or intolerable backpressure penalty for the GPF. In addition, a recent collaborative publication from our group has demonstrated our ability to create a hierarchical porous filter, with variable pore size in each layer. Knowing that filtration efficiency and pressure drop increase as the average pore size decreases, offers inspiration for a novel wall design with small pores comprising the top 40% of the wall layers and larger pores on bottom 60%. The model predicts that such a wall would result in an 8% increase in filtration efficiency.

Introduction

The pursuit of higher fuel efficiency from internal combustion engines (ICEs) has led to the rapid development of combustion strategies, such as gasoline direct injection (GDI). Compared to (multi)Port Fuel Injection (PFI) engines, GDI engines produce higher concentrations of both particulate mass and number, as shown in **Figure 18**[2-4]. It has long been known that nano-scale particles, such as those from GDI exhaust, can penetrate deep and deposit in the fine airways of the human respiratory system, such as the bronchioles and alveoli shown in **Figure 19**[5]. Studies have also shown that long-term exposure to fine particulate matter from exhaust can lead to severe cardiovascular issues such as myocardial infarction, heart failure and stroke[6].
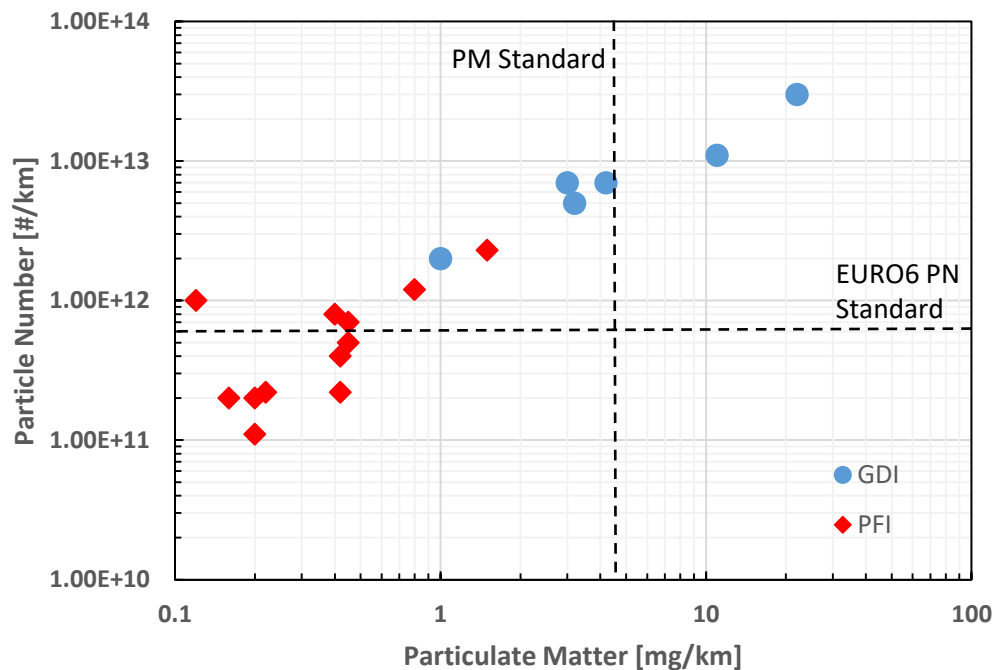
Figure 18. Particulate mass and number emissions from GDI and PFI engines based on the data from[2], with the proposed standards shown by the vertical and horizontal dash lines.
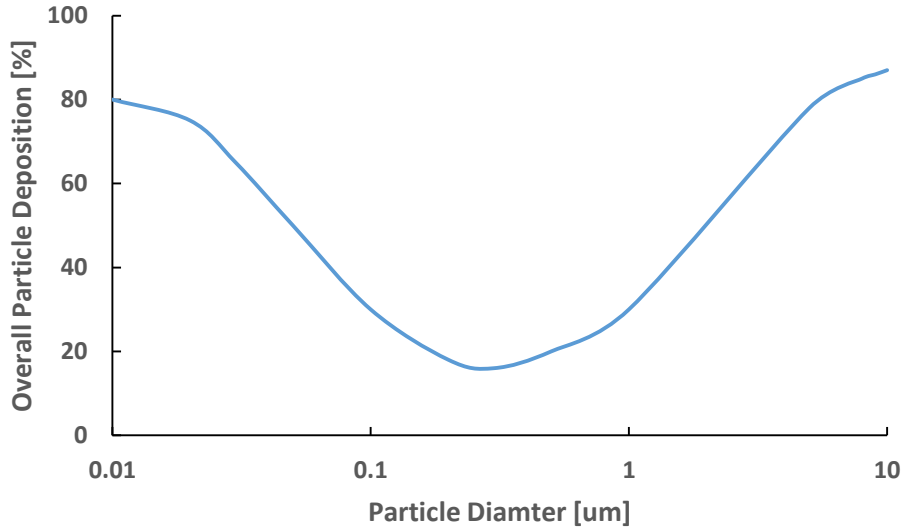
Figure 19. Small size particles, such as GDI PM, have been shown to have high deposition rates in the fine airways, where they can later pass into the blood. The plot is based on data from[5].

In response to the aforementioned health issues and the well-known environmental consequences, regulatory agencies in the United States, Europe and Japan have proposed stringent regulations to control PM and PN emissions. California Air Resources Board (CARB) LEVIII and U.S. EPA Tier 3 guidelines[7] reduce the allowable mass emissions from the previous level of 10 mg/mile to 3 mg/mile. In Europe, the current EURO 6 number standard requires PN emissions to be less than 6×10^{11} particles/km. Additionally, Asian markets such as China and India, have begun to create their own regulations to control particulate emissions[46]. These global and domestic regulations make the design of GDI engines and exhaust after-treatment system challenging. Currently, most vehicles on the market exceed the EURO 6 PN regulations at cold start[8], as shown in **Figure 20**. Therefore, an advanced, gasoline-specific filter with high filtration efficiency will be required in order to meet regulatory limits.
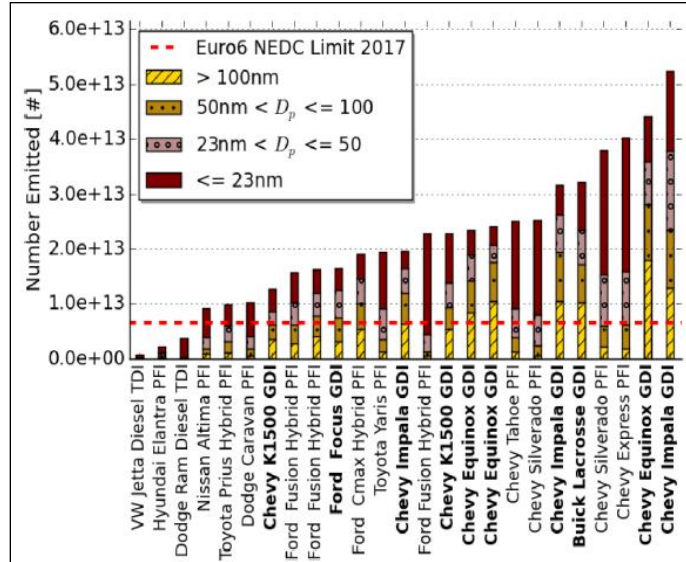
Figure 20. Vehicle PN emissions during cold start[47].

Diesel Particulate Filters (DPFs) are ceramic, wall-flow filters that have been used to reduce particulate emissions for nearly two decades [9, 10, 48], with high (>90%) filtration efficiency. However, despite the success of the application of DPFs with diesel engines, they are not a good solution for GDI engines for two main reasons. First, the concentration of particulates in exhaust is much higher from diesel than GDI engines[2-4] and at the same time, diesel particles are larger in size. This leads to the rapid formation of soot cake on surface of DPF wall and is responsible for why they quickly achieve high filtration efficiency [13-15]. In contrast, due to the smaller size and lower concentration of GDI particles, the absence of soot cake formation and the relatively larger pore sizes make DPFs insufficient for GDI aftertreatment[16]. Second, GDI engines are more sensitive to back pressure[17]. Filters that have a high overall pressure drop can choke the engines and eventually cause power loss. Therefore, there is a need for specific GPFs with high filtration efficiency and low pressure drop to meet the ever stringent PM and PN regulations.

The overarching objective of this work is to examine how to increase GPF filtration efficiency, while keeping the pressure drop low. CFD modeling is the primary tool used to achieve this. Modeling efforts began decades before the requirement of DPFs on engine with analytical modeling of particulate filters due to its low cost, ease of adjusting filter properties and high fidelity results. The core of analytical model is based on the "packed bed" theory, proposed by Payatakes[18] in early 1970s to simulate porous media filtration processes. The theory assumes numerous monodisperse grains (unit collectors) are connected in parallel to form a packed bed. Lee[19] employed the Kuwabara [20] model of forces on a multiplicity of spheres in a viscous fluid, to simulate the filtration of aerosol particles through a packed bed. Later in 1980s, Bissett[9] proposed a mathematical model of thermal regeneration of a wall flow monolith DPF. Furthering Bissett's work, Konstandopoulos and Johnson[10] developed an analytical model to predict the time-dependent pressure drop and particulate collection characteristics as a result of soot loading. The classic filtration model assumes homogeneity of the wall substrate and derives the unit collector size assuming a constant wall porosity and characteristic pore size. However for most commercial cordierite filters, the substrate pore size can have a large pore size distribution. To account for this non-homogeneity of the filter wall, Gong developed a PDF-based heterogeneous multiscale filtration (HMF) model[49]. The HMF model has proven to be a useful tool to study the microstructure effects of GPF on GDI-sized particle filtration behavior[21, 22]. Despite the large advances made by the HMF model over the classic filtration model, it is still an analytical model at its core using a statistical method to resolve the probability density function of the GPF wall pore sizes. Fluid dynamics dictates that the microstructure of the GPF porous wall has a critical role in filtration characteristics and overall pressure drop[27] and more complex interactions between different sized pores, specifically how randomly dispersed small size pores

influence the flow in large pores, is still in need of investigation. CFD is a numerical method that can offer high fidelity flow field results for complex geometry, making it an ideal tool to study particle-laden flow in GPFs.

A 2-D CFD study of pore size and distribution effects on GPF performance metrics, namely filtration efficiency and pressure drop, is conducted in this study and provides detailed flow field information and particles motion trajectories within the substrate. This information is crucial in terms of understanding the dynamic interactions between particles and wall microstructure, and is able to suggest a porous wall design to further optimize GPFs.

Approaches

ANSYS FLUENT is the primary tool for numerical simulation in this study. Prior to the CFD simulation, a 2D geometry was established to accurately capture the characteristics of a sample GPF substrate (**Table 1**), including porosity and pore size distribution (**Figure 21**). This geometry and its corresponding CFD simulation results are taken as the baseline, to which further simulation results are compared.

Table 1. Sample GPF wall properties

Sample GPF Wall Properties	
Cell Density in cpsi	300
Wall Thickness t in mil	12
Porosity ε	0.65
Mean Pore Size $\hat{d}_p$ in μm	15
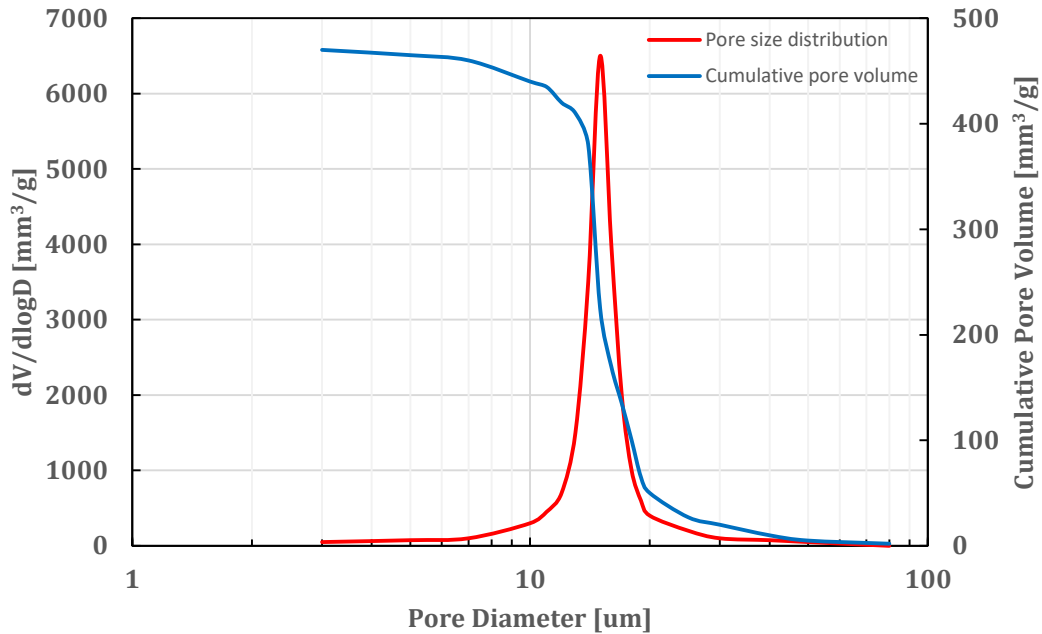
Figure 21. Sample GPF wall substrate pore size distribution and cumulative pore volume profile based on the mercury porosimetry data.

An array of "circular obstacles" is created, surrounding cavities in the middle. The cavities represent the physical void space observable in SEM images from Ford (**Figure 22**)[7]. The gaps between circular obstacles (in both horizontal and vertical directions) represent pores in the GPF substrate. These pores link the void space together and serve as flow paths for gas and particles. By altering the size of the gaps, different pore sizes can be simulated. Instead of focusing on air flowing over obstacles like the classic "packed bed" theory, this model focuses on air traveling through cavities via different sizes of pores, as indicated in **Figure 23**.
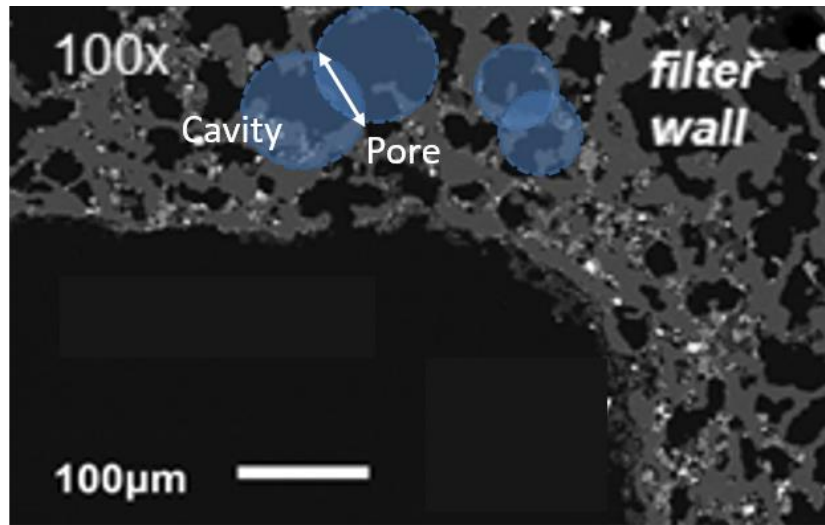
Figure 22. SEM image of a typical GPF wall, showing the cavities and pores microstructure.
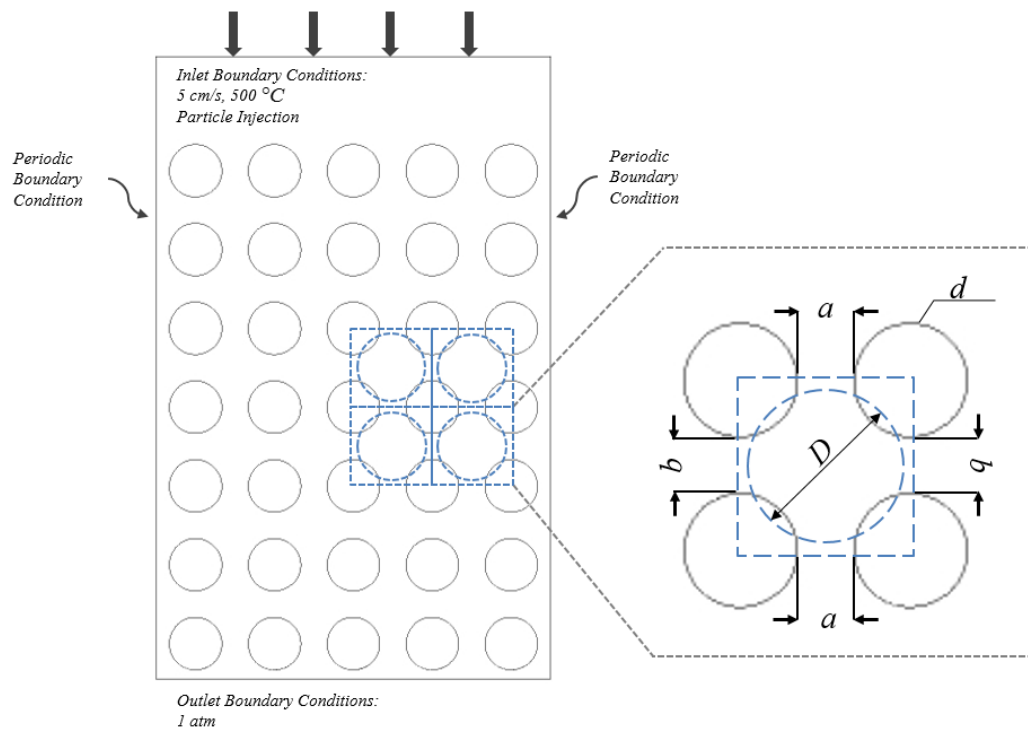
Figure 23. The GPF wall is described by an array of "circular obstacles". The cavities that exhaust flows through are represented by blue dashed lines. Where d is the diameter of the obstacle, a is the horizontal pore spacing; b is the vertical pore spacing, and D is the diameter of the cavity.

For a monodisperse wall model, meaning pore size (a and b in **Figure 23**) stay fixed, cavity size D needs to satisfy equation (17) below to match the porous wall property. Meanwhile, the number of layers of circular obstacles are determined by equation (18).

$$\varepsilon = \frac{\pi(\frac{D}{2})^2}{(d+a)\cdot(d+b)} \tag{17}$$

$$n = \frac{t}{d+b} \tag{18}$$

Where, ε is the porosity of GPF wall; a,b is pore size; d is the diameter of circular obstacle; D is the diameter of cavity, and n,t indicates the total number of obstacle layers and GPF wall thickness.

The particle-laden gas is introduced at the top of the wall at $500°C$, with velocity 5 cm/s to simulate the real working condition of the GPF. The flow across the wall remains laminar with Reynolds number well below 1. The boundary condition of 1 atmosphere of pressure is assumed at bottom of the wall. Additionally, we assume steady state, incompressible flow.

Once the flow field in wall substrate is calculated and fully converged, particle tracking is performed to predict the size-dependent filtration efficiency. Both Brownian diffusion and drag, corrected by Stokes-Cunningham factor, are considered while tracking particles using the Lagrangian method. The particles are counted as "trapped" if they hit the circular obstacles, and their trajectories are terminated. Particles that travel out of the wall are not captured and instead counted as having broken through. **Figure 24** shows a typical flow field and particle trajectories simulation results of a 2-D GPF wall model, from which crucial information like velocity and pressure field at particular regions, or particle motion and impact locations, can be retrieved conveniently.

(a)   (b)
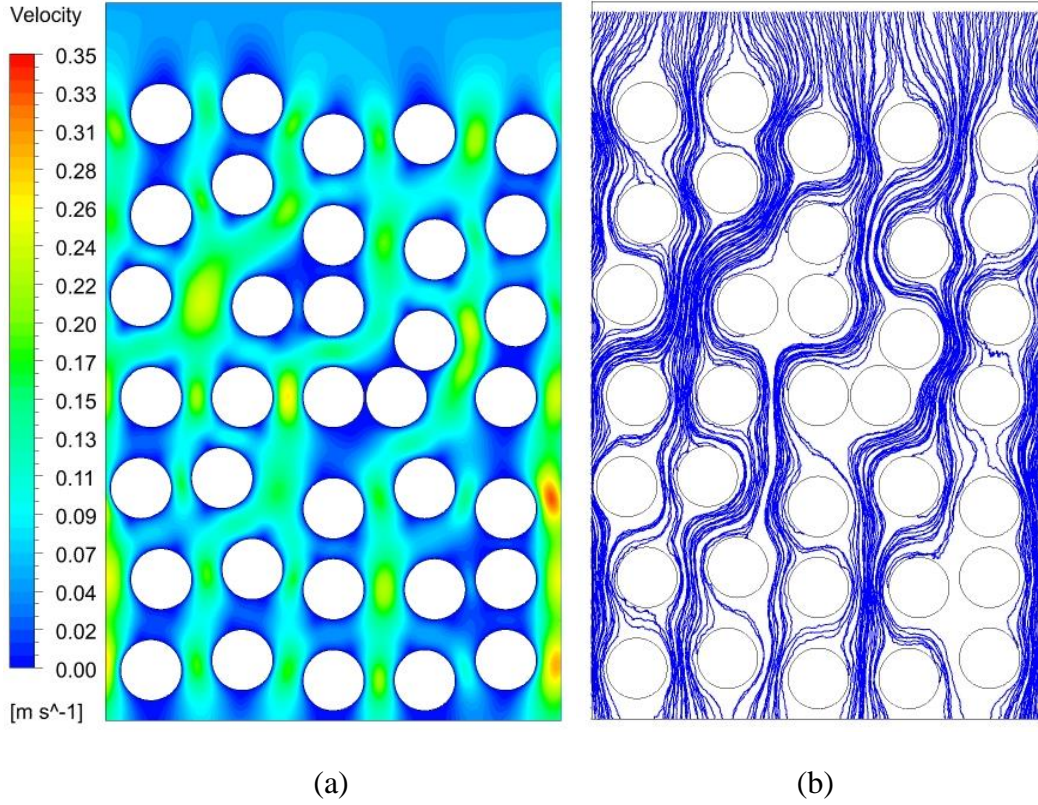
Figure 24. (a) Flow field and (b) particle tracking results of a typical CFD study.

Equation (19) is used to calculate the size-dependent filtration efficiency. Due to the particle size of interest in this study, we assume Brownian diffusion is the dominant capture mechanism and neglect interception and direct impaction. For GDI-sized particles of 75 nm diameter, both the Stokes Number and particle collector diameter ratio are much smaller than 1, which makes interception and impaction related filtration efficiency about two orders of magnitude lower than diffusion related efficiency.

$$E = \frac{N_{trapped}}{N_{injected}} \tag{19}$$

Where E is the total filtration efficiency across the wall; $N_{trapped}, N_{injected}$ is the total number of particles trapped in the wall and the total number of particles injected into the wall.

The pressure drop calculated by the CFD simulation is compared to the 0-D pressure drop model based on Darcy's Law, with permeability approximated by the Rumpf & Gupte correlation (Equation (20))[50].

$$k = \frac{\varepsilon^{5.5}}{5.6} d^2 \qquad (20)$$

Where, k indicated the predicted permeability of GPF wall; ε is the wall porosity and d is the diameter of the circular obstacle.

The Baseline Condition

An array of "circular obstacles" with seven layers and a total of 70 pores was created as the baseline geometry. Out of the 70 pores, half are in the horizontal direction, and the other half are vertical. Pores in each direction are configured to match the measured pore size distribution of the sample GPF described in **Table 2** and **Figure 25**. The layout is shown in **Figure 26.**

Table 2. Quantity of different sized pores in the 2D baseline geometry

Baseline, $\hat{d}_p = 15\mu m, d = 30\mu m$		
Pore Size (um)	# on Horizontal	# on Vertical
0	1	1
5	2	2
10	8	8
15	16	16
20	5	5
25	2	2
30	1	1
Total	35	35

(a)   (b)
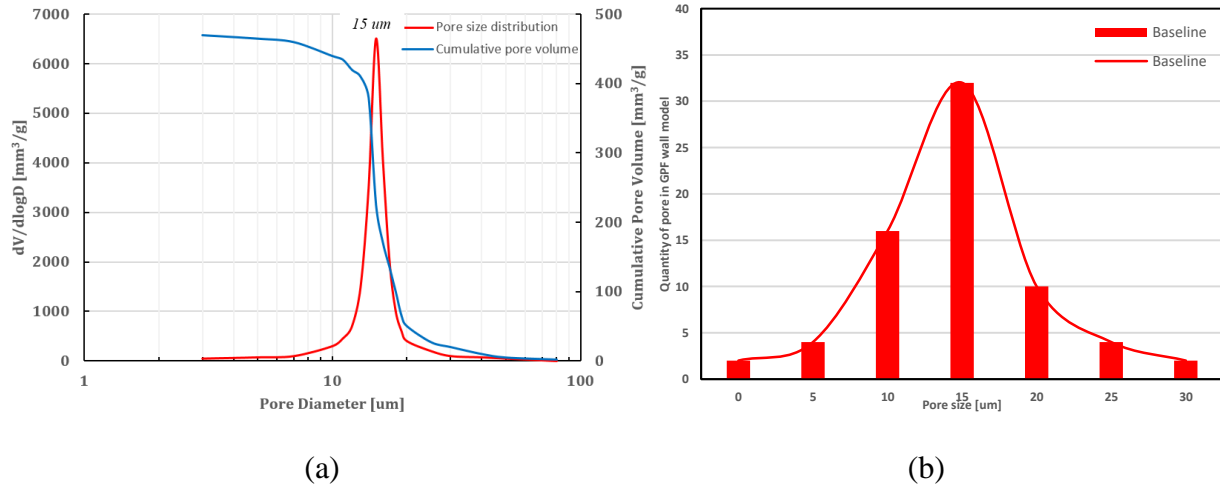
Figure 25. Measure baseline pore size distribution of the sample GPF in (a) logarithmic scale and (b) stacked column graph. The quantity of each pore sized is elaborated in Table 2.
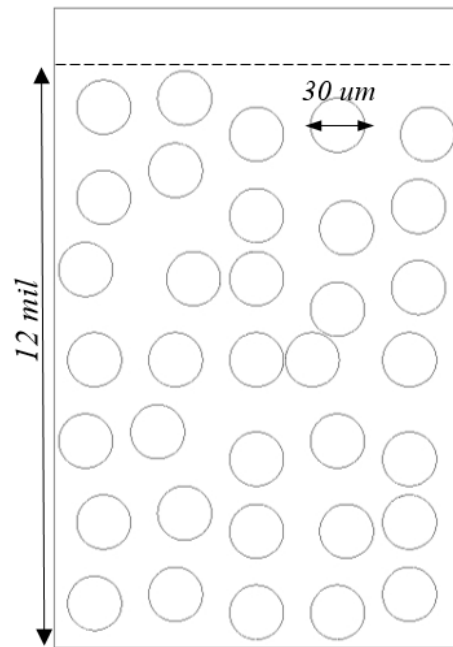
Figure 26. Depiction of the 2-D CFD wall geometry for the baseline pore size distribution.

Study of the Effects of the Tighten/Widen Pore Size Distribution

On the basis of the measured baseline pore size distribution of the sample GPF, the distribution is further reconfigured to simulate different possible wall properties, by stretching and tightening the distribution curve. This distribution reconfiguration (mean pore size stay fixed) aims to investigate the pore size distribution effects on GPF filtration and pressure drop performance. The tight distribution is narrow, with less variation with respect to the mean pore size (**Figure 27**). The most extreme scenario for a tightened distribution is monodisperse, with the pore size fixed at $d_P = 15\mu m$. The wide distribution is an expanded curve, possessing heavier tails on both ends. The exact variance of each distribution compared to the baseline distribution is explicitly enumerated in **Table 3**. All properties stated in Table 1 remain the same. The pores layouts for each distribution are shown in **Figure 28**.

(a)   (b)
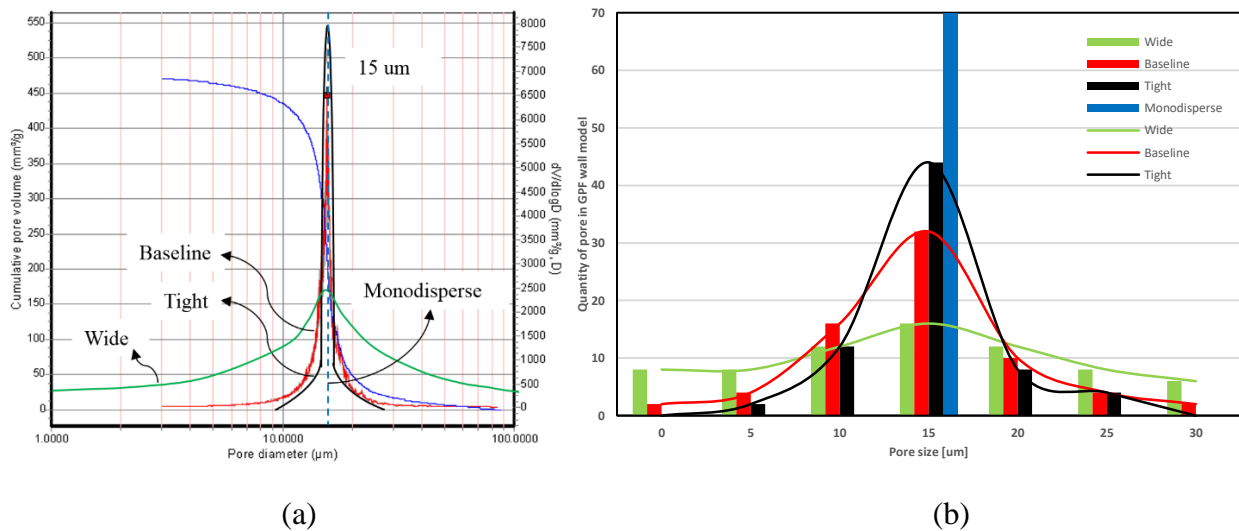
Figure 27. Depiction of the baseline pore size distribution and its wide, tight and monodisperse variations in (a) logarithmic scale and (b) arithmetic scale and stacked column graph. Variance is elaborated in Table 3.

Table 3. Quantity of different sized pores in the 2D geometry for the wide, tight and monodisperse cases

Pore Size (um)	Wide, $\hat{d}_P = 15\mu m,\ d = 30\mu m$		Tight, $\hat{d}_P = 15\mu m,\ d = 30\mu m$		Monodisperse, $d_P = 15\mu m,\ d = 30\mu m$	
	# on Horizontal	# on Vertical	# on Horizontal	# on Vertical	# on Horizontal	# on Vertical
0	4	4	0	0	0	0
5	4	4	1	1	0	0
1	6	6	6	6	0	0
1	8	8	22	2	35	3
2	6	6	4	4	0	0
2	4	4	2	2	0	0
3	3	3	0	0	0	0
T	35	3	35	3	35	3
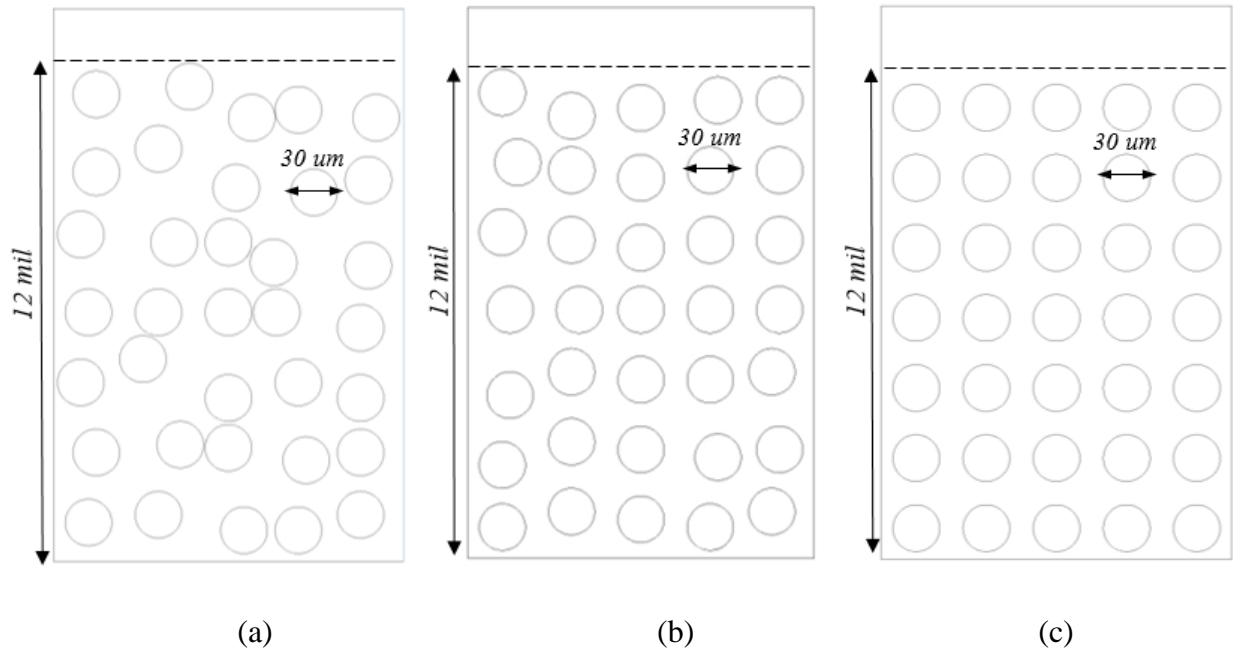
Figure 28. The 2-D CFD wall geometry with (a) wide pore distribution, (b) tight pore distribution and (c) monodisperse pore distribution.

To consider the randomness of the circular obstacles layout in the GPF wall model, and its potential impact on the particle filtration efficiency, a GPF wall model with staggered obstacle layout is created on the basis of the regular wall model with relatively orderly obstacle layout. The staggered obstacle layout is created by translating obstacles in every other row to left or right by a distance of $\frac{d+a}{2}$, where d is the circular obstacle diameter and a is the pore size. The monodisperse wall model with staggered obstacle is shown in **Figure 29** below. The CFD study and particle tracking will be conducted in the staggered model and the predicted filtration efficiency for a specific particle size is denoted as E_R. The predicted E_R for aforementioned pore size distributions, including the baseline, wide, tight and monodisperse are shown **Figure 30**, in comparison with the orderly layout wall model filtration efficiency E. The comparison shows that the tighter the pore size distribution is possessed by the GPF wall model, the heavier influence will the obstacle randomness has on the particle filtration efficiency. The monodisperse pore size distribution case sees the largest disparity between the orderly and random obstacle layout. The final size-dependent filtration efficiency $\hat{E}$ for GPF wall model with certain pore size distribution is calculated by averaging E and E_R.

$$\hat{E} = \frac{E + E_R}{2} \tag{21}$$

The staggered layout is created purely for the final filtration efficiency calculation and comparison between various pore size distributions. For more details about the CFD predicted in wall flow field and pore size's effect on the flow field, investigations are made on the basis of the wall model with orderly obstacle layout.
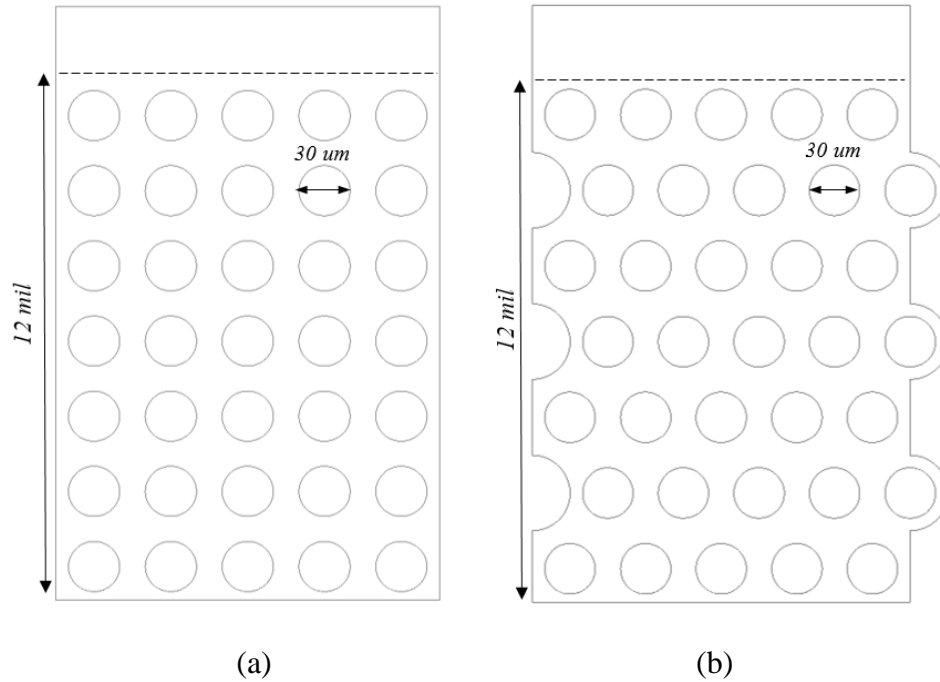
Figure 29. GPF wall models for the same pore size distribution, with (a) orderly obstacle layout and (b) staggered obstacle layout.
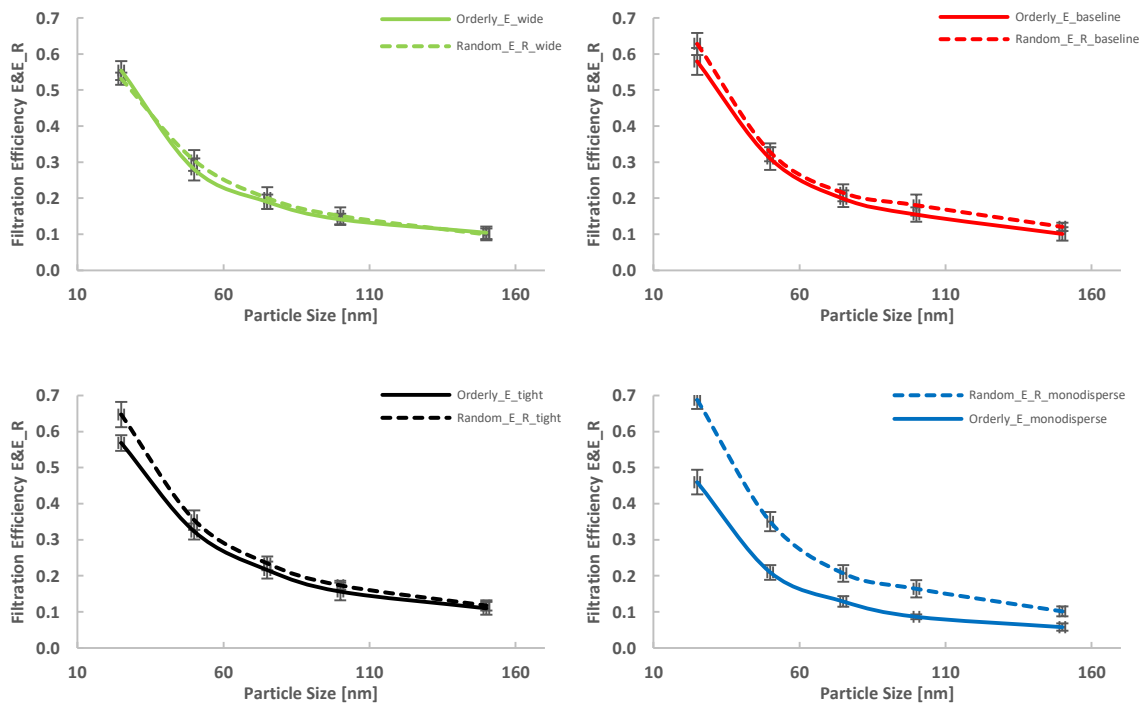
Figure 30. Size-dependent filtration efficiency of random and orderly circular obstacle layout GPF wall model for the baseline, tight, wide and monodisperse pore size distribution.

Average Pore Size Sensitivity Study

To investigate the impact of the average pore size, the baseline distribution is shifted to left or right by $5\mu m$, therefore all pore sizes decrease or increase by $5\mu m$ simultaneously. The resultant distributions are shown in **Figure 31**. All other GPF properties remain fixed. The circular obstacles layouts are indicated in **Figure 32**.
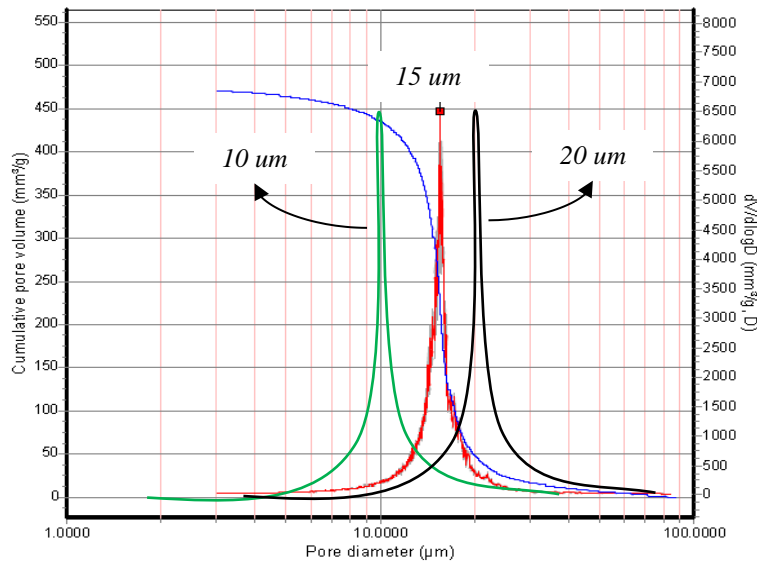
Figure 31. The baseline pore size distribution (a) shifted to right, with average pore size of 20 um; (b) shifted to left, with average pore size of 10 um.
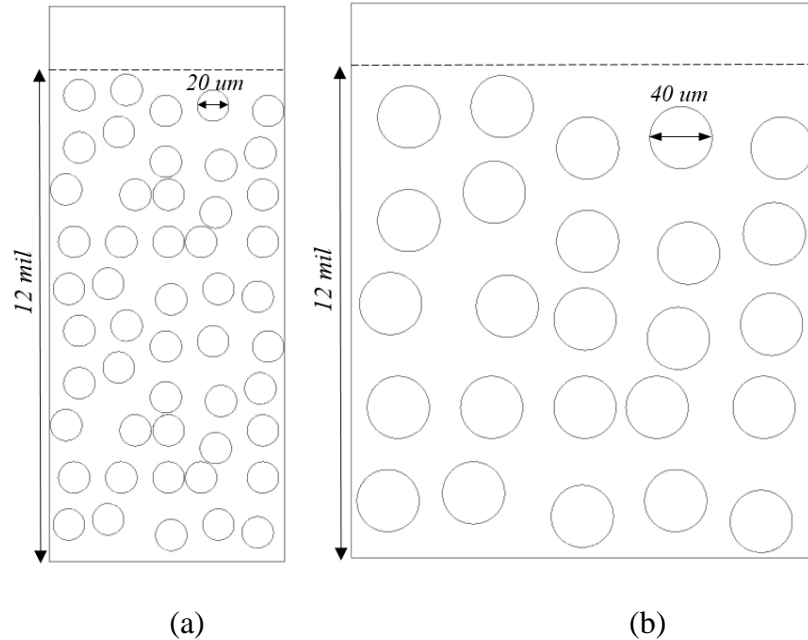
Figure 32. The 2-D CFD wall geometry with baseline pore size distribution (a) shifted to the left, with average pore size of 10 um and (b) shifted to the right, with average pore size of 20 um. The wall thickness and porosity remain unchanged from the baseline condition.

The CFD model was validated for the baseline condition with experimental data, from Dinex GPFs. The GPF sample was evaluated at room temperature, at 30000 hr^{-1} space velocity. Size-dependent filtration efficiency of incident ammonium sulfate particles was measured using a TSI Scanning Mobility Particle Sizer (SMPS) and the pressure drop was measured by a MKS differential pressure transducer[16]. This validated CFD model was then run for the matrix of geometries described earlier to study the pore size and distribution effects on GPF performance. Only particles smaller than 150nm are considered in the simulation because majority of GDI particulates fall into this size range [51, 52]. Ten particle-tracking simulations were conducted for each wall geometry in order to calculate an average size-dependent filtration efficiency. This approach can lessen the impact of the randomness introduced in the model by particles following Brownian diffusion. Results of the averaged filtration efficiency and pressure drop are compared

to results from the baseline condition, to provide insight and inspirations for what wall features would create a better GPF[53].

Results and Discussion

Model Validation

To validate the FLUENT model's capability in predicting GPF wall filtration efficiency, the "circular obstacles" in the 2-D GPF wall model for the baseline condition was reconfigured to match the "unit collector" size in the Konstandopoulos filtration model, derived by equation (22).

$$d_c = \frac{3}{2}\frac{1-\varepsilon}{\varepsilon}d_p \tag{22}$$

Where d_c is the unit collector diameter; ε is the wall porosity and d_p is the pore size.

As shown in **Figure 33**, at the same working conditions, the CFD simulation yields size-dependent filtration efficiency results close to both experimental results and the O-D model for particle sizes in the range of 50 nm to 150 nm. This additionally validates the assumption of Brownian diffusion as the dominate filtration mechanism for GDI-sized particles. This study decided to take a unique route and used larger sized "circular obstacles" compared to classic unit collector to create the baseline 2-D CFD geometry, in order to better represent real GPF wall microstructure. This geometry with "circular obstacles" enables the model to match both porosity and pore size distribution of the real Dinex GPF sample, while classic unit collector model can only recreate the wall porosity.
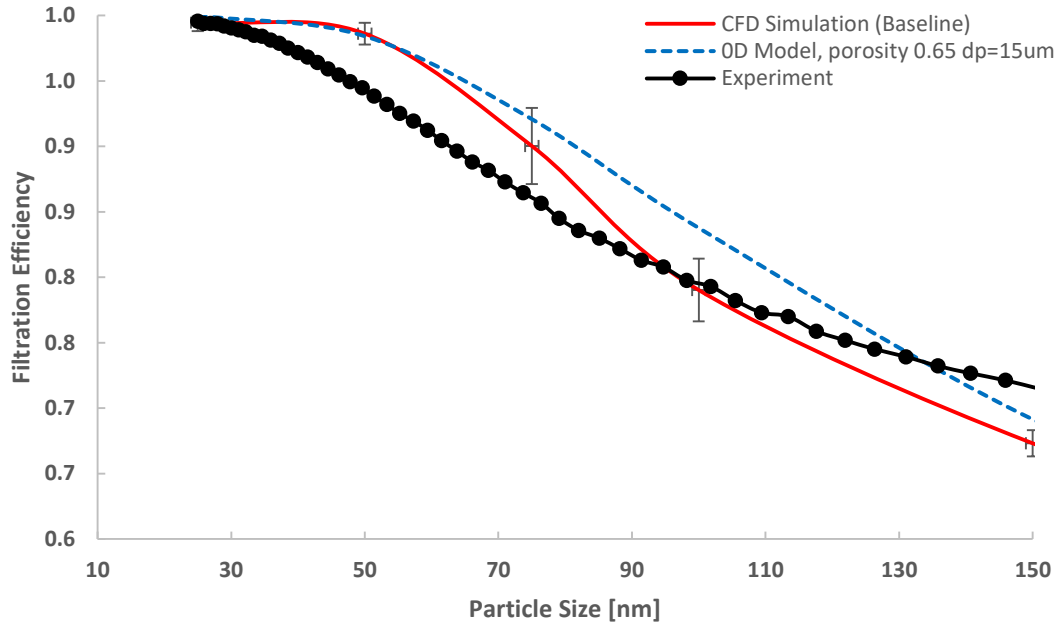
Figure 33. Size-dependent filtration efficiency comparison between the 2-D CFD simulation described in this work, the 0-D model and experiment.

Effects of a Tightened Pore Distribution

By comparing the curves in **Figure 34**, it is possible to observe the trend that average filtration efficiency first increases and then decreases as pore size distribution tightens up. For GDI-sized particles, a bar chart, **Figure 35,** showcases this nonlinear trend and indicates the potential for optimizing the pore size distribution, for maximum filtration efficiency, as a function of particle size.
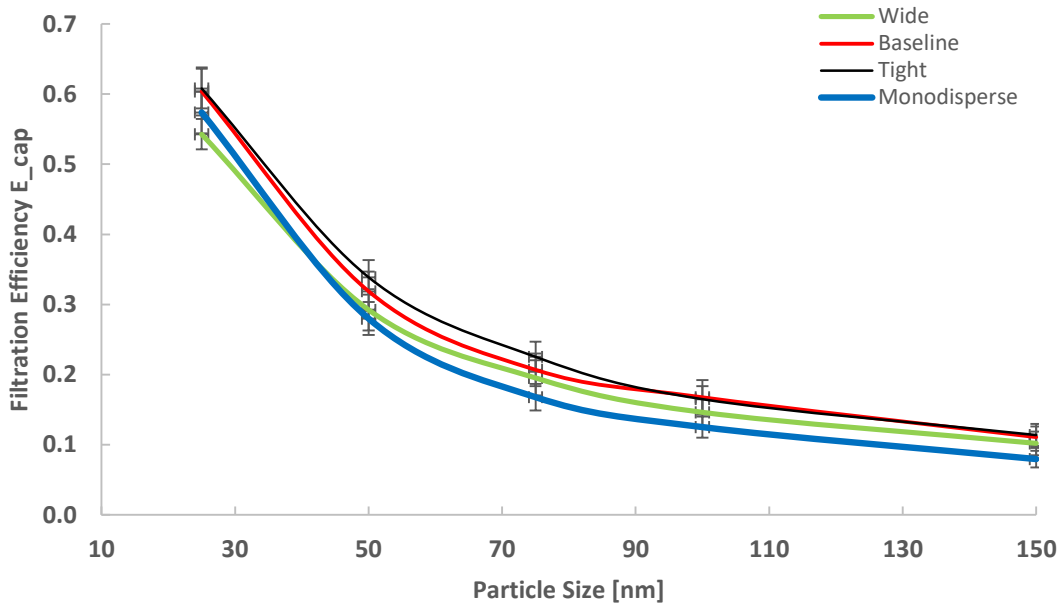
Figure 34. Size-dependent filtration efficiency $\hat{E}$ for the baseline, tight, wide, and monodisperse pore distributions. For details of the quantities of different pore size for each pore size distribution, please refer to Table 3.
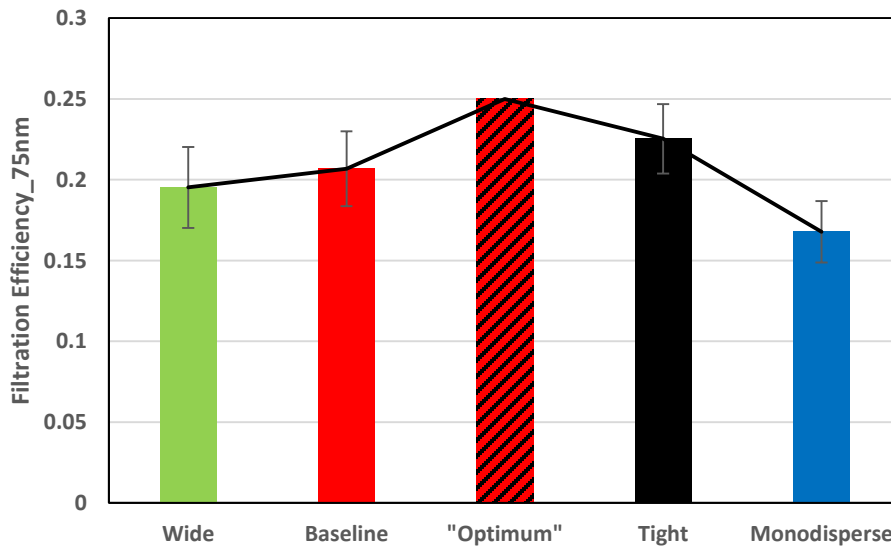
Figure 35. Filtration Efficiency Comparison for 75 nm particles between various pore size distributions in this study indicates the potential existence of an "optimal distribution". For details of the quantities of different pore size for each pore size distribution, please refer to Table 3.

Analysis of the velocity contours of the baseline and tight pore distributions can be used to explain the nonlinearity of the trend. Shown in **Figure 36**, the velocity contour plot for the baseline condition has more locations of high flow velocity. This is because flows from parallel canals are more likely to merge due to the large quantity of small pores. High flow velocity will weaken the impact of Brownian diffusion on GDI-sized particles, which can lead to a decrease in filtration efficiency. Also due to the number of small pores, flow bypasses occur more often with relatively low velocities. These low flow regions enhance the diffusion related particle filtration and consequently increase the efficiency. Therefore, the existence of both high flow regions and low flow regions can counteract each other, making the performance of GPF with the tight pore distribution nearly identical to baseline.
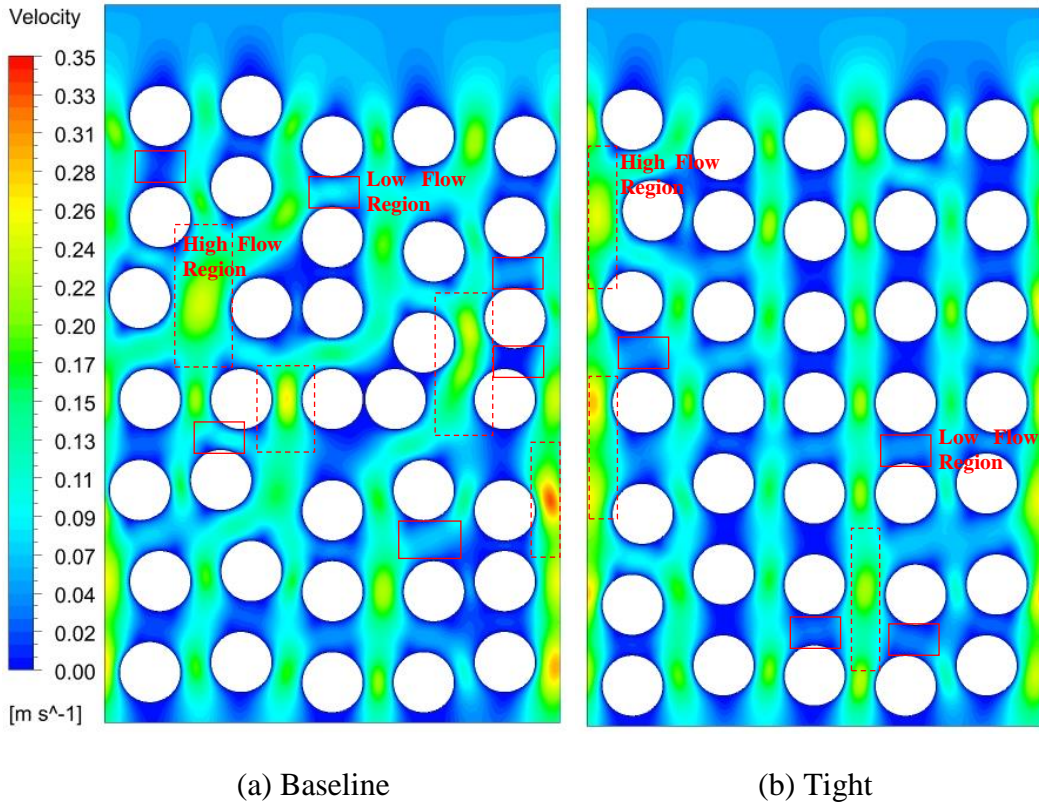
Figure 36. Velocity contours of the (a) baseline and (b) tight pore distributions. High flow velocity regions due to flow merging are marked by red dashed rectangles; Low flow regions resulting from divergence are marked by red solid line rectangular.

To further support these conclusions, **Figure 37** offers a look at the particle movements inside the wall. For the baseline case, more particles are trapped in the low flow bypasses that happen more frequently than in the tight pore distribution case. Particles in the high flow regions are less likely to be trapped because of the weak diffusion effect. There are also regions in baseline case, where only a small fraction of the flow and particles are able to go through due to being influenced by the small pores upstream. As a result, these regions do not contribute to the filtration functionality.
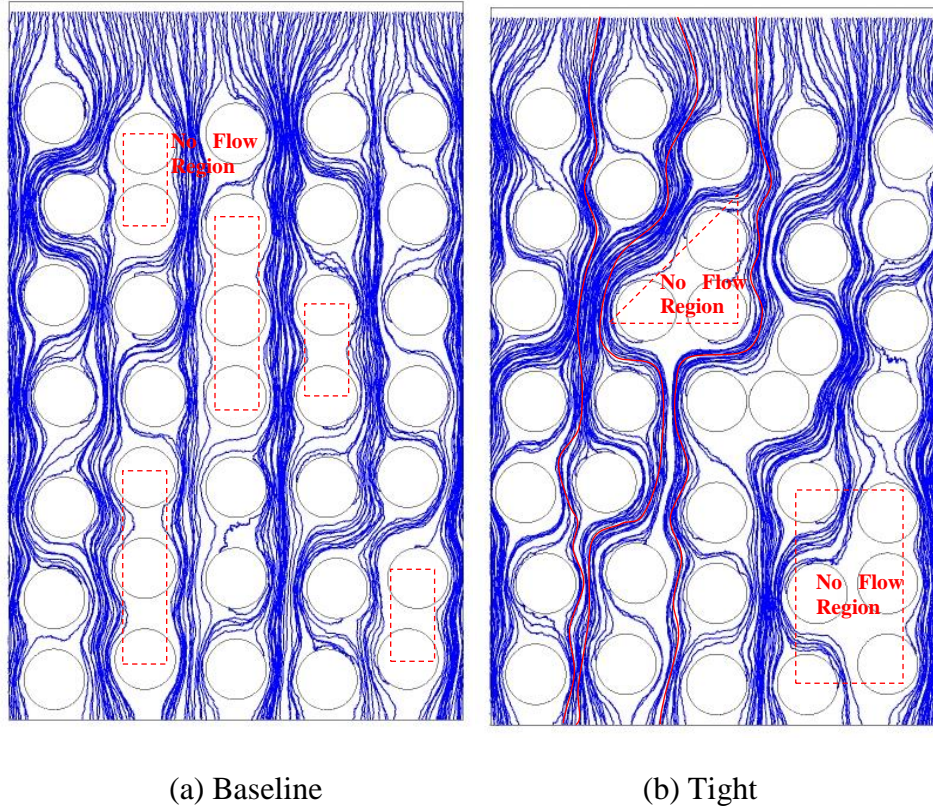
(a) Baseline   (b) Tight

Figure 37. Particle tracking for the (a) baseline and (b) tight pore distributions. Three numbered streamlines shown in red, are singled out to show flow divergence and merging. Regions with low or no flow are marked by red dashed rectangles.

The simulations show that GPF walls with tight pore size distributions have a small impact on the overall filtration efficiency, but have a large impact on local flows, which can be seen from the particle tracking in the wall. A tighter pore size distribution eliminates small pores in the wall, resulting in particle-laden flow tending to travel linearly, without divergence and bypasses. In the specific tight pore distribution investigated in this study, pores in the vertical direction are barely used for filtration functionality. Similarly, for the more extreme monodisperse distribution case, none of the vertical pores are used for filtration, dramatically lowering the filtration efficiency. In contrast, the baseline and wide pore distribution cases have more incidences of flow bypass, favoring filtration. However, it is worth noting that the very small pore sizes ($0 < a \le 5\mu m$)

completely stop the flow from passing through and cause a void space downstream. The wide pore distribution suffers from choked flow more than baseline due to a larger quantity of small size pores.

These observations point to the potential for an "optimum pore size distribution", that would occur in between the baseline and tight pore distributions described in this study. This hypothesized "optimum pore size distribution" should have pores small enough ($a < 10 \mu m$) to diverge the flow and large enough ($5 \mu m < a$) to allow a fraction of flow pass, which is the balance of actions needed for particle filtration. The detailed "optimum pore size distribution" is enumerated in **Table 4**, and further shown in **Figure 38**, in comparison with the baseline and tight distributions. The filtration efficiency comparison between such an "optimum", baseline and tight is shown in **Figure 39**. The hypothesized "optimum distribution" yields filtration efficiency close to that of the baseline and tight cases across all particle sizes.

Table 4. Quantity of different sized pores in "optimum distribution" comparing to the baseline and tight distribution

Pore Size (um)	Baseline, $\hat{a}_p = 15 \mu m, d = 30 \mu m$		Tight, $\hat{a}_p = 15 \mu m, d = 30 \mu m$		"Optimum", $\hat{a}_p = 15 \mu m, d = 30 \mu m$	
	# on Horizontal	# on Vertical	# on Horizontal	# on Vertical	# on Horizontal	# on Vertical
0	1	1	0	0	0	0
5	2	2	1	1	2	2
1	8	8	6	6	7	7
1	16	1	22	2	19	1
2	5	5	4	4	5	5
2	2	2	2	2	2	2
3	1	1	0	0	0	0
T	35	3	35	3	35	3
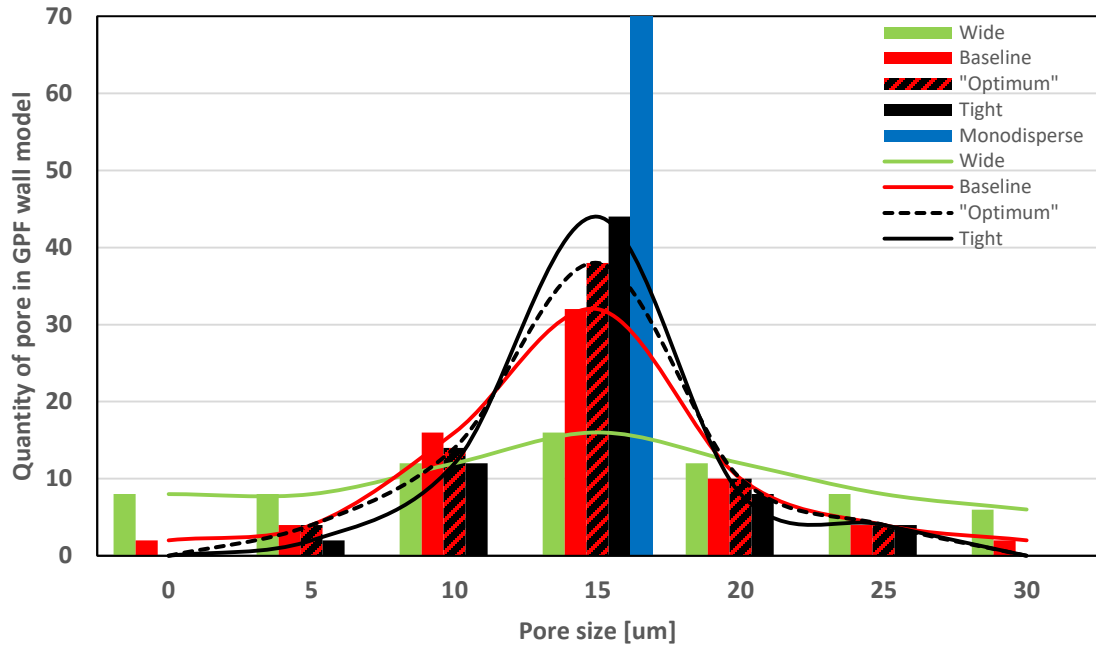
Figure 38. The hypothesized "Optimum pore size distribution" in stacked column graph, next to the baseline, wide, tight and monodisperse distribution. The quantity of each pore size in the "Optimum" distribution is elaborated in Table 4.
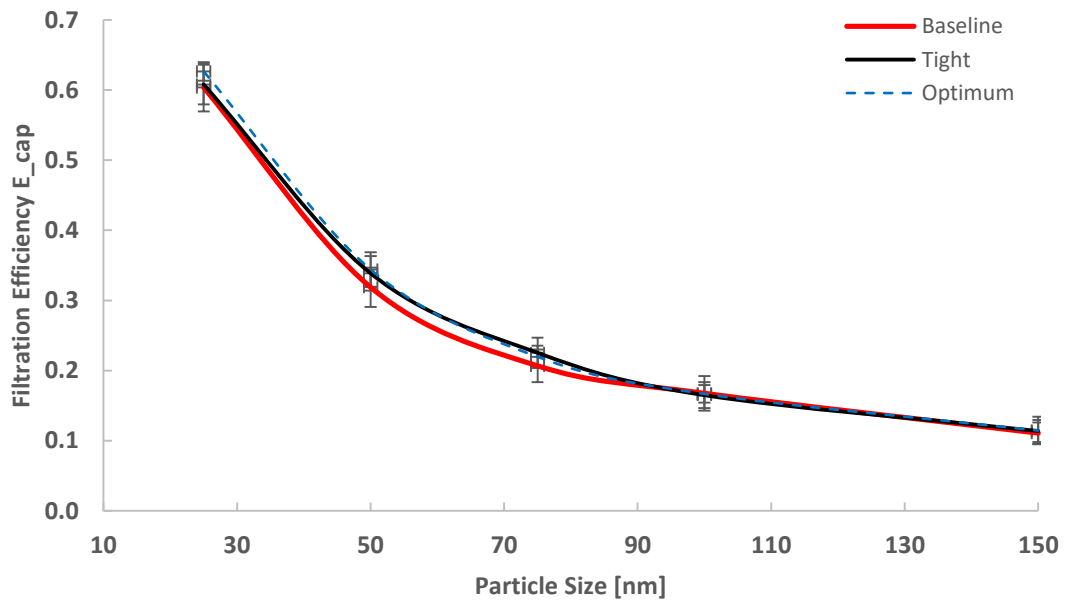
Figure 39. The hypothesized "Optimum pore size distribution" shows similar filtration efficiency with the baseline and tight cases at nearly all particle sizes.

Therefore the singular hypothesized "optimum pore size distribution" doesn't exist, and instead a pore size distribution range is recommended to filter suppliers in order to achieve full potential of GPFs. As indicated in **Figure 40** and previous discussion, for the GPF sample in this study with fixed mean pore size and porosity, pore size distribution is recommended to be restrained between the baseline and the tight distribution. Beyond the recommended pore size distribution range, neither too wide nor too tight distribution is good to the GPF filtration performance.
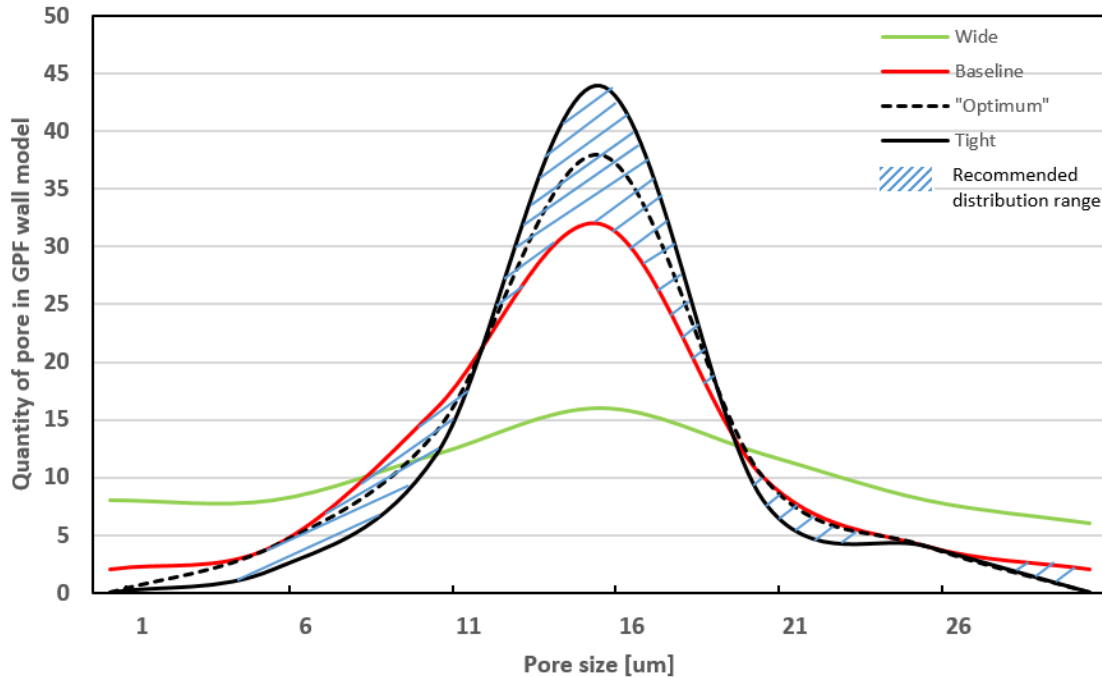
Figure 40. Recommended range of pore size distribution for sample GPF.

The 2-D CFD simulation can also provide a relatively accurate pressure drop estimate for the porous wall, as compared to 0-D model as shown in **Table 5**. Similar to the filtration efficiency calculation, CFD predicted pressure drop for each pore size distribution is an average of the orderly and random obstacle layout. The pressure drop comparison indicates a linear increase of pressure

drop as pore size distribution tightens. Usually pore size distributions with high filtration efficiency also yield high pressure drop across the GPF wall due to longer distance flow travels through the wall. This explains why pore size distribution between the baseline and the tight has higher pressure drop than wide case. For monodisperse case, the even higher pressure drop is attributed to the random obstacle layout variation, which produces a higher pressure drop than the orderly layout variation. However the random layout variation to the monodisperse case doesn't produce filtration efficiency high enough to compensate the orderly layout variation. Therefore, the monodisperse pore size distribution is not recommended due to its low filtration efficiency and high pressure drop.

Table 5. Pressure drop comparison.

	Pressure	0D	Difference
Wide	35 Pa	36 Pa	2.8%
Baseline	39.5 Pa	36 Pa	9.7%
Tight	40.5 Pa	36 Pa	12.5%
Monodisperse	42 Pa	36 Pa	16.7%

Effects of Average Pore Size

A sensitivity study on the effect of average pore size was conducted, keeping porosity fixed by shifting the baseline pore size by $\pm 5\mu m$. The filtration efficiencies of the new pore distributions are shown in **Figure 41**, with comparison to the baseline case.
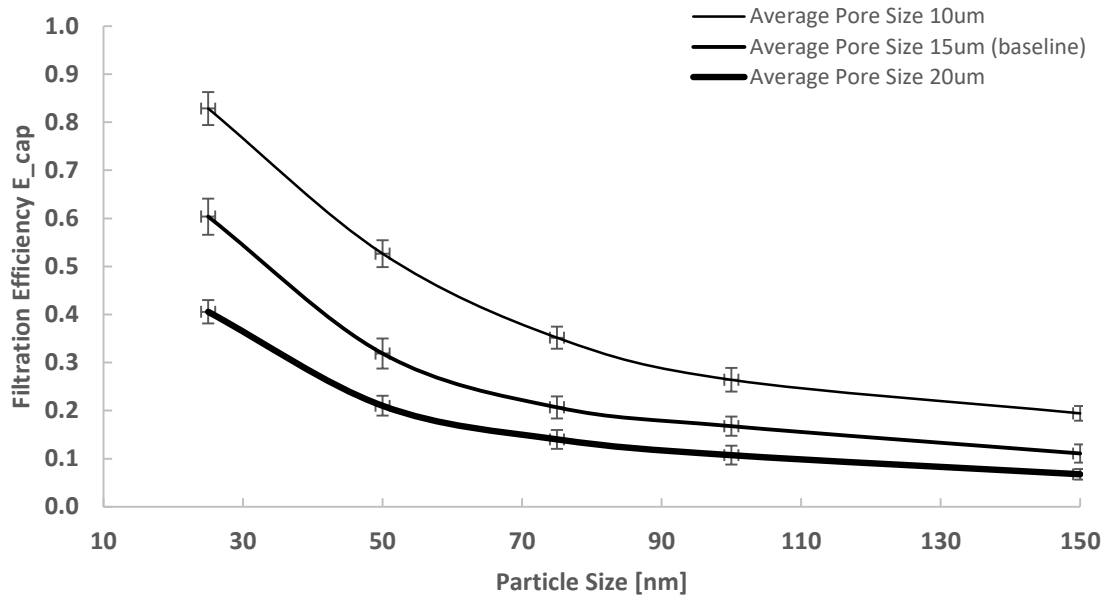
Figure 41. Size-dependent filtration efficiency with changing average pore size.

Additionally, **Figure 41** confirms that a decrease in average pore size can lead to an increase in filtration efficiency across all particle sizes. It follows that the smaller the average pore size, the smaller the "circular obstacle" is to maintain the same porosity. This means that for the same wall thickness, more obstacles are stacked up to create more cavities and pores for flow to travel through. To control for this, in this sensitivity study, regardless of the magnitude of the average pore size, all three cases share the same distribution and the probability density function for each distribution is identical. Since the wall with 10 μm average pore size has more pores in total, the quantity of relatively small pores is more than the baseline case, though they comply with the same distribution. Flow bypasses occur due to the small pores and create low flow regions, which are critical for particle filtration as shown in **Figure 42.** To better visualize the particle movements in wall, a streamline is highlighted for each case in Figure 43. Compared to the baseline,

the 10 μm streamline ⊛, goes through more divergences, and these can enhance the diffusion effects due to low flow velocity. By contrast, streamline ⊖ has fewer divergences than the baseline.

| Velocity |
| 0.35 |
| 0.33 |
| 0.31 |
| 0.28 |
| 0.26 |
| 0.24 |
| 0.22 |
| 0.20 |
| 0.17 |
| 0.15 |
| 0.13 |
| 0.11 |
| 0.09 |
| 0.07 |
| 0.04 |
| 0.02 |
| 0.00 |
| [m s^-1] |

(a)   (b)   (c)
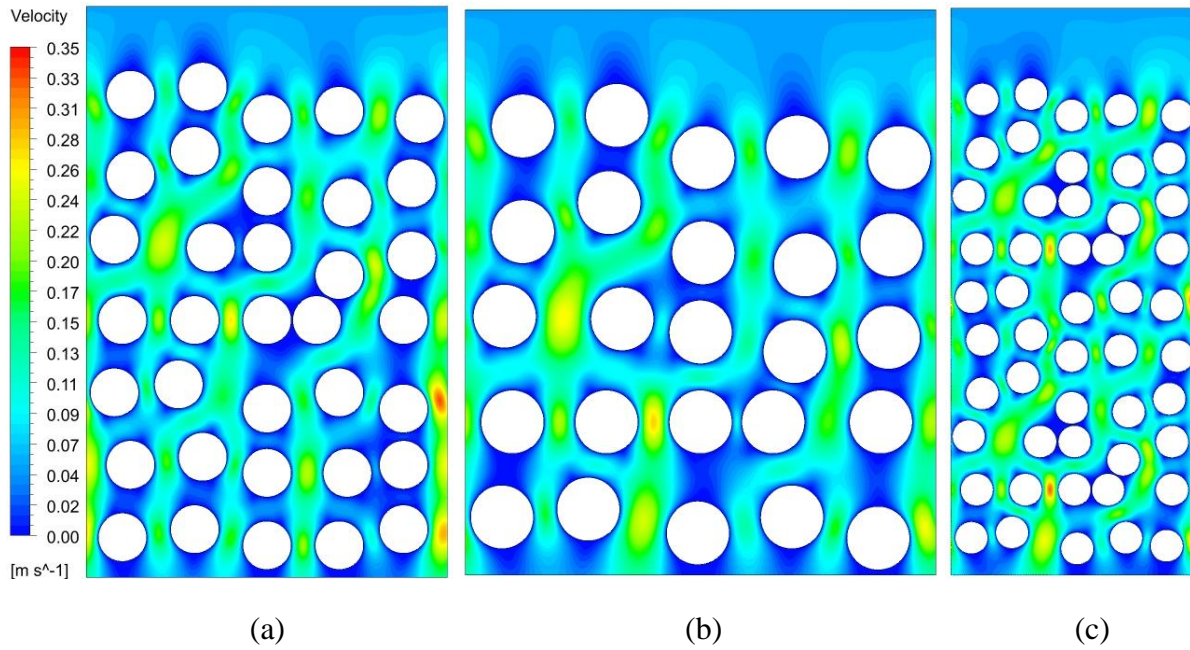
Figure 42. Velocity contour for (a) the baseline, (b) 20um average pore size and (c) 10um average pore size.

(a)	(b)	(c)
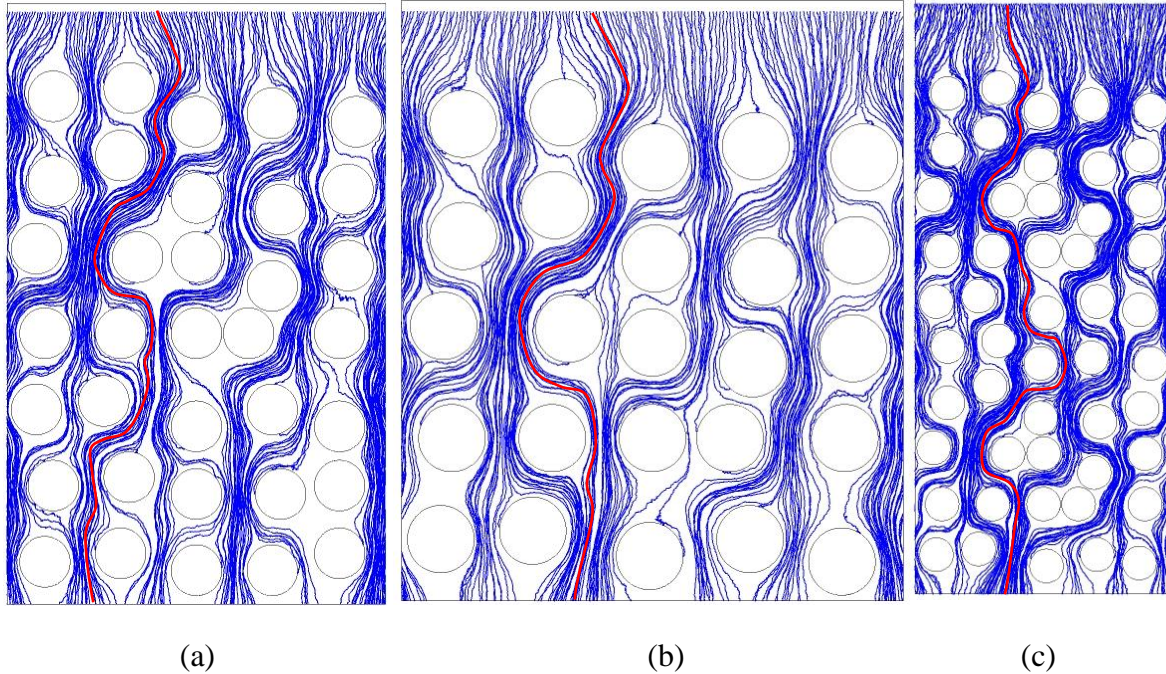
Figure 43. Particle tracking of (a) baseline, (b) 20um average pore size and (c) 10um average. A streamline is highlighted in red for each case.

Table 6 shows that pressure drop increases as average pore size deceases. Following streamline ⊛ in **Figure 43**, it can be seen that it travels a longer distance than any other cases, as a result of a larger quantity of small sized pores. Even more significant is that streamline ⊛ is in the middle of a much narrower canal. The Darcy-Weisbach equation indicates pressure drop is inversely proportional to second order of canal diameter, the narrower canal is, the higher the pressure drop across the wall. This is the dominate factor of the GPF wall pressure drop.

Table 6. Pressure drop comparison among samples with different average pore size.

	Pressure	0D	Difference
Baseline	39.5 Pa	36 Pa	9.7%
Average Pore Size 10um	83.5 Pa	82 Pa	1.8%
Average Pore Size 20um	21.7 Pa	20 Pa	8.5%

Based on the GPF sample in this study and simulation results, it can be seen that simply decreasing the average pore size in purpose of increasing filtration efficiency will dramatically raise the pressure drop of GPF and may jeopardize engine performance. However, the sensitivity study inspired the combination of multiple layers varying pore size to achieve higher filtration efficiency, while keep pressure drop low. Previous work has shown that filtration is done in the top 1/3 to half of the wall [25]. Therefore, a filter design having smaller average pore sizes in the top layers, and the remainder having larger average pore sizes as shown in **Figure 44**, should have a high capture efficiency, with low pressure drop. The proposed GPF design proposes a 2/5 and 3/5 spit of the wall substrate, where the top 2/5 possesses high initial capture efficiency and is rapidly loaded with soot or ash. This way, a cake-like membrane will quickly form and sustain a high filtration efficiency. Methods such as co-assembly of Polystyrene/clay colloidal crystal, could accurately configure microstructure of substrate fabrication with controlled porosity and pore size distribution [54].
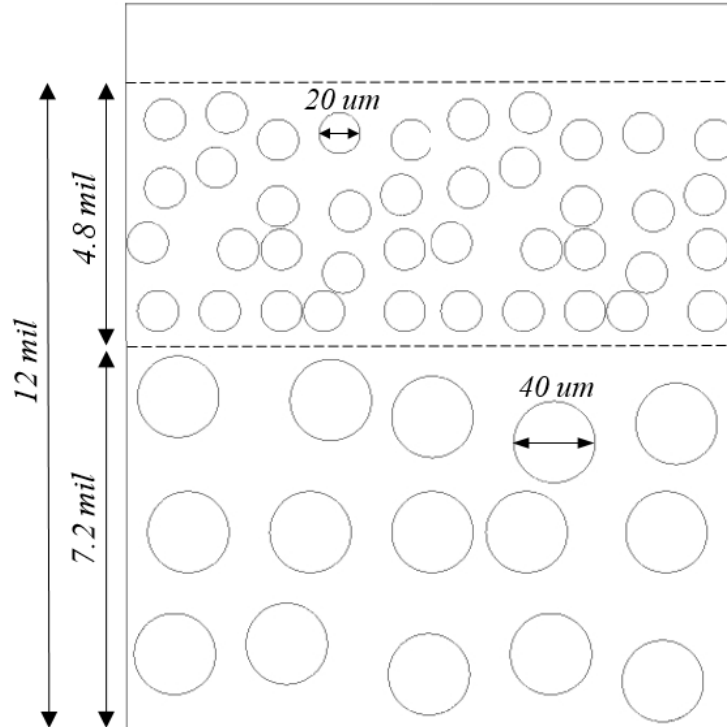
Figure 44. Proposed GPF wall with varying porosity. The top 2/5 of the wall is composed of 10um pores and the bottom 3/5 is composed of 20 um pores.

This new wall design is projected to deliver an average 8% increase of filtration efficiency, with only a 7 Pa higher pressure drop, as indicated in **Figure 45**. This level of pressure drop increase can easily be compensated for in the exhaust pipe or muffler.
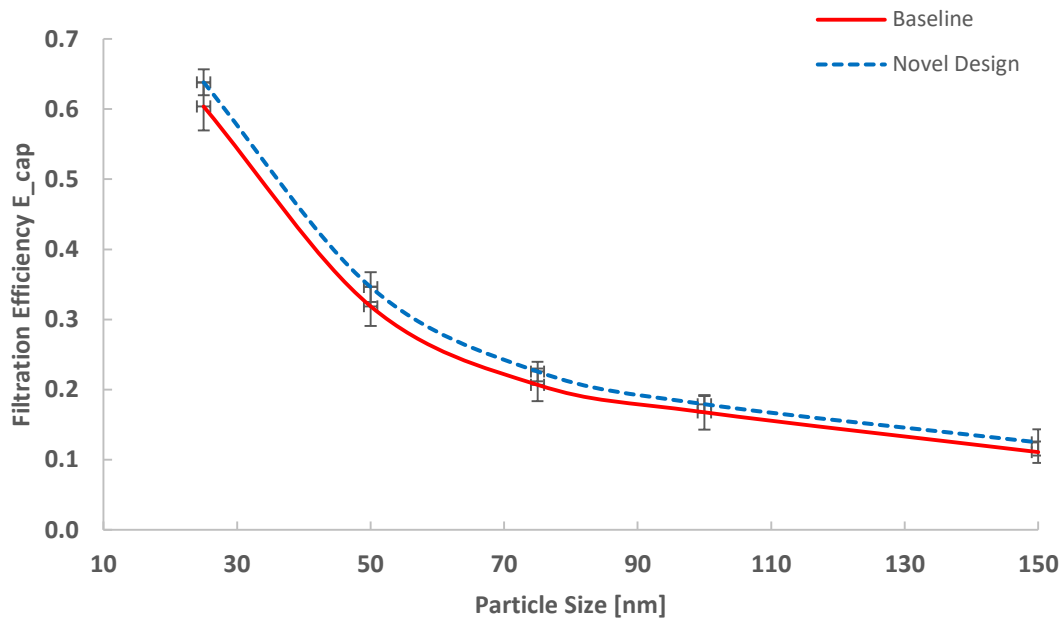
Figure 45. Novel GPF wall design shows increased filtration efficiency as compared to the baseline.

Conclusions

Simulation results show the average filtration efficiency of GPF first increases and then decreases as the pore size distribution tightens and has shown the existence of a pore size distribution range, between the baseline and tight pore distribution that can achieve the maximum filtration efficiency potential of the sample GPF. Pore size distributions fitting in this recommended range contains pores small enough ($a < 10\mu m$) to diverge the flow and large enough ($5\mu m < a$) to allow a fraction of flow pass, which is a good balance for particle filtration without large increases in pressure drop.

The sensitivity study indicates a decrease of GPF average pore size can lead to an increase of both filtration efficiency and pressure drop. A new GPF design is proposed with a 2/5 and 3/5 spit of the wall substrate with top 2/5 consist of small sized pores and the rest large sized pores.

69

The new wall substrate design projects to deliver an 8% increase of filtration efficiency across all particle sizes, at the expense of only a 7 Pa higher pressure drop.

CHAPTER IV

MANUSCRIPT #3

Overview

The wide application of Gasoline Direct Injection (GDI) engines and the increasingly stringent Particulate Matter (PM) and Particulate Number (PN) regulations make Gasoline Particulate Filters (GPFs) with high filtration efficiency and low pressure drop highly desirable. However, due to the specifics of GDI operation and GDI PM, design of these filters is even more challenging as compared to their diesel counterparts. Computational Fluid Dynamics (CFD) studies have been shown to be an effective way to investigate filter performance. In particular, our previous 2-D CFD study explicated the pore size and pore size distribution effects on GPF filtration efficiency and pressure drop. The "throat unit collector" model developed in this study, furthers this work in order to characterize the GPF wall microstructure more precisely. Throat unit collectors with different diameter ratios were created and simulated in ANSYS FLUENT to calculate the size-dependent particle filtration efficiency. The simulation results indicated a non-linear change of single collector efficiency, as the efficiency first decreased and then increased with a decreasing throat unit collector diameter ratio. The simulation results also showed the total wall filtration efficiency increased as the throat unit collector diameter ratio decreased. The throat unit collector model was also used to simulate the wall filtration efficiency change during particulates loading. The decrease of pore size in throat unit collector was used to mimic the pore bridging process during loading.

Introduction

Compared to (multi)Port Fuel Injection (PFI) engines, Gasoline Direct Injection (GDI) engines produce higher concentration of both Particulate Matter (PM, a mass-based measurement) and Particulate Number (PN, a number concentration based measurement) [2, 35, 47, 52]. This increase in emissions raises numerous issues for both human health and the environment [6, 55, 56]. A recent study shows more than 4 million people died worldwide due to the exposure to PM 2.5 and its related diseases, such as lung cancer and cardiovascular disease [57]. In response to the hazardous effects caused by GDI particulate emissions, regulatory agencies have proposed stringent regulations to control them. Europe and China pioneer this regulatory campaign with the strict EURO 6 and China 6 regulations limiting PN emissions to be below $6x10^{11}$ #/km. In contrast, the EPA and CARB of the US propose a mass-based particulate emission regulation, which is less strict than EURO 6 if the $2x10^{12}$ particles/mg correlation is applied. Based on the large amount of data in the literature, for gasoline engines, with no aftertreatment applied, a majority of those tested failed to meet the EURO 6 limit and only a small percentage met the CARB LEV III 2025 limit, as shown in **Figure 46**. These regulations make the design and development of Gasoline Particulate Filters (GPFs) with high filtration efficiency and low pressure drop challenging, but desirable [7, 8, 46, 58].
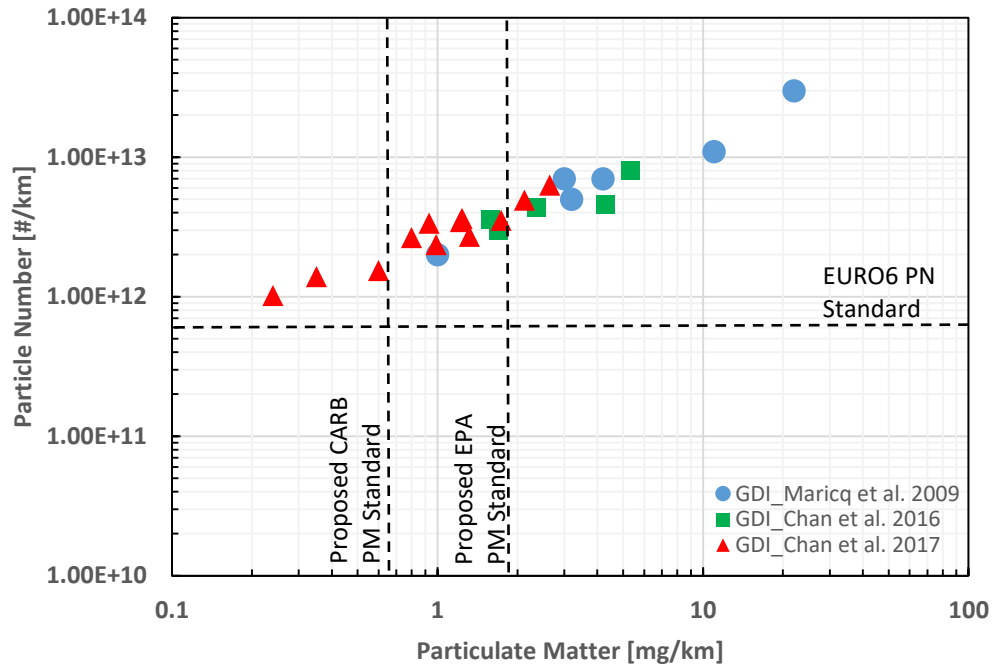
Figure 46. Current GDI engine out particulate emissions exceed EURO 6 and CARB LEV III limit based on data from[2, 59, 60].

Analytical models have been widely used for Diesel Particulate Filter (DPF) filtration simulations, and have been proven to be effective by numerous studies [18-20]. Based on packed bed theory and the unit collector model, the analytical model assumes the porous wall of DPF consists of mono-sized grains with the grain diameter as the single degree of freedom that can be altered [10, 13-15, 40]. This assumption makes the analytical solution possible and efficient on the soot-cake-dependent DPF filtration prediction. As opposed to DPFs, GPFs normally feature porous wall with higher porosity and lower average pore sizes, which dramatically complicates the microstructure of the GPF wall. The complicity of the GPF microstructure, including pore size variations, cavity size variation and their connectivity, are shown to have an strong impact on the GPF filtration and pressure drop performance [27, 61-63] . Also, unlike DPFs, GPFs heavily rely on deep bed filtration due to the continuous active regeneration conditions in the exhaust. To

73

account for the inhomogeneity of GPFs, Gong creates the Heterogeneous Multiscale Filtration (HMF) model to resolve the pore size variation and non-uniform porosity across the wall [21, 22, 64]. However, the HMF model is still an analytical method at its core by converting pore size distribution into a scaled range of unit collectors. The effect of the cavity scales and their connectivity in the cordierite-based GPF wall on filtration needs further investigation. More recently, researchers have begun to switch their attention from the simple analytical model to a 3D model created from a CT-scanned reconstruction, in order to better understand the flow field and filtration mechanism within the GPF wall [65-68]. Though it may be a highly accurate representation of the physical wall structure, this type of simulation, such as a Lattice Boltzmann model, is very computationally expensive, time-consuming and not generalizable. Only a small fraction (typically a 2 cm x 2 cm segment) of the porous substrate can be scanned and modeled each time and the demand for powerful computational resources is inequitably high. Therefore, in this study, the "throat unit collector" model is proposed with more degrees of freedom than the classic spherical unit collector model in order to represent the GPF wall microstructure more accurately. It is a more time and cost economical approach compared to the 3D reconstruction model. The throat unit collector model is created to focus on the pore size, cavity size and their connections in the GPF wall. This model was inspired by SEM images of a typical GPF, and was developed based on the GPF wall "circular obstacle" model [69]. Previous research has demonstrated the effectiveness of using CFD to predict the filtration efficiency in a complex GPF wall flow domain [69]. Thus, CFD methodology is applied in this study to resolve the size-dependent particle filtration efficiency of a single throat unit collector. The throat unit collector model enables us to alter the cavity and pore size and study the effects of collector diameter ratio

on GPF filtration. This model is an evaluation tool to explain the dependency of GPF wall filtration efficiency on particulates loading.

Approaches

GPF Sample Properties

GPF wall microstructure drives the development of this model. CFD is used to resolve the flow field in the wall in great detail, and offers the ability to track particles so as to study their dynamic interactions with the substrate. ANSYS FLUENT was the package used for this numerical simulation. Prior to the CFD simulation, a 2D axisymmetric geometry was established to accurately capture the characteristics of the sample GPF wall substrate as described in **Figure 47** and **Table 9**, including the porosity and the average pore size.

Figure 47. Image of the sample GPF.

Table 7. Sample GPF wall properties

Sample GPF Wall Properties	
Cell Density [CPSI]	300
Wall Thickness [mil]	12
Porosity ε	0.65
Mean Pore Size $\hat{d}_p$ [um]	15

Throat Unit Collector Model

Earlier research from our group shows a unique and effective way to model the complex wall microstructure. The model was created with an array of 'circular obstacles', in which the cavities are to represent the physical void space observable in SEM images, an example of which is shown in Figure 48 [7]. The horizontal and vertical gaps between the circular obstacles represent pores in GPF substrate. These pores link the void space together and serve as canals for gases and particles to pass through. Instead of focusing on air flowing over obstacles as the packed bed theory does, the gas travels through the cavities via different sizes of pores, as indicated in **Figure 49**.
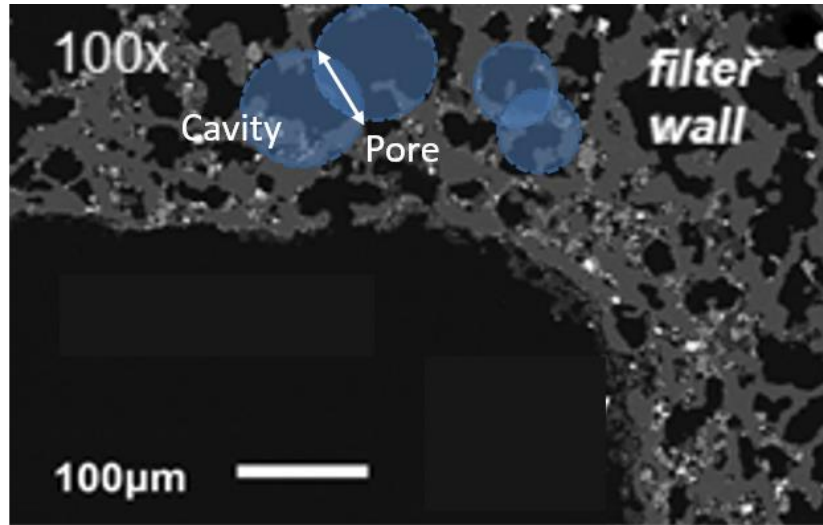
Figure 48. SEM image of a typical GPF wall, showing the cavities, pores and their connectivity.
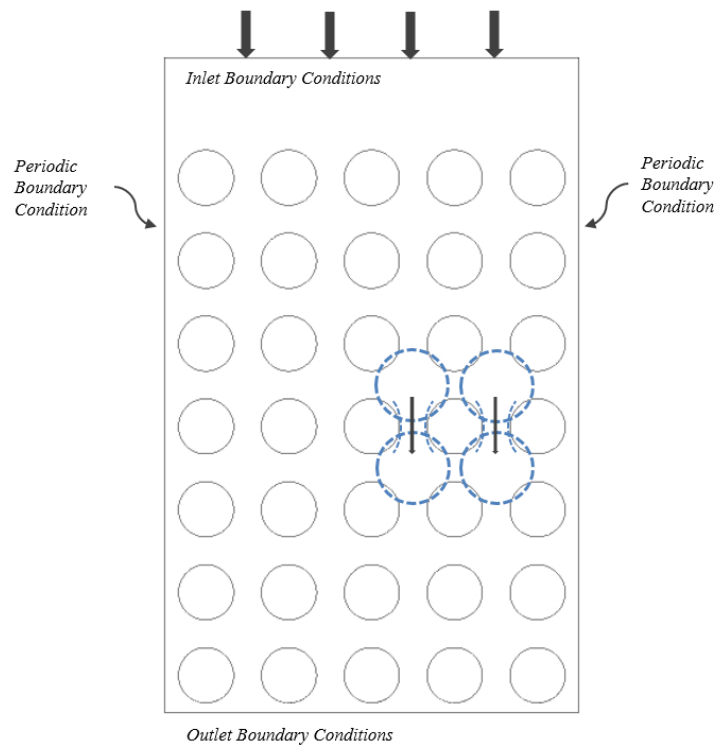
Figure 49. GPF wall model. The cavities that exhaust actually flows through are represented by blue dash line. Let d be the diameter of the obstacle; a is the pore size on horizontal; b is the pore size on vertical; Let D be the diameter of the cavity.

The SEM image of the GPF substrate wall truly provides a unique perspective from which to understand the interactions and connections of pores of different sizes. It prompts us to rethink porous wall modeling and strive to make improvements to comply with the characteristics of the substrate wall more precisely.

Based on the wall model above, it would be a natural and intuitive course of action to replace the "circular obstacles" with a sequence of new unit collectors. Hereby, we call them "throat unit collectors" (Figure 50). The introduction of the throat unit collector is to reflect the wall attributes and better represent the cavity and pore connections. The new model also enables the study of the effects of cavity size change on filtration performance. Thus, a critical parameter of the throat unit collector model is defined as the ratio of cavity diameter to pore size $\frac{D}{d_p}$, which governs the filtration efficiency of the individual unit collector by a large extent. Figure 50 shows a 2D representation of the throat unit collector where the solid ceramic material encloses the void space, which is responsible for capturing the particulates from the flow. Once the model was imported into FLUENT, only the void space was extracted to generate the flow domain and the 2D model was converted to a 2D axisymmetric model to simulate the 3D flow and particle filtration. The parameter b' in Figure 50 is the height of the throat unit collector and a' is the side length of the cuboid. The size of a' and b' are closely related to the size of D, d_p and porosity ε, from equation (23-24).
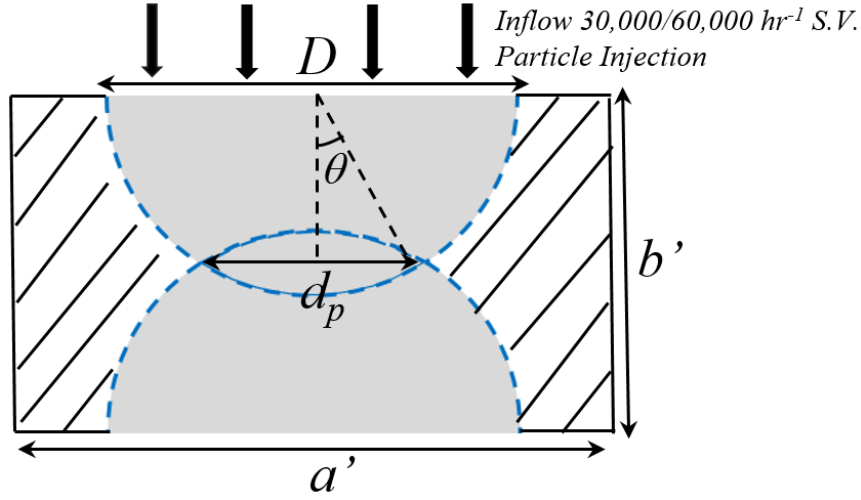
Figure 50. Throat unit collector. D is the diameter of cavity; d_p is pore size; let a' be the side length of the cuboid throat unit collector and b' be the height; angle θ changes with the diameter ratio.

$$a' = \sqrt{\frac{\pi D^3 + \pi d_p{}^2 \sqrt{D^2 - (\frac{d_p}{2})^2} - 2\arcsin(\frac{d_p}{2D})D^3}{12\varepsilon\sqrt{D^2 - (\frac{d_p}{2})^2}}} \qquad (23)$$

$$b' = \sqrt{D^2 - d_p{}^2} \qquad (24)$$

CFD-based particle tracking is carried out to calculate the single unit collector efficiency η. Equation (25) is derived to process the particle tracking results, where $N_{injected}$ is the total number of particles injected into the unit collector, and $N_{trapped}$ indicates the number of particles trapped on the collector wall. Special treatment is required for particle count $N_{injected}$ and $N_{trapped}$ since the flow field in the collector is resolved in axisymmetric fashion. Given the fact that particles are injected into a 2D flow domain, proper integration along the cavity radius is needed to deliver a filtration efficiency η for the 3D unit collector. For GDI-sized particulates, only capture by

Brownian diffusion and inertial effects are considered in particle tracking. The Brownian and Stokes-Cunningham corrected drag forces are applied on particles.

$$\eta = \frac{N_{trapped}}{N_{injected}} \tag{25}$$

To predict the overall filtration efficiency across the GPF wall, an aggregate of throat unit collectors need to be created (Figure 51). Equations that relate single collector efficiency to total efficiency were derived, as shown in equations (26) and (27). The parameter E is the total filtration efficiency across the wall; η is the single unit collector efficiency; C is a constant, which only depends on the wall porosity ε, thickness t, cavity diameter D and angle θ.
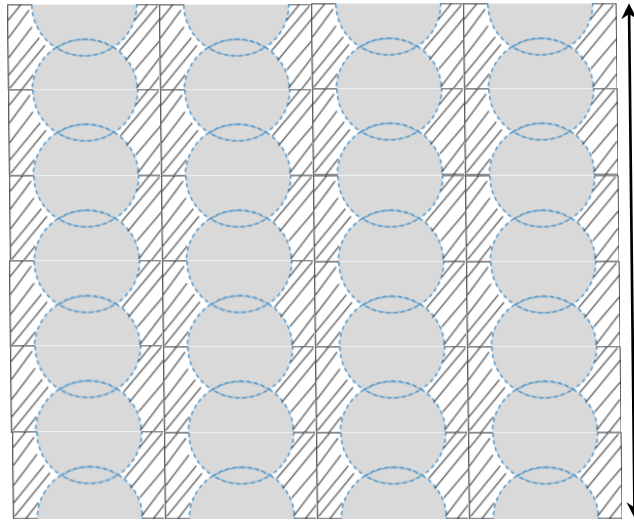
Figure 51. An aggregation of throat unit collectors form the GPF wall.

$$E = 1 - e^{-C\eta} \tag{26}$$

$$C = \frac{\frac{3}{2}t\varepsilon}{D + 4D\sin^2\theta\cos\theta - \frac{2\theta}{\pi}D} \tag{27}$$

The Baseline Throat Unit Collector and Variation with Diameter Ratios

To simulate the porous wall for a specific GPF sample, a baseline throat unit collector was created to match the sample GPF properties (Table 7). The pore size, d_p, of the collector is fixed at $15 \mu m$, which is the mean pore size of the sample GPF. The diameter ratio of the baseline collector is determined by fixing the collector height b' equal to the spherical grain diameter d_c from packed bed theory (Equation 28). Based on equation (24), the diameter ratio of the baseline throat unit collector can also be determined using equation (29). The baseline throat unit collector is shown in **Figure 52**.

$$b' = d_c = \frac{3}{2} \frac{1-\varepsilon}{\varepsilon} d_p \tag{28}$$

$$\frac{D}{d_p} = \frac{\sqrt{b'^2 + d_p^2}}{d_p} = \frac{19.2 \mu m}{15 \mu m} \approx \frac{1.3}{1} \tag{29}$$
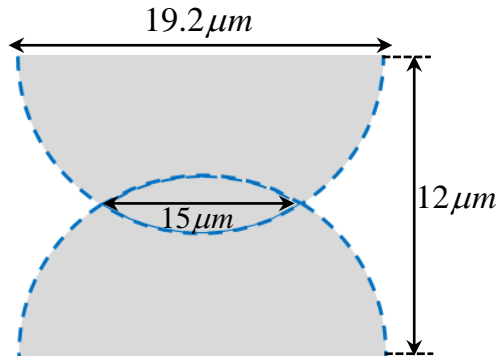
Figure 52. Schematic of the baseline throat unit collector matching the properties of the sample GPF.

In addition to the baseline case, four other throat unit collector geometries with different diameter ratios were created to study the diameter ratio effects on the filtration efficiency of both

a single throat unit collector and the collector aggregate representing the GPF wall. The diameter ratio changes in each case with the changing cavity diameter, *D,* keeping the pore size fixed at $15 \mu m$ as shown in **Figure 53**. Each case is run at both 30,000 hr^{-1} and 60,000 hr^{-1} space velocity. CFD-based particle tracking is conducted for each throat unit collector geometry to calculate the size-dependent single collector filtration efficiency. The total efficiency across the wall that is composed of a combination of throat unit collectors were further calculated using equations (26) and (27). Comparisons were made across the simulation results, to shed light on the transient influence of particulates loading on GPF performance.

| (a) | (b) | (c) | (d) |
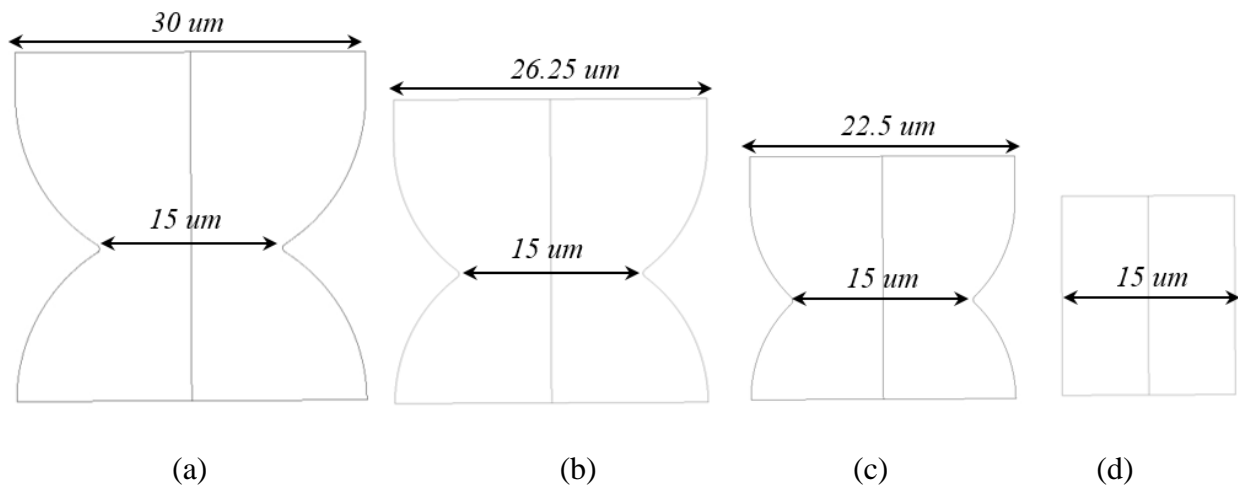
Figure 53. Throat unit collectors with four different diameter ratio. Diameter ratio (a) 2:1, (b) 1.75:1, (c) 1.5:1, (d) 1:1.

To decrease the effect of randomness introduced by Brownian diffusion of the particles during particle tracking, ten replicates for each diameter ratio, for specific injected particle sizes at each flow space velocity were executed to generate efficiency data. The efficiency then was calculated by averaging the ten data sets.

The throat unit collector model was validated with experimental data, from a Dinex sample GPF. The GPF sample was evaluated at room temperature and 30000 hr^{-1} space velocity. The size-dependent filtration efficiency of incident ammonium sulfate particles was measured using a TSI Scanning Mobility Particle Sizer (SMPS). The experiments were run for four hours with a constant flowrate and constant particle concentration. Filtration efficiency data was acquired for every half hour, as described in [70].

Results and Discussion

Throat Unit Collector Model Validation

The baseline model was validated with experimental data at 30,000 hr-1 space velocity. The throat unit collector with diameter ratio $\frac{D}{d_p} = 1.3$ yields a total filtration efficiency close to the sample GPF efficiency measured by experiment, with 4% difference (**Figure 54**). This validation showcases the capability of the throat unit collector model in terms of predicting the filtration efficiency of GPFs while sustaining high resemblance to the physical properties of the target GPFs. This resemblance of the throat unit collector to the physical wall properties can be beneficial when it comes to provide guidance to GPF modifications from the modeling point of view.
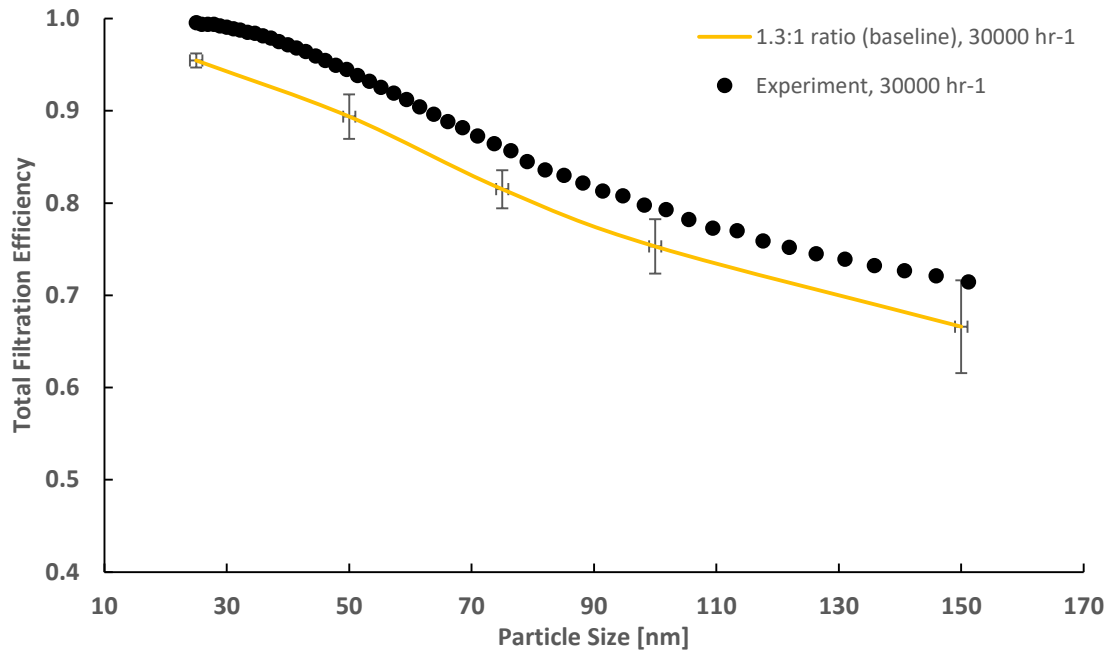
Figure 54. Total wall filtration efficiency with the baseline diameter ratio throat unit collector, validated by experiment data at 30,000 hr^{-1}.

Effects of Diameter Ratio and Space Velocity on Throat Unit Collector Filtration Efficiency

The single throat unit collector efficiency was evaluated for each diameter ratio at 20°C and 30,000 hr^{-1} space velocity. 75 nm particles were injected to the domain. The simulation results show a nonlinear change of efficiency as the diameter ratio decreases (**Figure 55**). The single collector efficiency first decreases and then increases when diameter ratio decreases. The minimum efficiency is seen at a diameter ratio of 1.5. Even though for GDI sized particles, Brownian diffusion dominates the motion of particles for most cases, inertial effects still play an important role in filtration for throat unit collectors with a large diameter ratio, namely $\frac{D}{d_p} = 2$. The sudden contraction of throat in the collector makes it hard for particles to follow the streamline, and as a result, particles are susceptible to be captured due to inertia. As the diameter ratio drops

to $\dfrac{D}{d_p} = 1.5$, the inertial effects diminishes, causing the single collector efficiency to decrease. However, as diameter ratio decreases further, Brownian diffusion dictates the collector filtration behavior. The average flow velocity in domain decreases with the decline of diameter ratio, which leads to a stronger Brownian diffusion, and in turn, a higher single collector efficiency.
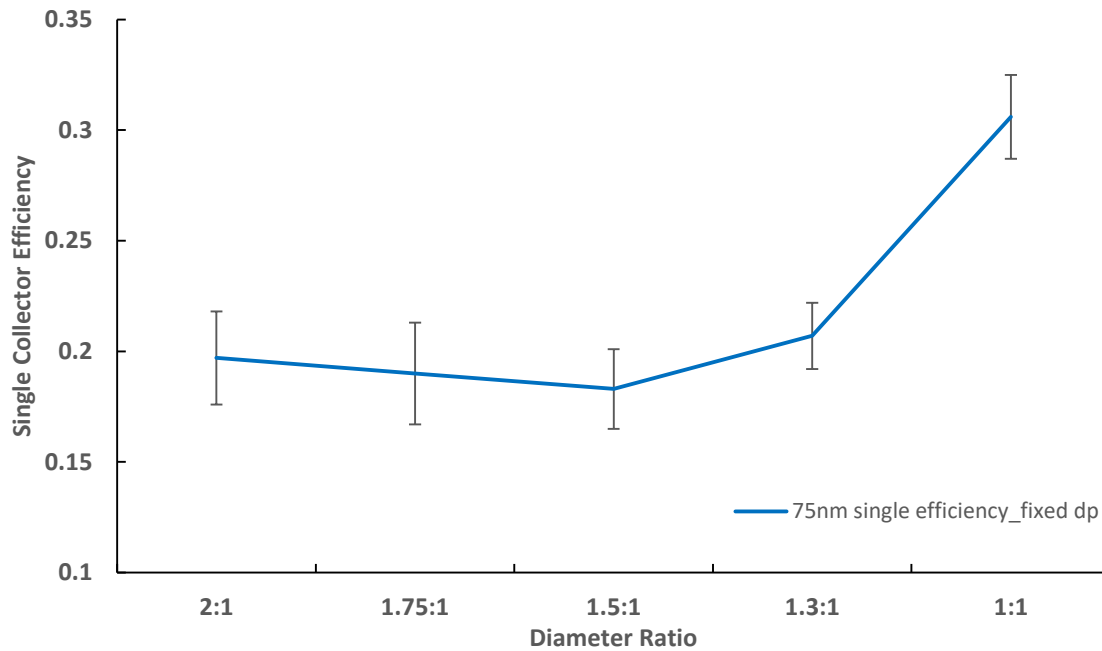
Figure 55. Single collector efficiency changes as diameter ratio decreases. Minimum efficiency is seen at diameter ratio of 1.5.

The total GPF wall filtration efficiency can be evaluated by stacking up single throat unit collectors, of a singular diameter ratio. By increasing or decreasing the diameter ratio, while fixing the porosity and pore size, numerous wall microstructure variations can be simulated allowing for study of the cavity size effects on the total wall filtration efficiency. By comparing the simulation results from walls with different diameter ratio throat unit collectors at the same space velocity, we find that a decrease of diameter ratio leads to an increase of total filtration efficiency, regardless

of the nonlinear trend shown by the single collector efficiency (**Figure 56**). The explanation for

this contradiction is that despite the single efficiency drop of the $\frac{D}{d_p}=1.5$ collector as compared to

the $\frac{D}{d_p}=2$ case, the total efficiency of the $\frac{D}{d_p}=1.5$ collector aggregation is offset by a larger quantity

of collectors. This compensation is represented by the constant C in equation (27). Based on this

rationale, a new wall design was suggested to achieve higher filtration efficiency than the sample

GPF. This higher efficiency would come from the 1:1 diameter ratio unit collector, creating a wall

that is solely composed of these type of unit collectors could increase the overall filtration

efficiency by as much as 25% according to **Figure 56**. This new wall design demonstrates itself to

be less susceptible to inflow velocity fluctuations, as an increase of space velocity has less impact

on the filtration efficiency of small diameter ratio unit collector than large ones, as shown in **Figure**

56. The new design could be more efficient during vehicle acceleration and other scenarios where

intake air increases, while sustaining high performance. More research, and particularly

experimentation is needed to further verify these model assertions.
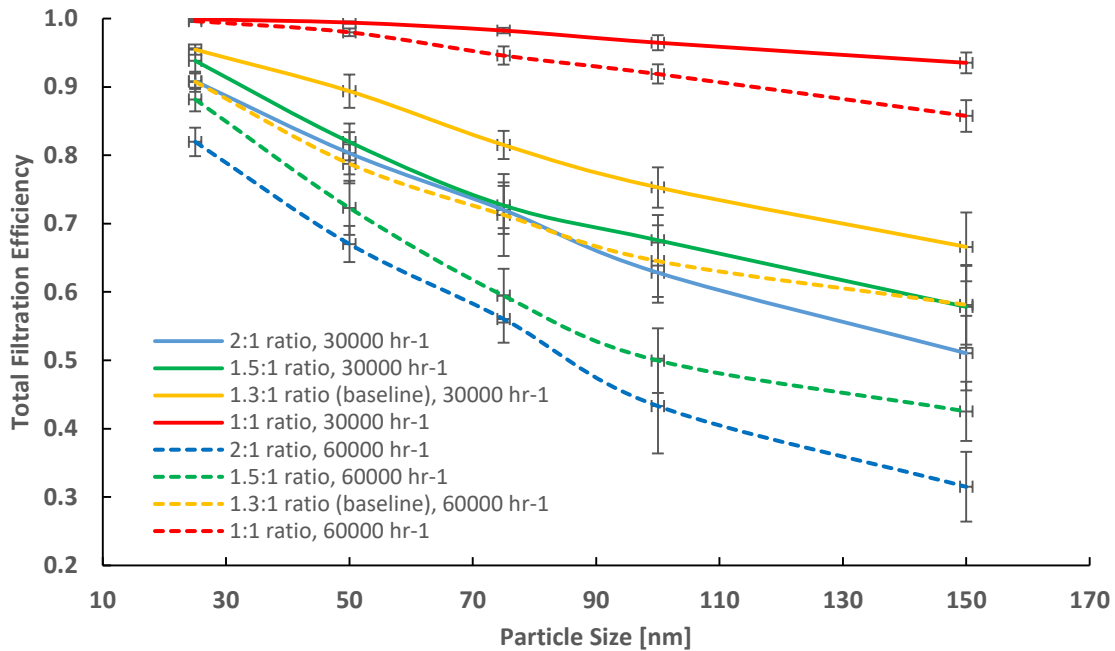
Figure 56. Total filtration efficiency of throat unit collectors with different diameter ratios, at both 30000 hr^{-1} and 60000 hr^{-1}.

Throat unit collector aggregates with four different diameter ratios were simulated at 20°C, and at both 30,000 hr^{-1} and 60,000 hr^{-1} space velocities. From this comparison, we can observe that total efficiency decreases with an increase in space velocity. For a single throat unit collector at constant temperature, the efficiency decreases as the inflow velocity increases because Brownian diffusion is the dominant factor governing the filtration behavior. The faster that particles move, the weaker the effect of Brownian diffusion becomes, regardless of particle size. Therefore, the total filtration efficiency also decreases as space velocity increases.

Transient GPF Filtration Simulation Using the Throat Unit Collector Model

The throat unit collector model was also used to simulate the GPF sample filtration efficiency during particle loading. A schematic is shown in **Figure 57** to illustrate how the diameter ratio changes during loading. First, we assume the cavity diameter *D* remains constant and that all

particles deposit on the upstream portion of the cavity wall and the throat. This deposition characteristic can be verified in **Table 8**, which shows the CFD-predicted proportion of particles trapped upstream of the collector compared to that of the downstream side.
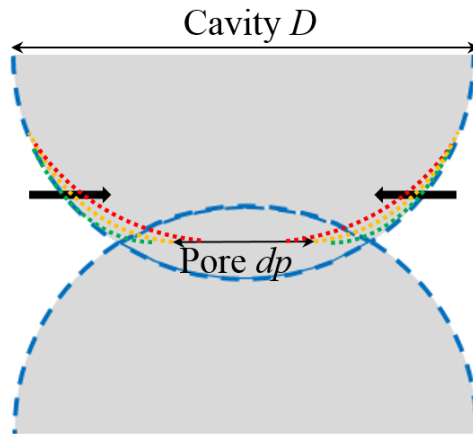
Figure 57. Throat unit collector schematic showing the diameter ratio change during loading.

Table 8. CFD predicted particle deposition characteristics of the throat unit collector with different diameter ratios

	$20°C, 30,000\,hr^{-1}$ S.V., 75nm Particles	
D/d_p	Upstream and throat deposition	Downstream deposition
1.3:1	95%	5%
1.5:1	83%	17%
2:1	85%	15%

Inflow particles gradually accumulate on the upstream cavity wall, causing bridging in the throat. A "new" throat unit collector is then formed with a larger diameter ratio, which according to **Figure 58**, yields a nonlinear change to the single collector efficiency η. Compared to the

single collector efficiency change with fixed pore size, the single collector efficiency change with fixed cavity diameter possess a similar trend, though it produces a slightly higher efficiency value. This higher efficiency is attributed to the fact that the collector height b' of the throat unit collector stays fixed during bridging, which does not provide enough distance for injected particles to curve around the throat before hitting the bridging region due to inertia. The smaller the pore size becomes, the more particles that will be captured by the throat if b' stays independent of the pore size change. Additionally, a fraction of the inflow still travels through the particle accumulation area, where the bridging takes place. Due to its much higher density and lower permeability, the newly formed pore bridge yields a nearly perfect filtration efficiency. Combining these two factors, the total single unit collector efficiency η' will increase as particulates load as shown in **Figure 59**. As a result, the total efficiency of the wall will also increase.
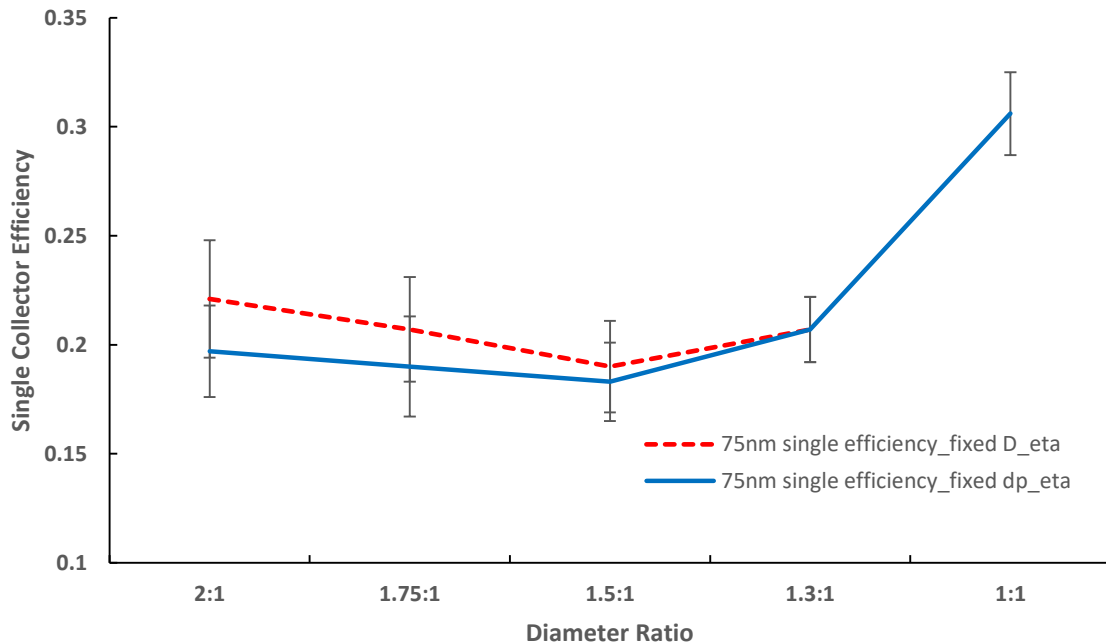
Figure 58. Single collector efficiency dependency on diameter ratio. Diameter ratio changes either by altering the cavity diameter or pore size.
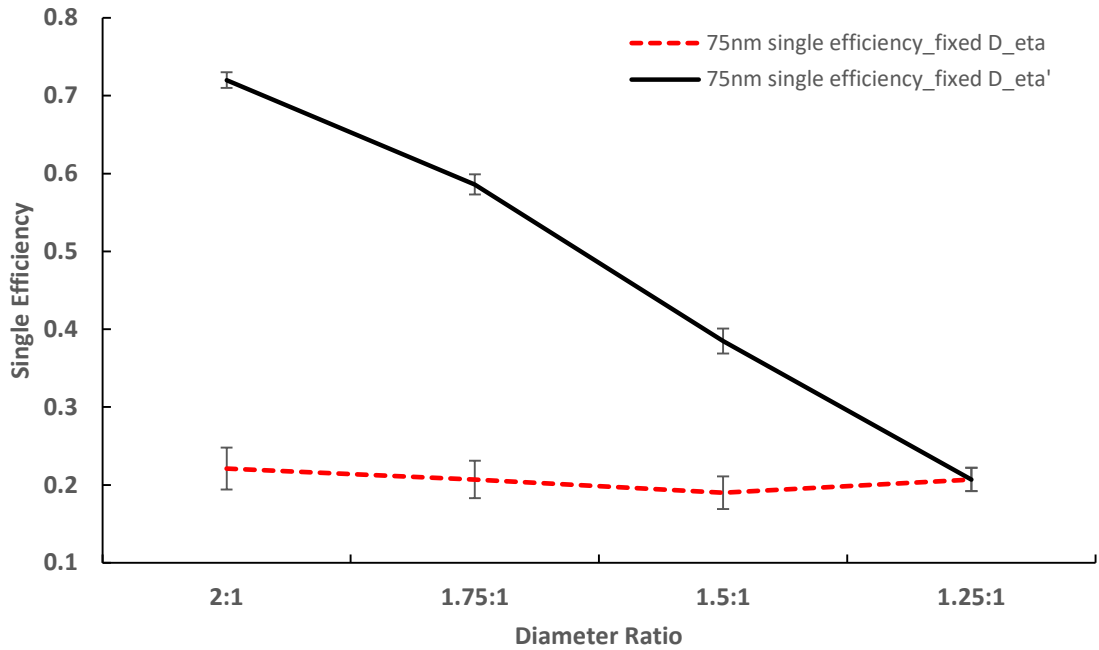
Figure 59. Single collector efficiency η and η' changes with diameter ratio.

To validate the transient behavior of the throat unit collector model, a time dependent change in the collector pore size due to bridging was derived, with the thickness of the pore bridging defined as $0.5\mu m$. In addition, it was assumed that particles only load the top 1/3 of the wall, with a linear loading profile for the first row of throat unit collectors having the maximum loading, as shown in **Figure 60**. The particle loading profile in **Figure 60** was normalized by dividing the particle packing density of the subsequence collector rows by the packing density of the first row.
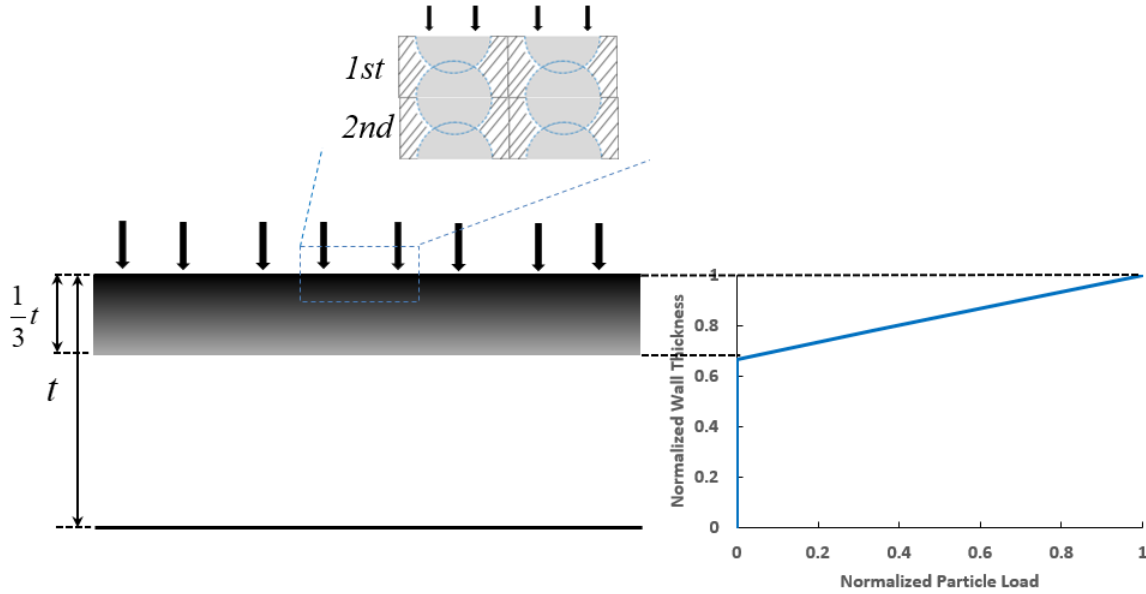
Figure 60. Normalized particle loading profile in the sample GPF wall is assumed to be linear with maximum loading in the first row throat unit collectors. The top rows of throat unit collectors in the zoom view have the same layout as in Figure 51.

At 20°C and 30,000 hr^{-1} space velocity, the total GPF sample filtration efficiency for 75 nm particles in transient was predicted. The simulation results match the experimental data well, as shown in **Figure 61**. At the initial state, when the sample GPF is clean, it has a pore size of $15\mu m$ with $\frac{D}{d_p} = 1.3$ diameter ratio for the top row collectors. After 4 hours of loading, the particles have bridged in the throats of the top row collectors and block the pore, causing a dramatic increase in the collector diameter ratio. **Figure 61** also shows the transient changes of the single collector efficiency η and η'. The single collector efficiency η is strongly dependent on the diameter ratio of the collector, and as a result, η alters dynamically during the bridging process. **Figure 61** shows that η has a similar nonlinear trend as in **Figure 59**, because the pore bridging phenomenon is a close equivalence to the increase of the unit collector diameter ratio. Extrapolation was taken based on the η plot from **Figure 59** when predicting the filtration behavior of the throat unit

91

collector if the diameter ratio exceeds 2:1 due to loading. Given the time dependence of the single collector efficiency, the total wall filtration efficiency can be predicted by using only equation (26-27). The model results are shown to match the experimental data well.
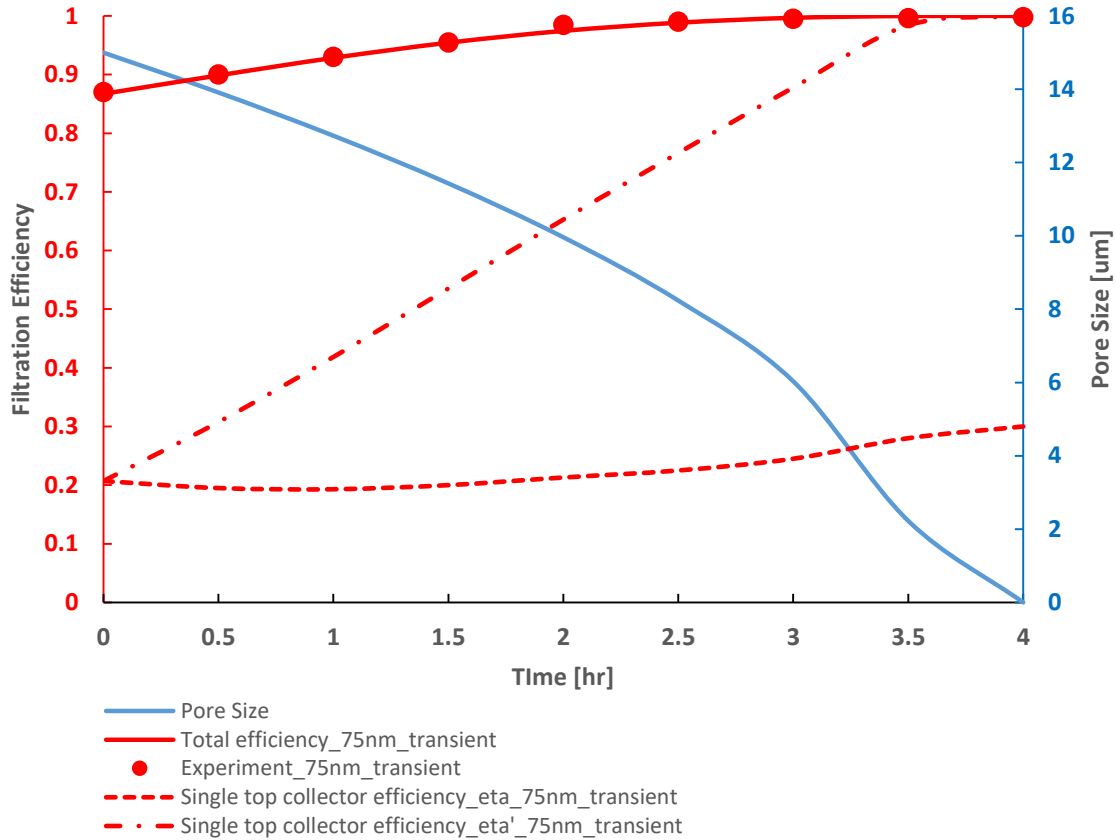
Figure 61. Model results for transient single collector efficiency, total wall efficiency and experimental results for GPF sample filtration efficiency for 75 nm particles.

Conclusions

Validation of the model with experimental data demonstrated the high fidelity of the throat unit collector model. Parameterization of the cavity diameter allowed for changing the cavity size in order to study its effects on GPF wall filtration efficiency. The diameter ratio of the throat unit

collector was shown to be a crucial parameter for calculating the single collector efficiency, whereas the overall GPF efficiency was shown to depend more on the quantity of the collectors in the wall. The throat unit collector model was also able to predict the transient filtration efficiency of the experimental GPF sample with particle loading.

The throat unit collector model has great potential for predicting the loading profile for particulates or ash across the wall, by treating the wall discretely as a 1-D problem. Additionally, using this model can offer insight into the pore bridging process, and how pore bridging impacts the overall GPF efficiency with time.

This model could also be used to predict the partitioning between the deep bed filtration and (soot) cake filtration in DPFs. This transition occurs when the throat unit collectors on top of the DPF wall fully bridge over, stopping the particle penetration and inducing the soot cake formation.

Finally, the throat unit collector model could also be used to investigate the effects of catalytic coatings on DPF/GPF filtration performance, which is planned for a future publication.

CHAPTER V

MANUSCRIPT #4

Overview

Continuously tightening Particulate Matter (PM) and Particulate Number (PN) regulations make Gasoline Particulate Filters (GPFs) with high filtration efficiency and low pressure drop highly desirable as Gasoline Direct Injection (GDI) engines increase in market share. Due to packaging constraints, GPFs are often coated with three-way catalyst (TWC) materials to achieve four-way functionality. Therefore, it is critical to investigate the effects of various washcoating strategies on GPF performance. A 3D CFD model, with an analytical filtration model was created. A User Defined Function (UDF) was implemented to define the heterogeneous properties of the GPF wall due to washcoating or ash membrane application. The model demonstrated ability to predict transient filtration efficiency and pressure drop of uncoated and washcoated GPFs. Simulation results showed the evenly coated GPF yielded the best performance compared to other washcoating profiles. The model predicted results indicated that a GPF with a 2.6 g/L ash loading was able to achieve a balance between high initial filtration efficiency and low pressure drop.

Introduction

The wide application of GDI engines calls for the rapid adoption of Gasoline Particulate Filters (GPFs) to meet the ever tightening Particle Mass (PM) and Particle Number (PN) regulations [47, 52]. Due to the vehicle space constraints, manufacturers prefer to combine the conventional automotive Three Way Catalyst (TWC) and GPF together by washcoating with TWC materials to achieve a four-way functionality. Despite the packaging benefits of washcoated GPFs, concerns arise with respect to how the associated backpressure of the device affects the fuel efficiency, power output and emission performance of Gasoline Direct Injection (GDI) engines [71, 72]. Previous research has shown the potential of the washcoated GPFs to effectively reduce CO and NOx without compromising fuel economy [73-75], but depending on the washcoating strategy, multiple washcoat profiles can be developed within the substrate. Therefore, more research is needed to investigate the effects of various washcoat profiles on performance.

Ash and its effects on GPF performance is another topic of great interest [76-80]. As compared to diesel engines, GDI engines produce particulates in lower concentration and smaller size [2, 47, 52]. The high temperature of GDI exhaust continuously regenerates particulate in the GPF. The combination of lower particulate concentrations and the rate of regeneration makes it very unlikely that a cake will ever form on the filter wall. Thus, during the initial stage of use, GPFs rely primarily on the deep bed filtration to trap particulates [22, 58]. In addition, ash, derived from both incombustible lubrication oil additives and engine debris, gradually accumulate in and on top of the wall [81, 82]. The build-up of an ash membrane would take over the majority of the filtration duty and have a soot cake like functionality. Research from Ford showed that ash loading in a GPF could dramatically increase its filtration efficiency with negligible increase in pressure

drop [7, 76]. Therefore, one initiative of this study is investigating the influence of pre-loaded artificial ash membrane on the filtration performance and pressure drop.

In this paper, a numerical method was used to study the substrate heterogeneity effects on its performance. The substrate properties are varied either axially or vertically as a result of different washcoating profiles or ash membrane addition. 3D CFD along with the analytical filtration model was used for this analysis. The channel flow field and overall pressure drop were predicted via 3D CFD method (ANSYS FLUENT). Particle tracking was conducted to resolve the particle deposition profile. A C language based User Defined Function (UDF) was applied to define the initial wall properties, update wall properties for each time step and resolve the size-dependent filtration efficiency. This approach demonstrates advantage over experimentation in its ability of tracking the dynamic change in wall properties and particulate distribution during loading. Compared to 1D or 2D CFD modeling widely used in DPF models [10, 22, 40, 64, 83-85], 3D CFD offers an extra, lateral dimension to track particles more accurately [86, 87]. Hence, the filtration efficiency of small particles and their deposition locations can be predicted more precisely instead of assuming they would strictly follow the streamline.

Approaches

GPF Samples and Nomenclature

Experimental data from three different GPF samples were used in this study for model validation. The properties of these samples and their designations are presented in **Table 9**. Experiments were conducted in the Combustion and Reaction Characterization Laboratory (CRCL) to measure the transient, size-dependent filiation efficiency at 30,000 hr^{-1} space velocity [70]. The incoming particle concentration was fixed at 0.4 mg/m^3. The experimental setup is shown in **Figure 62**. Before each experiment, the sample was properly cleaned to remove residual particles.

Blank1 and Washcoat1 are samples used by Ford in their published research [80]. The particle-loaded filtration and pressure drop literature data were used for validation purpose in this study. Sample Blank2 was provided to the CRCL from Dinex. Both Blank1 and Washcoat1 samples were exposed to particle-laden flow at 23,000 hr^{-1}, with particle concentration of 15 mg/m^3. Three other washcoat variations were developed with an intent to mimic GPFs with different washcoating profiles. Washcoat2 properties are intended to mimic two-way coating with an overlap section in the middle of the substrate. Washcoat3 and Washcoat4 are meant to simulate one way coating with opposite orientations. All washcoat variations have the same total washcoat loading of 1.5 g/in^3.

Additionally, three models were created with various artificial ash membrane thicknesses to investigate the effects of ash membrane addition on performance, assuming the membrane is evenly distributed on top of the inlet channel wall. These models are designated as Ash1, Ash2 and Ash3, representing ash membrane thicknesses of 0.5um, 1um and 1.5um respectively. If measured by ash load per unit volume, these three models are loaded with 0.85 g/L, 1.7 g/L and 2.6 g/L of ash, assuming the density of ash is 1600 kg/m^3.

Table 9. Sample GPF properties and nomenclature

	Blank1	Washcoat1	Blank2
Dimension D×L	1" ×4"	1" ×4"	1" ×3"
Cell Density [CPSI]	300	300	300
Wall Thickness [mil]	12	12	12
Porosity ε	0.5	0.39	0.65
Mean Pore Size $\hat{d}_p$ [um]	22	17	15
Washcoat Load [g/in³]	0	1.5	0
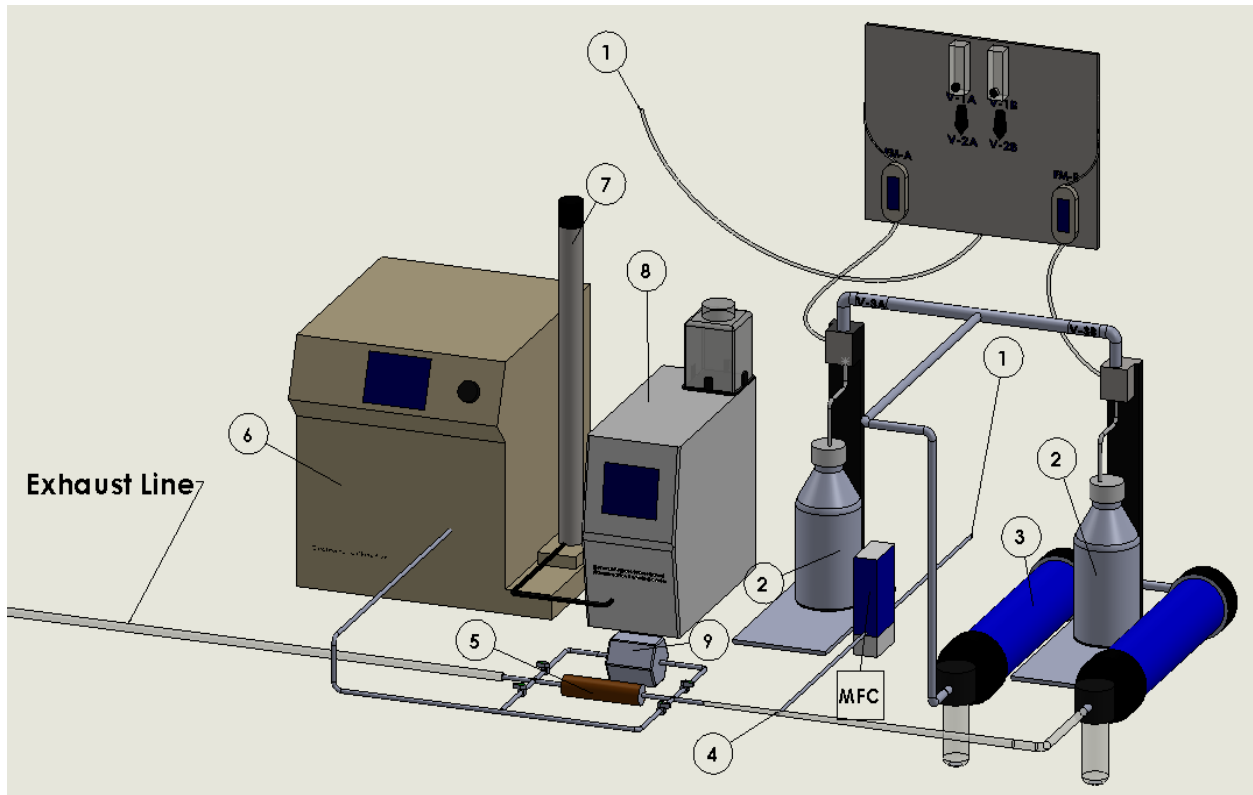
Figure 62. Experiment setup for GPF filtration measurement. (1)HEPA filtered building air is introduced into the system, (2)Atomizers, (3)Gas Dryers, (4)Mass Flow Controller for makeup air, (5)Filter chamber, (6-8)Scanning Mobility Particle Sizer, (9)Differential Pressure Transducer [70].

3D GPF Model

A 3D model was created to comply with the dimensions and the cell density of Blank1. Taking advantage of the highly symmetric geometry of Blank1, two quarter channels for inlet and two quarter channels for outlet were selected for modeling. A cross-shaped porous substrate separates these channels, as shown in **Figure 63.** Inlet and outlet zones were defined to account for the pressure drop due to flow contraction and expansion effects. The porous wall was evenly discretized into eight zones axially using the UDF. A mesh was generated prior to the CFD simulation with approximately 6 M cells. The mesh in specific regions, such as the inlet channel

entrance and channel-wall interface, was further refined to adapt to the sharp flow field change. A mesh size dependence study was carried out to reach a stable overall pressure drop across the model and a stable wall velocity profile along the channel.
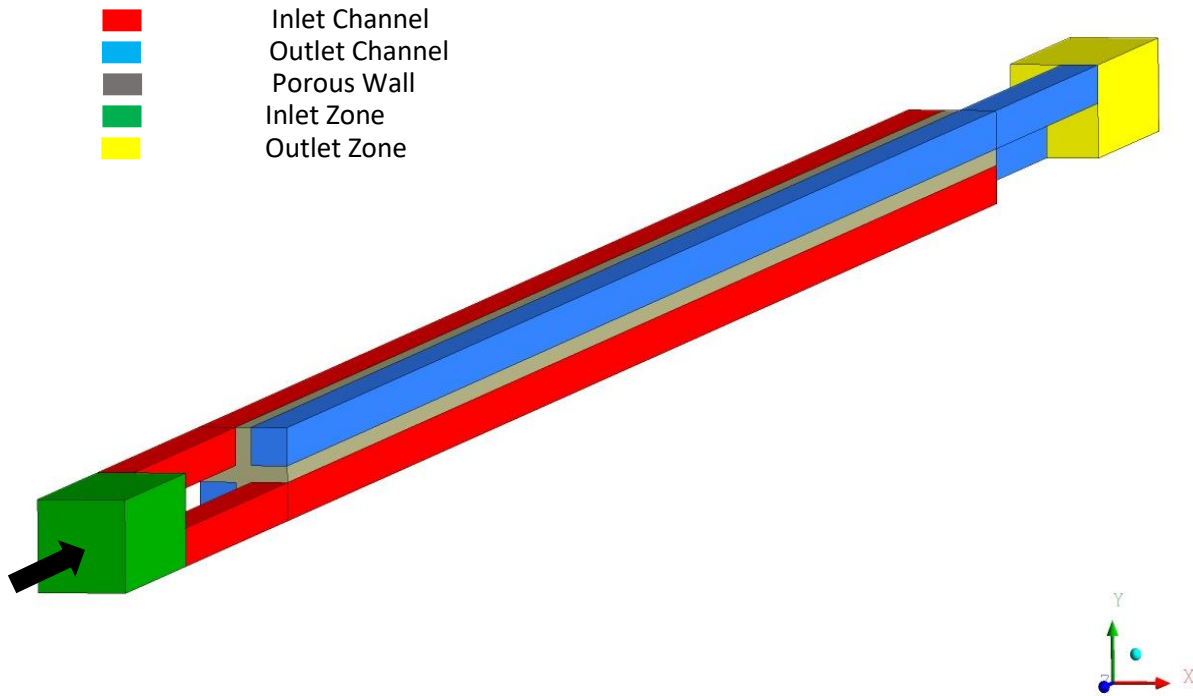
Figure 63. 3D GPF model.

The flow is considered to be laminar and incompressible in the channels. The 3D Navier-Stokes equations were solved via the finite volume method. An extra source term S was added to the N-S equation to resolve the pressure drop within the porous substrate, governed by Darcy's Law shown in Equation (30-31). The second term in the S equation represents the inertia-driven pressure drop, which is negligible compared to the Darcy term, due to the low magnitude of the wall velocity.

$$\nabla \cdot (\rho \vec{u} \cdot \vec{u}) = -\vec{\nabla}P + \nabla \cdot \vec{\sigma} + S \tag{30}$$

$$S = -\frac{\mu}{k_e}\vec{u} - \frac{1}{2}\beta\rho|\vec{u}|\vec{u} \tag{31}$$

CFD-based particle tracking was carried out to predict the particle deposition profile along the inlet channel. The Lagrangian method was used to track particles of different size, considering Brownian diffusion. Flow slip on the particle surface was taken into account by introducing the Stokes-Cunningham correction factor. Due to the randomness introduced by Brownian Diffusion, GDI-sized particles behave unpredictably after being injected into the channels. The fewer particles injected at a time, the more uncertain their deposition profile is. Thus, 6400 particles in each size bin were injected at the inlet to achieve a balance between particle tracking statistical stability and computational time required. The model predicted initial particle deposition profiles in Blank2 showcase the necessity of using 3D CFD modeling, as shown in **Figure 64**. The disparity between the normalized wall velocity profile and particle deposition profile, especially for small sized particles, demonstrates the insufficiency of assuming that particles always follow the streamline.
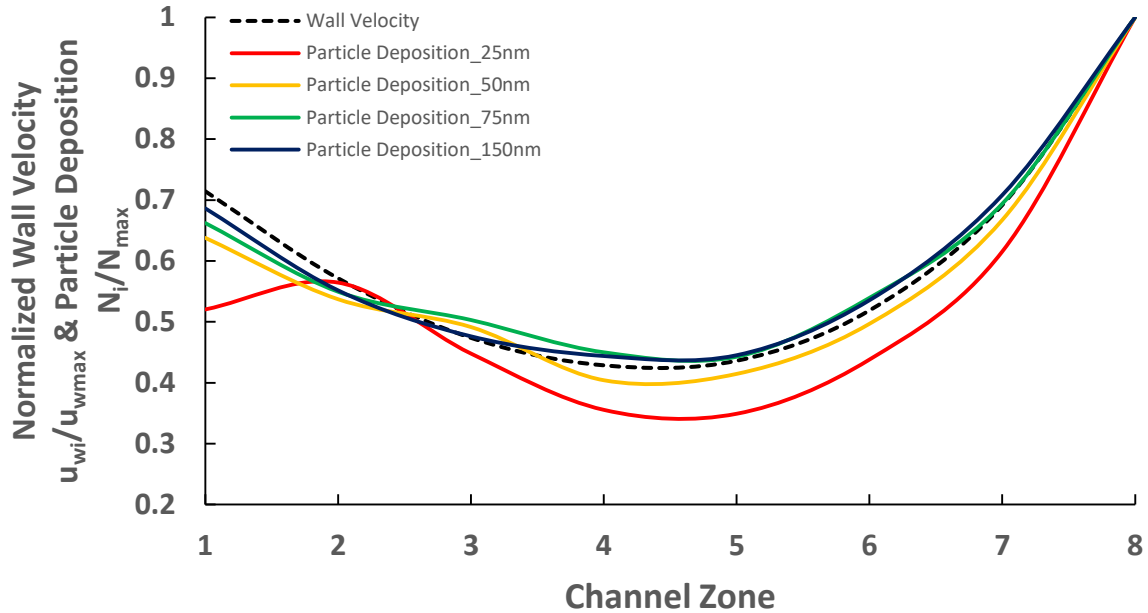
Figure 64. Normalized particle deposition profiles vs normalized wall velocity profile.

Filtration Model and UDF

There are three major functions of the UDF:

(1) Resolve size-dependent filtration efficiency

(2) Define initial wall properties

(3) Update wall properties with time

The classic unit cell model was incorporated in the UDF to predict the filtration performance of the target GPF [10, 88]. The UDF was triggered once particles contacted the surface of the porous wall, and the filtration efficiency was resolved for each particle. Modifications were made to the classic unit cell model to account for the channel corner effects and non-spherical morphology of GDI particulates. The modified filtration model is described in Equations (32-33).

$$E = 1 - e^{-\alpha} \tag{32}$$

$$\alpha = \left(\frac{4(1-\varepsilon)w(p)}{\pi \varepsilon d_c} \right) \left(E_D + l \cdot E_R + E_I \right) \tag{33}$$

The interception length scale, l, was introduced for the interception term E_R [22]. In this study, $l = 5$. Wall thickness, w, was redefined as a variable depending on the particle contact location on the wall. The CFD predicted flow field result of Blank2 at the initial state shows curving streamlines at the corner region (**Figure 65**). The curling streamlines elongate travel distance for particulates, and in turn, enhance the filtration performance.

(a) isometric view   (b) view normal to the inlet surface

Figure 65. CFD predicted streamline of Blank2 at initial state.

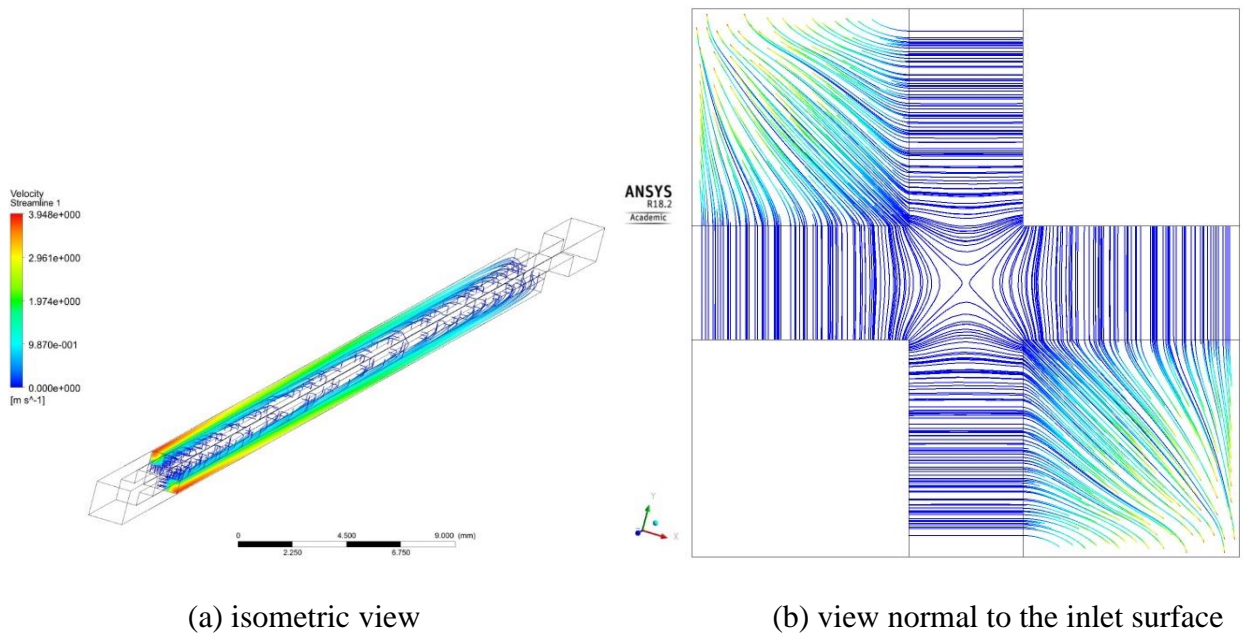An assumption was made that particles only loaded the top 1/7 of the porous wall, based on numerous post-mortem aging studies [7, 78]. Transition was included as an integrated part of the filtration model. The implementation of the transition model allowed for a smooth switch from

deep bed filtration to cake filtration [83]. For filtration modeling of ash loaded GPFs, assumptions were made that all trapped particles contributed to the cake development. Changes in the properties of porous wall and ash membrane were negligible.

The second function of the UDF is to assign initial wall properties. The main idea of the unit cell model is to simplify a porous medium to numerous randomly laid out unit collectors. The change of unit collector size and porosity locally is a direct response to the particle loading, and consequently alters the local permeability and filtration efficiency for the next time step. The porous wall properties of various GPF samples were distinguished by assigning their corresponding unit collector size and porosity through the UDF. For non-coated samples Blank1 and Blank2, unit collector size and porosity were the same for each channel zone. Whereas for washcoated GPFs, variable unit collector size and porosity were defined for different channel zones at the initial state. The initial permeability for each zone can be calculated using the equation below:

$$k(i,t) = k_0 \left(\frac{d_c(i,t)}{d_{c0}} \right)^2 \frac{f\left(\varepsilon(i,t)\right)}{f(\varepsilon_0)} \tag{34}$$

$$f(\varepsilon) = \frac{2}{9} \frac{\left[2 - \frac{9}{5}(1-\varepsilon)^{1/3} - \varepsilon - \frac{1}{5}(1-\varepsilon)^2 \right]}{1-\varepsilon} \tag{35}$$

d_{c0}, ε_0 are the intrinsic wall properties prior to washcoating. d_{c0} can be determined by

$d_{c0} = 1.5 \times \frac{1-\varepsilon_0}{\varepsilon_0} \hat{d}_p$. Similarly, k_0 is the wall permeability before washcoating, which can be

determined by $k_0 = \dfrac{\varepsilon_0^{5.5}}{5.6} \hat{d}_p^2$. The initial porosity and permeability of each channel zone for all GPF

models are shown in **Figure 66**.
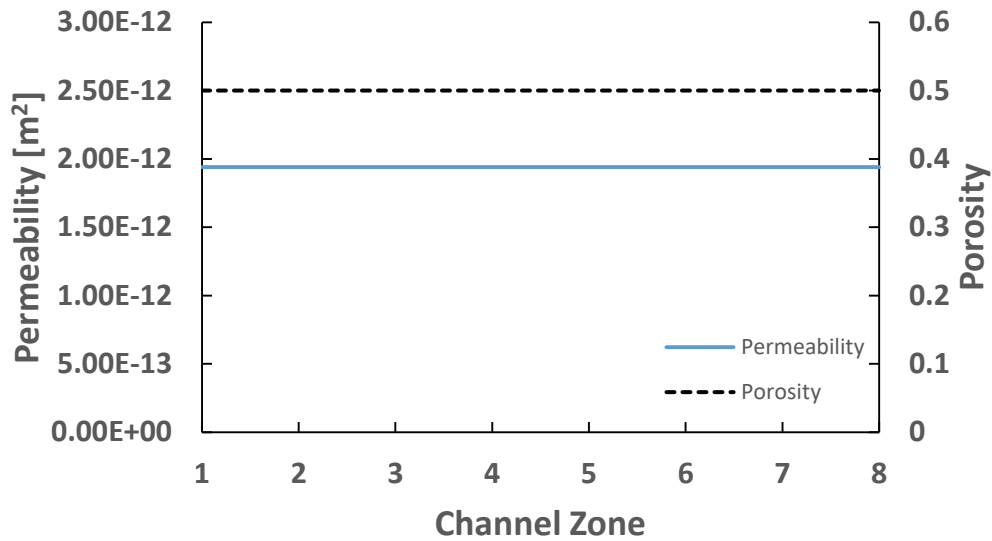
(a) Blank1
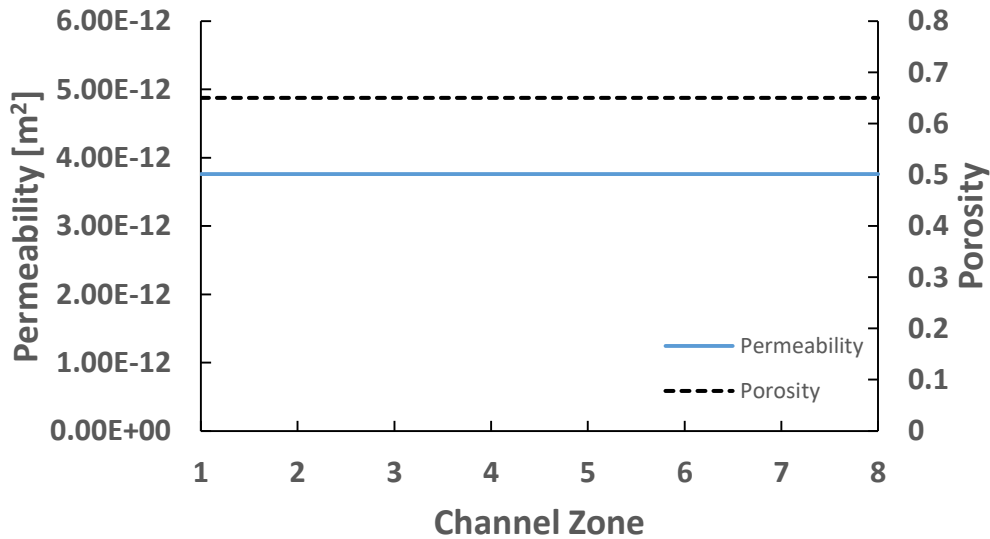
(b) Blank2

Figure 66. Initial porosity and permeability of each channel zone for (a) Blank1, (b) Blank2, (c) Washcaot1, (d) Washcoat2, (e) Washcoat3, (f) Washcoat4.
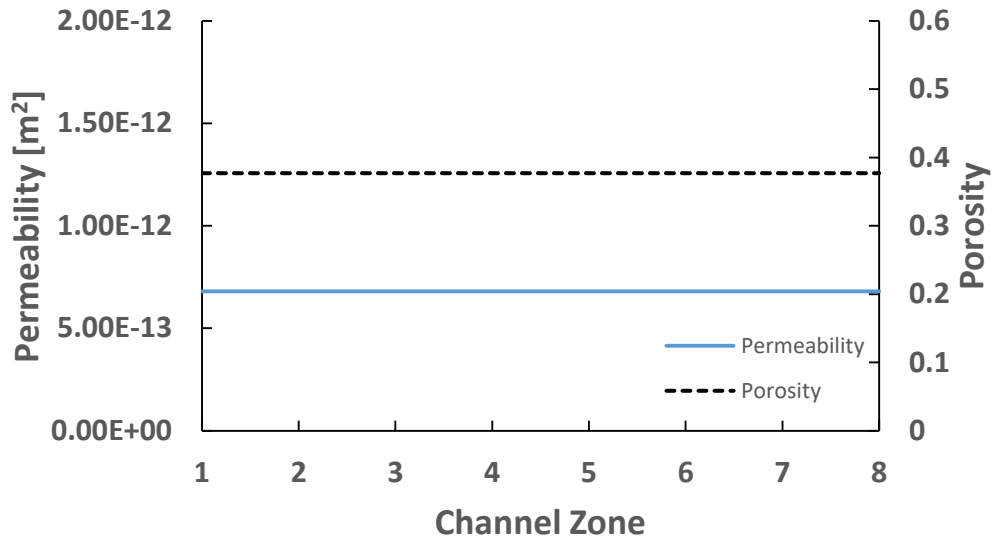
(c) Washcoat1
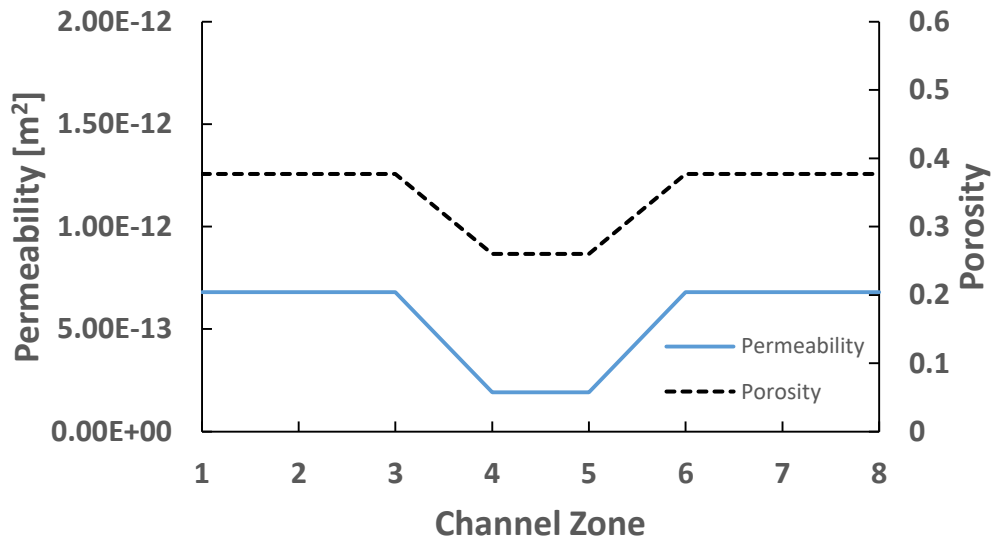
(d) Washcoat2

Figure 66. Continued.
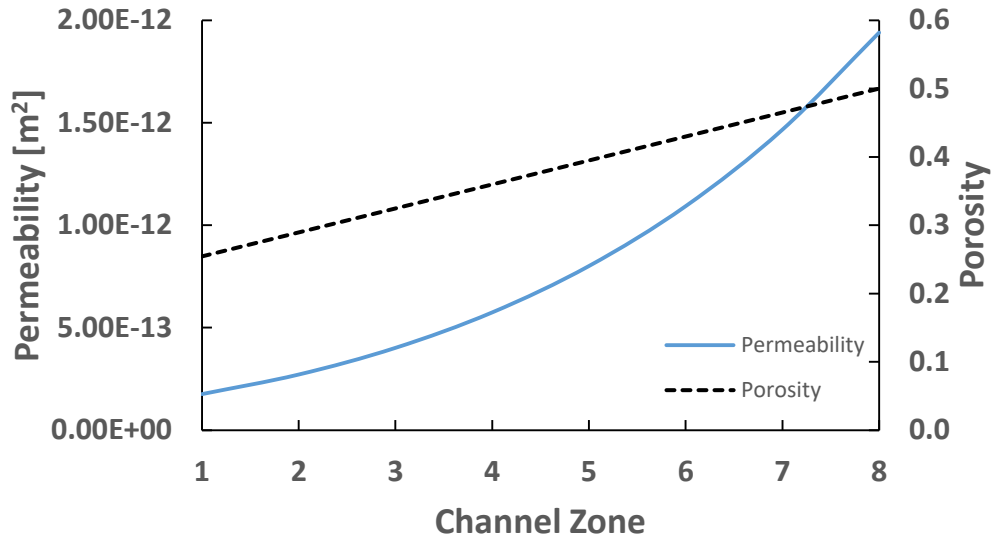
(e) Washcoat3
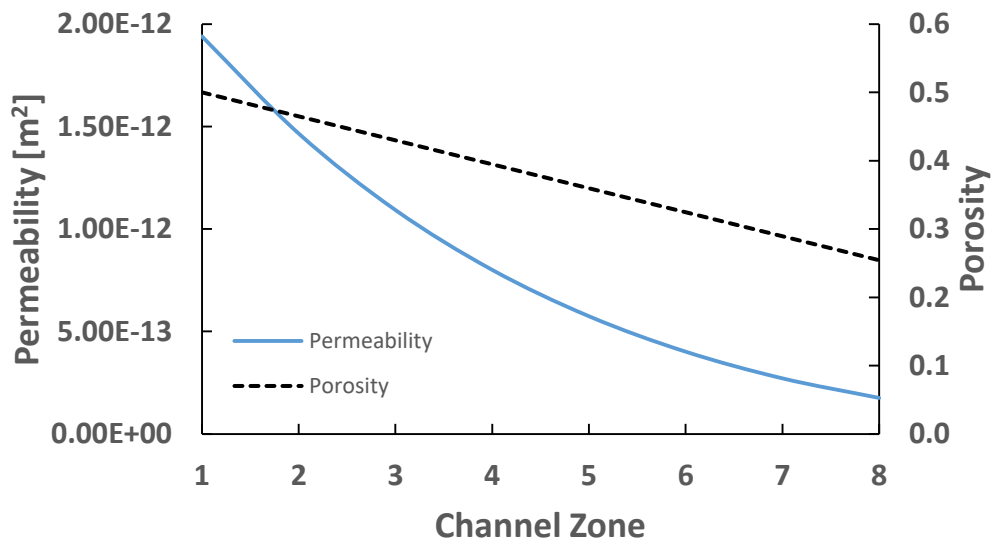
(f) Washcoat4

Figure 66. Continued.

The third function of the UDF is to update the wall properties, in particular the porosity and unit collector size of each zone, at every time step,. This is important for transient filtration and pressure drop simulation during particle loading. The UDF allows FLUENT to calculate the

current unit collector size and porosity of each channel zone based on the particle loading of the

last time step shown in Equations (36-37). The new permeability is updated based on the current

unit collector and porosity data, which is then fed to the FLUENT solver to predict the up-to-date

flow field and filtration efficiency.

$$d_c(i,t) = 2\left[\frac{3}{4\pi}V_{cell} + \left(\frac{d_c(i,t-1)}{2}\right)^3\right]^{1/3} \tag{36}$$

$$\varepsilon(i,t) = 1 - \left(\frac{d_c(i,t)}{d_{c0}}\right)^3 \cdot (1-\varepsilon_0) \tag{37}$$

A flowchart is presented in **Figure 67** to show how the UDF achieves the aforementioned

functions.
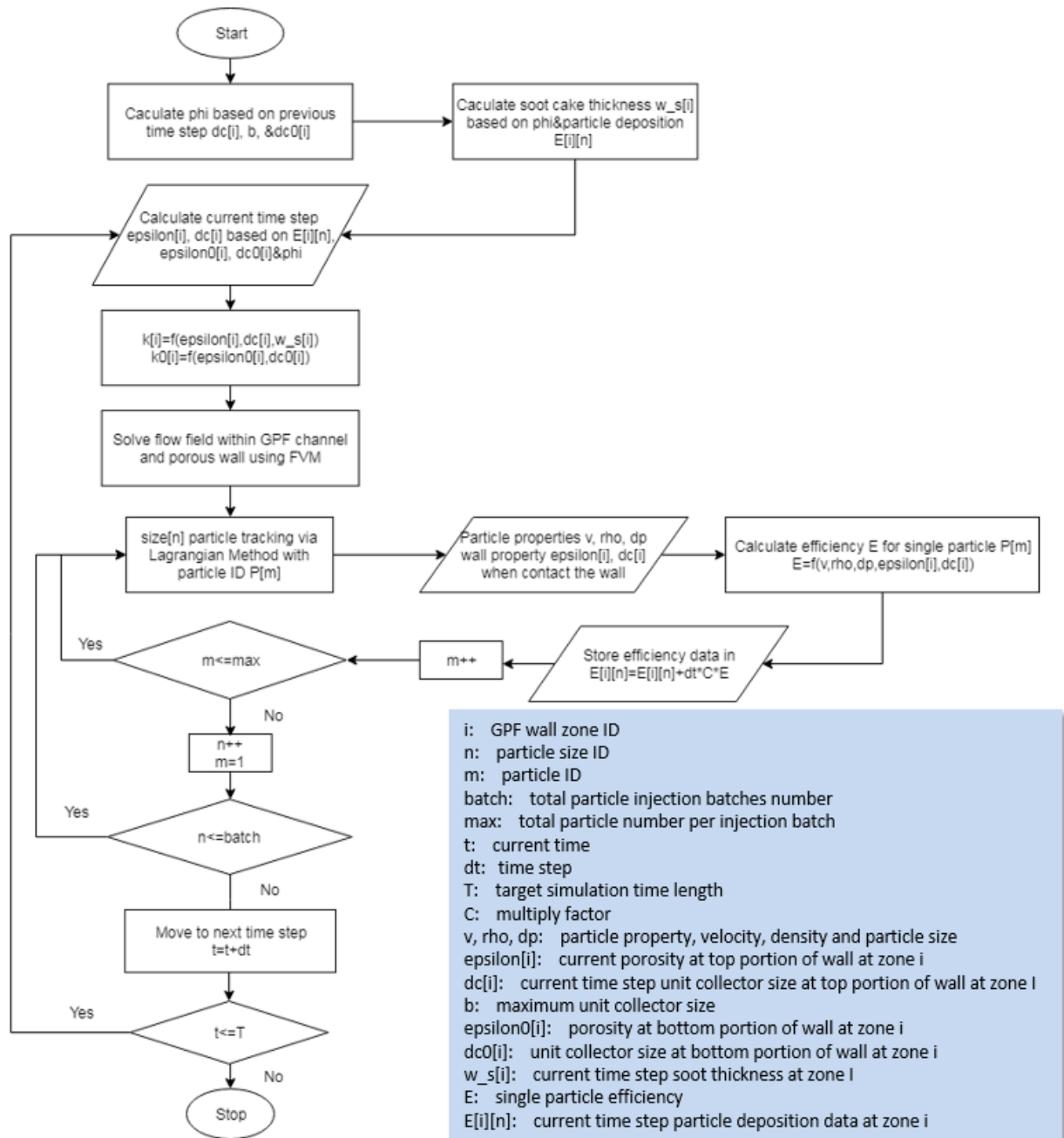
Figure 67. UDF flowchart.

The 3D CFD model with the UDF was first validated against the experimental data of Blank1 and Blank2, then further validated against data of Washcoat1. After validation, model was used to investigate the wall heterogeneity effects on its performance, by modeling the transient

filtration efficiency and pressure drop behavior of Washcoat2, Washcoat3, Washcoat4, Ash1, Ash2 and Ash3.

Results and Discussion

Model Validation

The model was validated against the initial size-dependent filtration efficiency data of Blank2 at multiple space velocities. The data was measured at 15,000 hr^{-1}, 30,000 hr^{-1} and 60,000 hr^{-1} respectively and the model predicted filtration efficiency shows a great match with the experiments, as indicated in **Figure 68**.
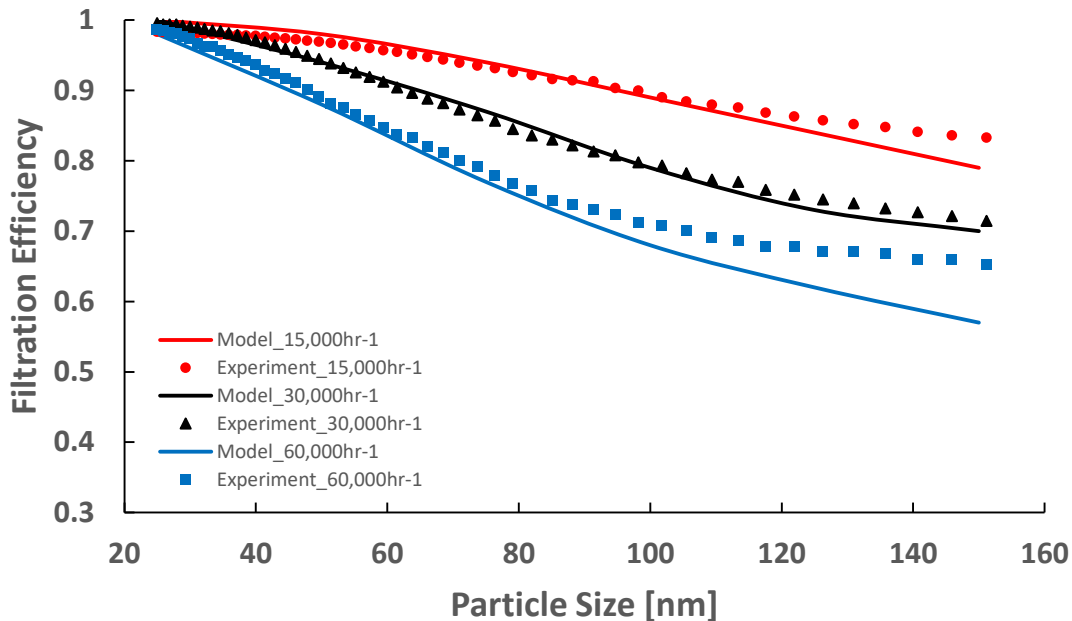
Figure 68. Model predicted initial filtration efficiency of Blank2, validated by experimental data at 15,000 hr^{-1}, 30,000 hr^{-1} and 60,000 hr^{-1}.

The transient size-dependent filtration efficiency of Blank2 from [70] was also used to validate the model. This experiment was conducted at room temperature with 30,000 hr^{-1} inlet

flow. The incoming particle concentration was fixed at 0.4 mg/m3. The model predicted filtration

results are compared with the experiment and manage to match the experiment well, as shown in

Figure 69.
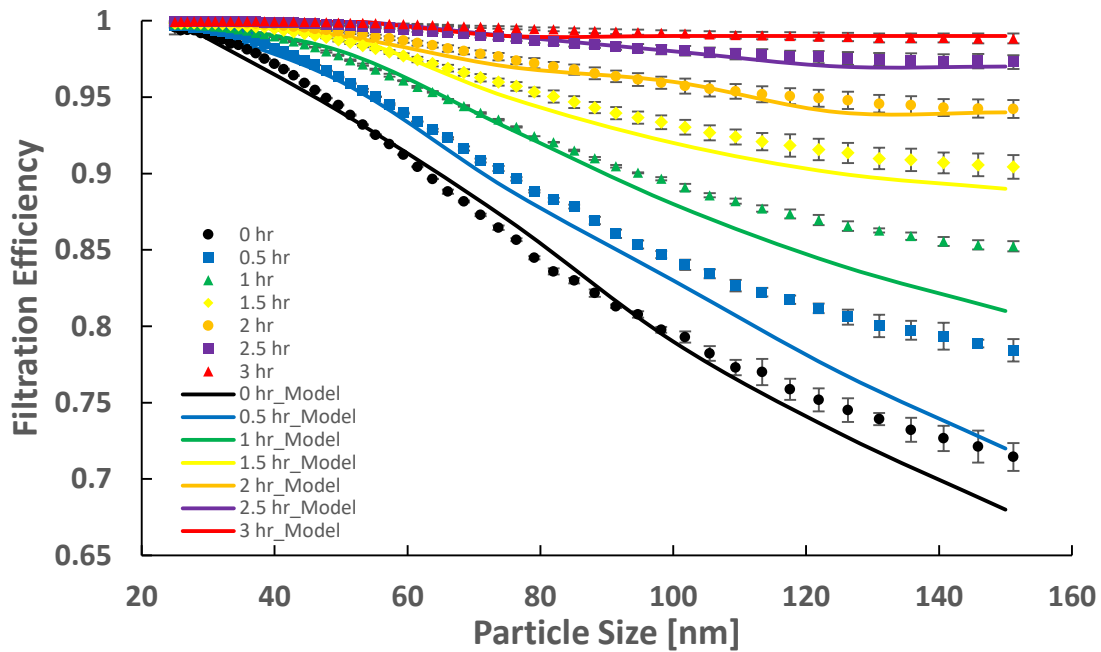
Figure 69. Model predicted transient filtration efficiency of Blank2, validated by experimental data at 30,000 hr^{-1}.

Given the assumption that particles only load in and on the top 1/7 of the wall, details about

the dynamic wall porosity profile change are presented in **Figure 70**. The channel zone porosity

decreases in response to the particle loading. Note that the porosity profile during the early loading

stage roughly matches the wall velocity profile, where more particles are trapped in the front and

back of the wall. The decreasing rate of porosity of each channel zone depends on the local

permeability and particle loading rate. For a given zone, the lower its porosity is, the lower its

permeability, and the fewer particles that will deposit in this zone during the next time step. This

result shows that the porosity profile starts from a uniform state and then gradually grows a hump

in the middle and ends up with a uniform profile with lower porosity magnitude. Due to the low incoming particle concentration and short simulation time duration, very little cake is formed.
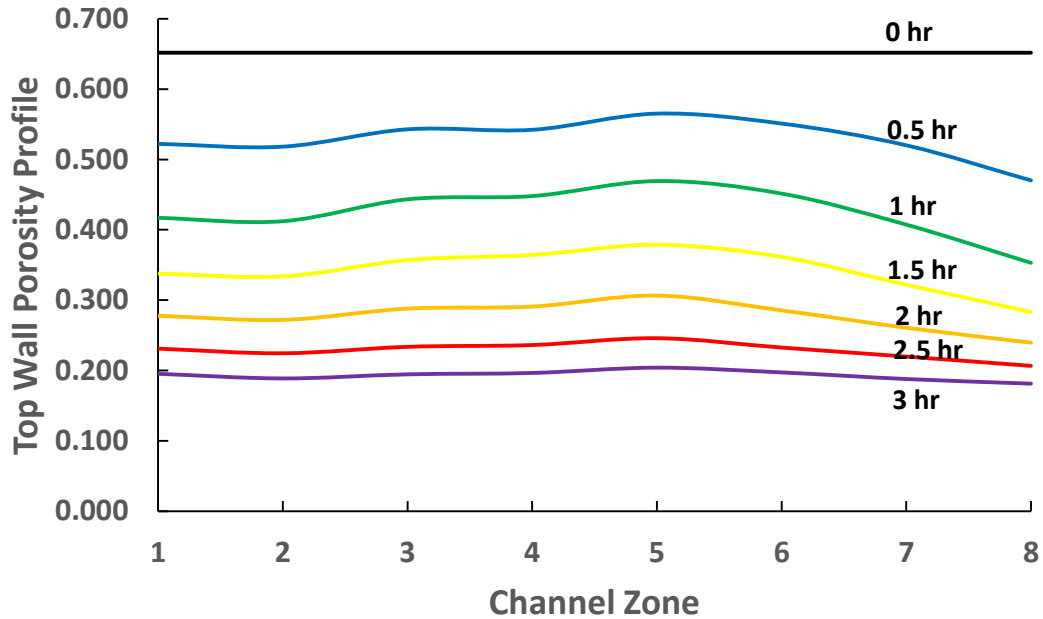
Figure 70. Dynamic top wall porosity profile change with time.

The model was further validated against the particulate loaded filtration and pressure drop data of Blank1. The experiment was run at room temperature at 23,000 hr^{-1}. Unlike Blank2, the Blank1 sample was exposed to an incoming flow with much higher particle concentration (15 mg/m^{3}). This higher particle concentration led to a fast transition from deep bed filtration to cake filtration, and in turn induced a quick buildup of a cake. The predicted mass-based filtration efficiency and pressure drop in comparison with the experiment are shown in **Figure 71**.
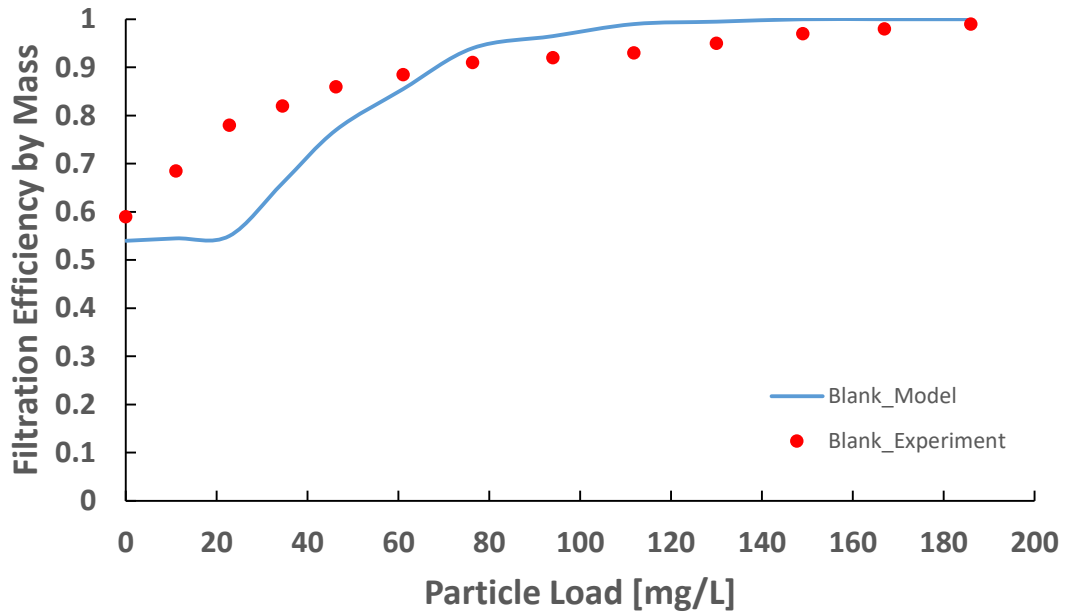
(a) Mass based filtration efficiency
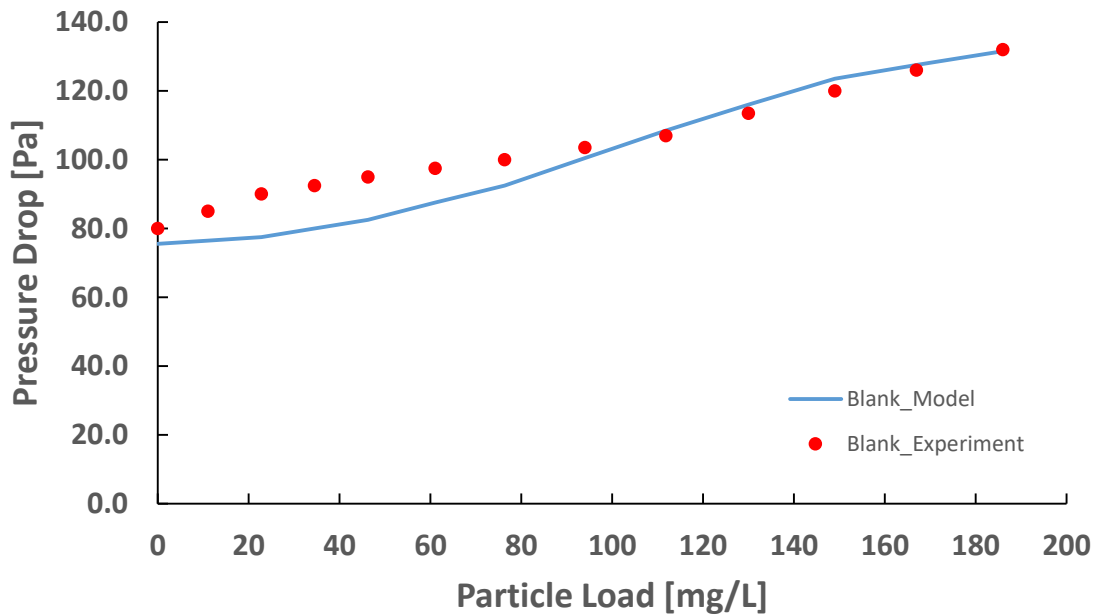
(b) Pressure drop

Figure 71. Model predicted transient filtration efficiency of Blank1, validated by experimental data at 23,000 hr^{-1}.

The model predicted dynamic wall porosity and cake profiles are shown in **Figure 72**. Note that the filtration mechanism makes the switch from deep bed to cake at ~150 mg/L. A similar trend of the wall porosity profile change is observed here, where it ends up uniform at a lower magnitude. However, the cake profile stays non-uniform throughout the loading process. The cake at the front and back of the wall maintains a higher thickness than that of the middle. Up until the filtration mechanism switching point, there has been an average of 1um in particulate accumulation on top of the wall, which increases the overall wall permeability to a large extent. As a consequence, the wall velocity profile flattens and induces a more even particle deposition, which sustains the non-uniform cake profile.
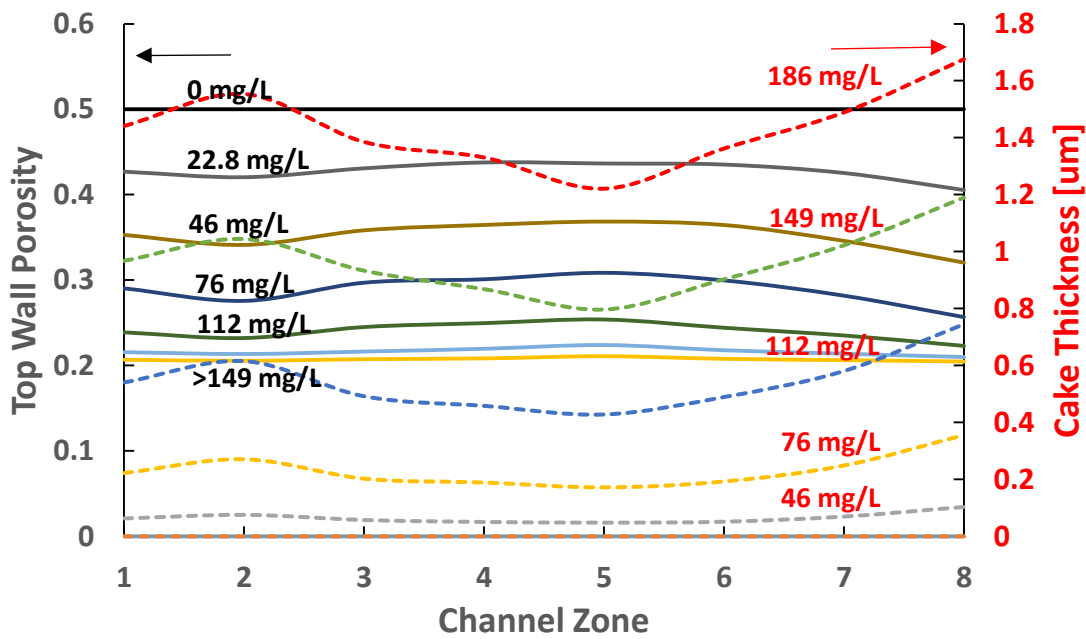
Figure 72. Dynamic top wall porosity profile and cake distribution.

Finally, the model was validated against the experimental data of Washcoat1. The experimental conditions were the same as for Blank1, at room temperature and at 23,000 hr^{-1}. The

results are shown in **Figure 73**, where it can be seen that the predicted filtration efficiency matches the experimental data well except in the very early loading stage, where the model yields a higher filtration efficiency during the initial 20 mg/L of particle loading. This is attributed to the way the washcoat is modeled in the UDF, where it is assumed to be evenly coated on the unit collectors. An extra layer of thickness is added to the unit collectors depending on the washcoat amount and density. This manner of washcoat modeling is identical to that of the particulate loading process, which justifies the higher predicted filtration efficiency during the early loading stage.
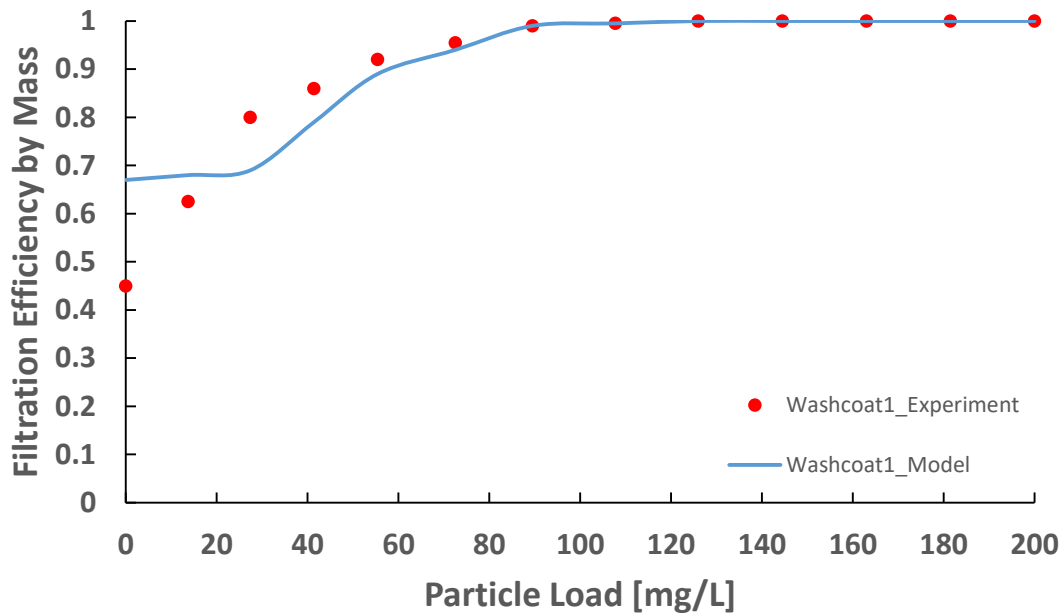
(a) Mass based filtration efficiency

Figure 73. Model predicted transient filtration efficiency of Washcoat1, validated by experimental data at 23,000 hr^{-1}.
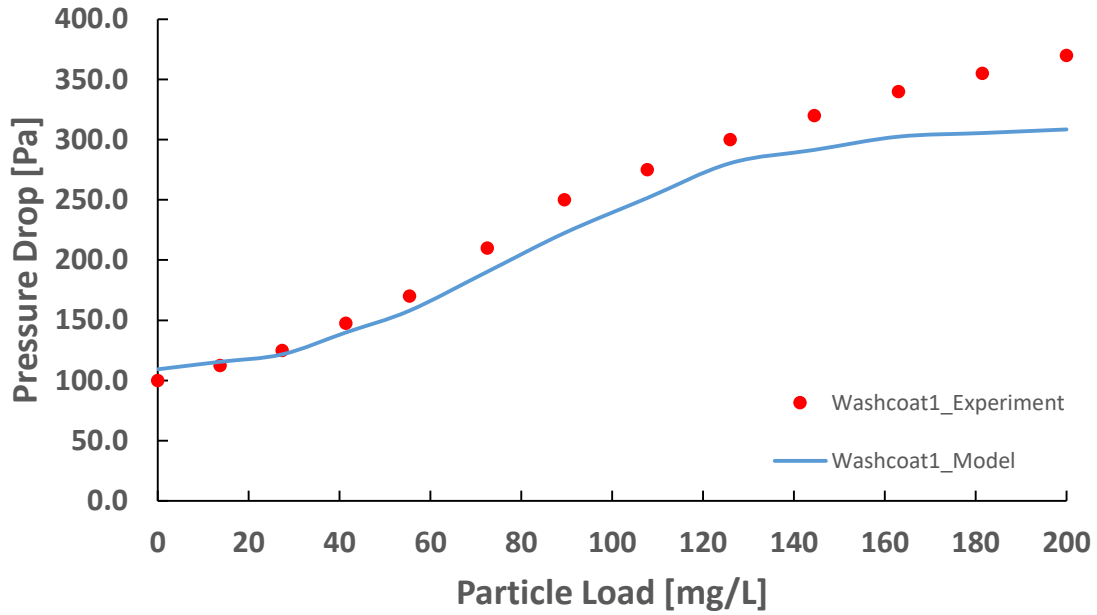
(b) Pressure drop

Figure 73. Continued.

A similar trend for the wall porosity profile change and cake profile development is observed in **Figure 74**. A faster transition from deep bed to cake filtration is observed in the Washcoat1 case, attributed to the washcoat-driven lower initial porosity. The transition happens at ~125 mg/L, matching what the transient pressure drop result suggests in **Figure 73**.
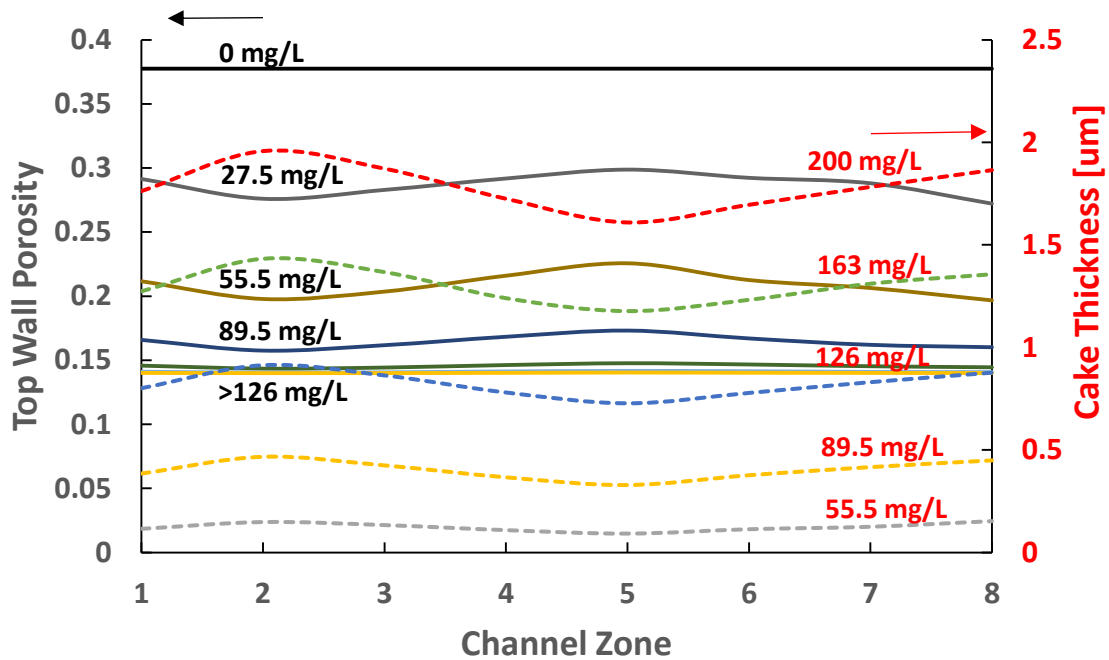
Figure 74. Transient top wall porosity profile and cake distribution.

Effects of Washcoat Variations on GPF Performance

The model predicted filtration and pressure drop results of Washcoat2, Washcoat3 and Washcoat4 are compared to Washcoat1 and Blank1 in **Figure 75**. All washcoated GPFs show a better filtration performance than the Blank sample, at the cost of a much higher pressure drop. Comparing to Washcoat1, Washcoat2, which possesses a coating overlap, yields similar filtration performance during loading. Despite the fact that the low permeability region of the wall can push upstream flow to the front and back of the channel, causing a higher local wall velocity. The higher wall velocity invokes a faster growth of a cake to compensate the deterioration of the diffusion filtration mechanism. However, the very same high wall velocity results in a higher pressure drop at regions outside the overlap. Another drawback of Washcoat2 is its high manufacture cost. The washcoat overlap applies more precious metal, which increases the cost without an evident performance increase. Washcoat3 and Washcoat4 behave quite similarly in terms of filtration and

pressure drop, but they both yield a lower filtration efficiency than Washcoat1. Among all washcoat variations, Washcoat1, with the uniform coating profile demonstrates the best overall performance.
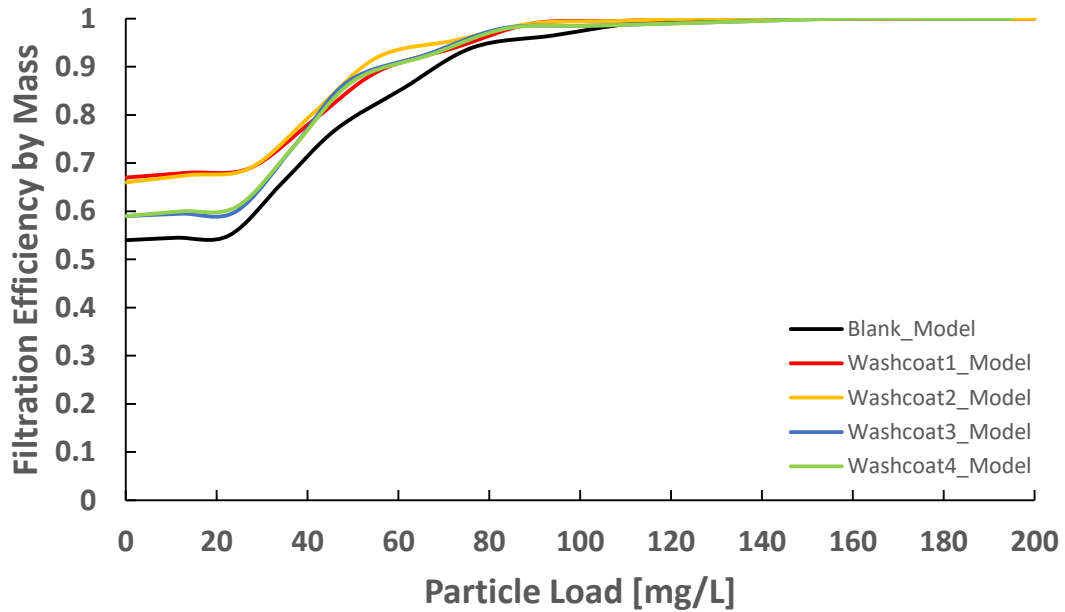
(a) Mass based filtration efficiency

Figure 75. Model predicted transient filtration and pressure drop of washcoat variations in comparison with Washcoat1 and Blank1.
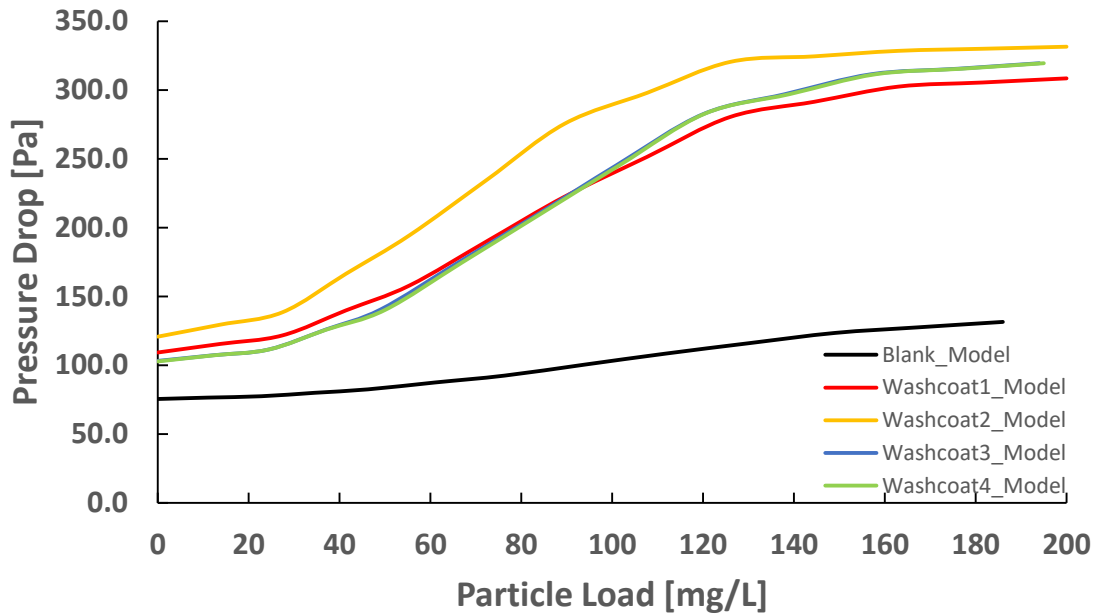
(b) Pressure drop

Figure 75. Continued.

More results from these washcoat variations is shown in **Figure 76**. Washcoat2 sees an even faster filtration transition than Washcoat1, at ~90 mg/L. Up until 200 mg/L particle loading, a center-dipping cake profile is seen. The high washcoat loading up front in Washcoat3 directs incoming flow to the channel end, as a result of which the cake grows faster at the back of the channel. The opposite happens in Washcoat4, where the cake grows faster at the front of the channel.

118
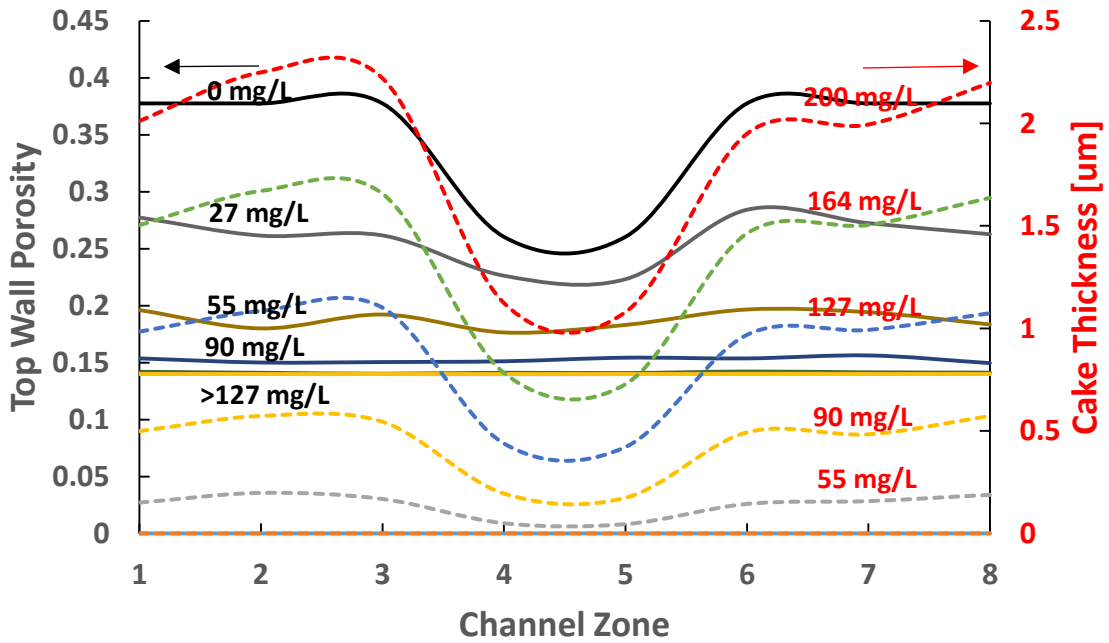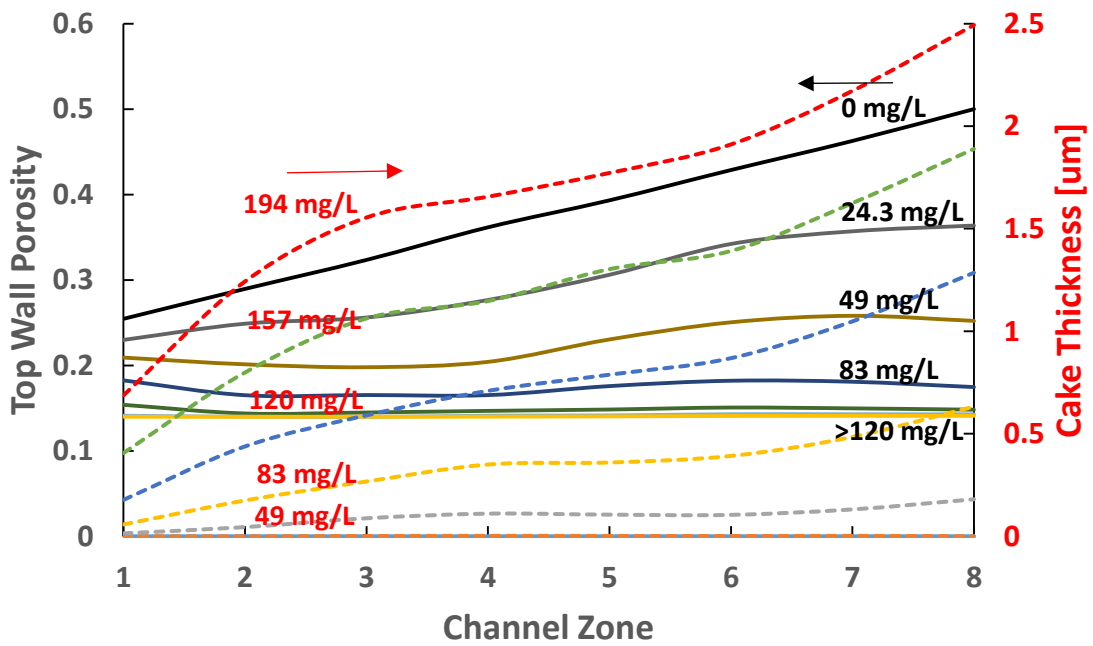
(a) Washcoat2

(b) Washcoat3

Figure 76. Dynamic top wall porosity and cake profile with washcoat variation.

119
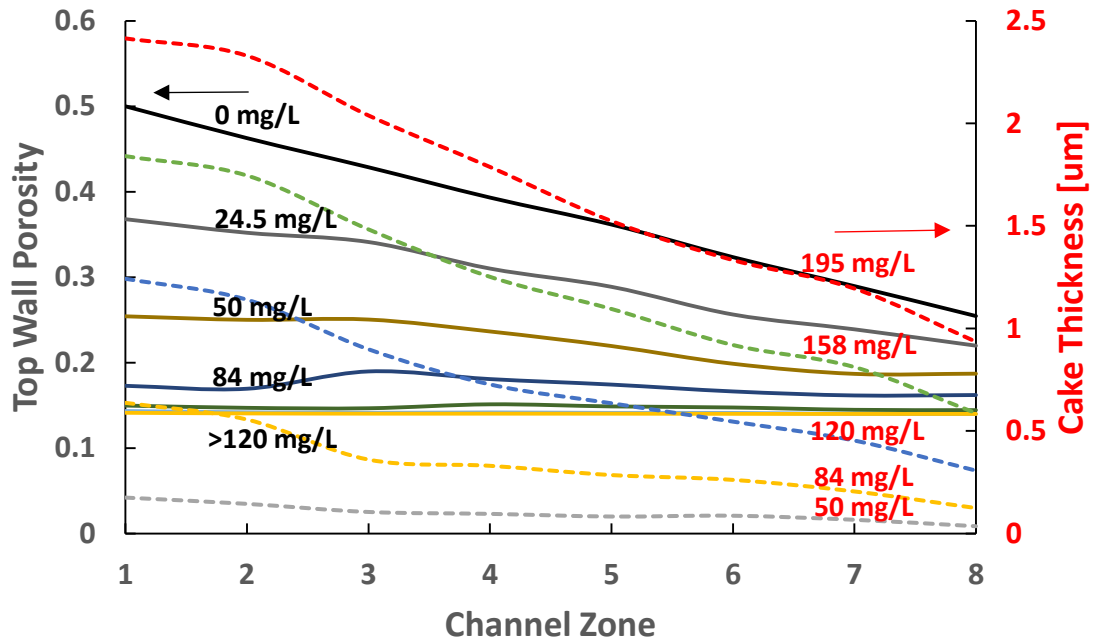
(c) Washcoat4

Figure 76. Continued

Effects of Artificial Ash Membrane on GPF Performance

The filtration and pressure drop performance of Ash1, Ash2 and Ash3 were simulated during particle loading, with incoming flow space velocity of 23,000 hr^{-1}, particle concentration of 15 mg/m^3 and loaded up to 200 mg/L. The model predicted results are compared to that of Blank1, as shown in **Figure 77**. The ash loaded GPFs have a much higher filtration efficiency than Blank1 due to the application of the ash membrane. A thin, 0.5 um, ash membrane is able to enhance the initial filtration efficiency from 55% to almost 80%. An ash membrane of 1.5 um thickness can \ achieve a nearly 95% initial filtration efficiency. As for the pressure drop, Ash1, Ash2 and Ash3 all yield a slightly higher pressure drop than Blank1, however, all ash loaded GPFs undergo cake filtration during the entire process and skip the deep bed filtration, which results in a much slower and linear pressure drop increase than Blank1. Thus, under standard working

conditions, Blank1 has a 110 Pa pressure drop to reach 95% filtration efficiency. Whereas for ash loaded GPFs, the pressure drop is approximately 80Pa. Based on the results in **Figure 77,** Ash3 possesses the optimal ash membrane thickness (2.6 g/L in equivalence) for Blank1. The continuous thermal regeneration makes it hard to grow a particulate cake on the ash loaded wall. This emphasizes the importance of the initial filtration performance of a GPF with an ash membrane. Ash loading less than 2.6 g/L is shown to be insufficient at the early stage of loading, while ash loading larger than 2.6 g/L is undesirable due to the higher pressure drop.
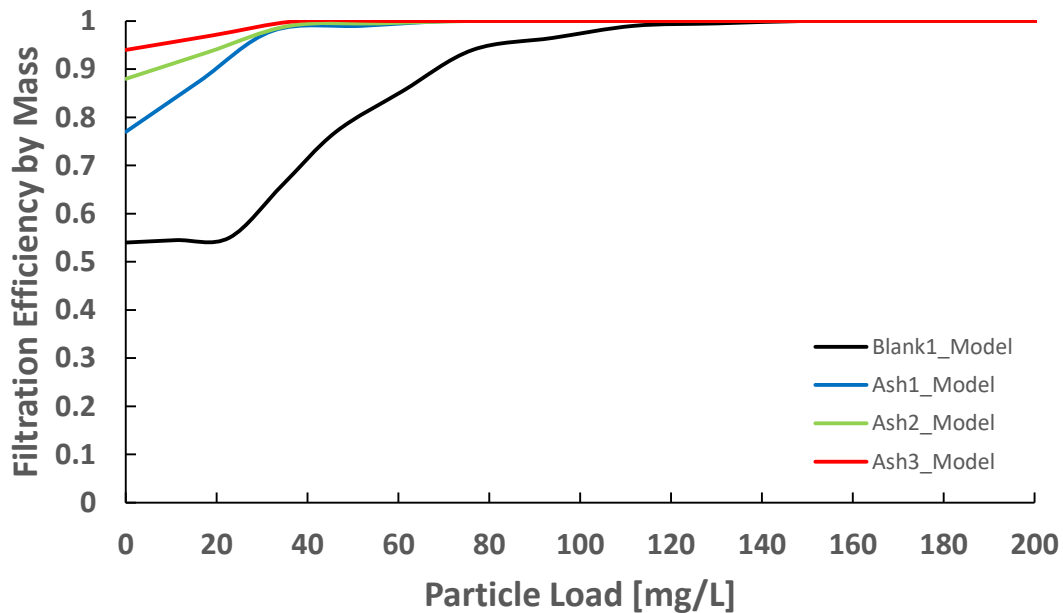
(a) Mass based filtration efficiency

Figure 77. Model predicted transient filtration and pressure drop of Ash1, Ash2 and Ash3 in comparison Blank1.
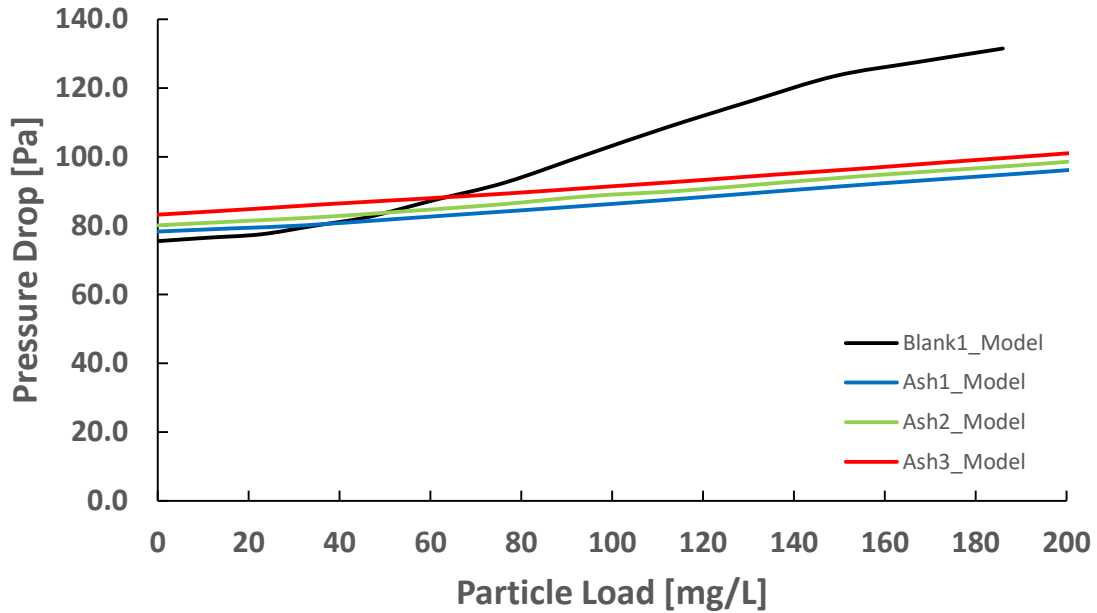
(b) Pressure drop

Figure 77. Continued.

For Ash1, Ash2 and Ash3, all particle capture is assumed to occur on the ash membrane surface. The trapped particles are devoted directly towards cake formation. The properties of the porous wall and ash membrane are assumed to stay fixed during loading. Therefore, the dynamic cake profile is shown in **Figure 78**. All three ash loaded GPFs develop a center-dipping cake profile, where more particulate is accumulated in the front and back of the inlet channel. Ash3 shows a slightly faster cake growth overall due to the higher initial filtration efficiency than Ash1 and Ash2.
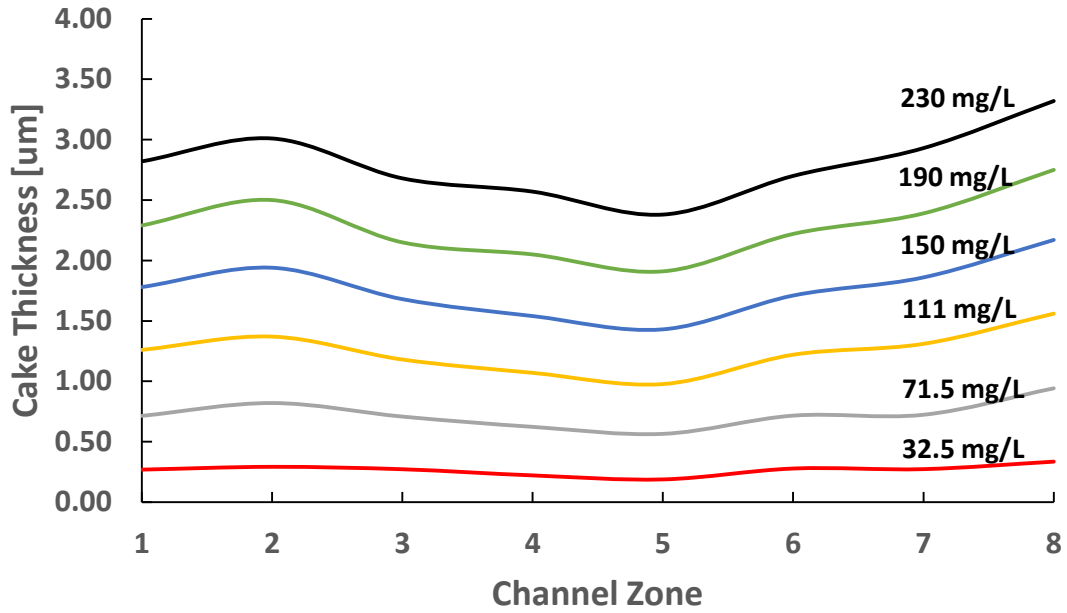
(a) Ash1
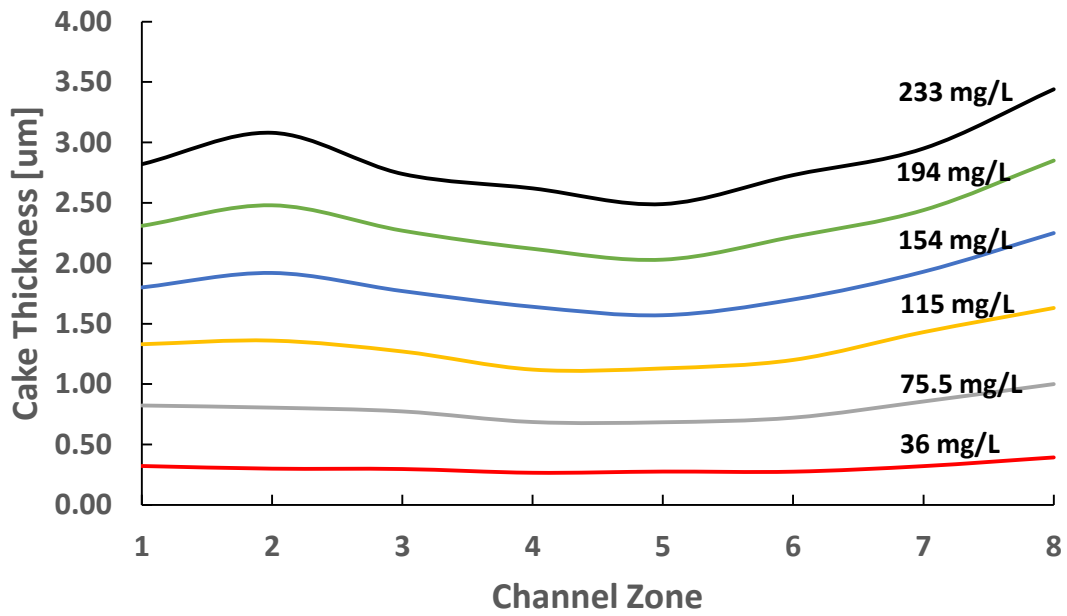
(b) Ash2

Figure 78. Dynamic cake profile of Ash1, Ash2 and Ash3.
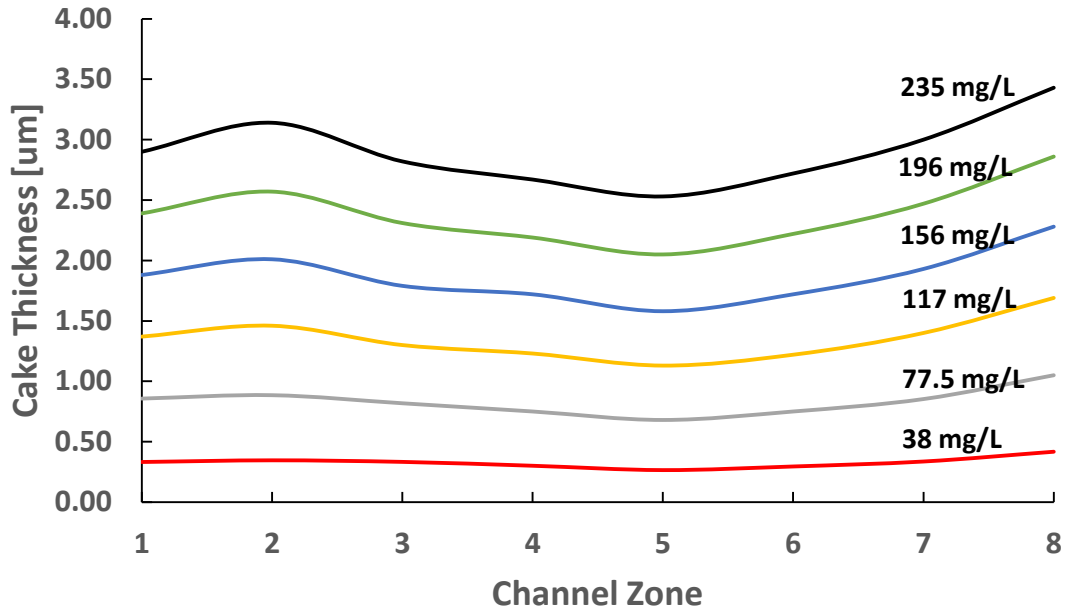
(c) Ash3

Figure 78. Continued.

Conclusions

The 3D CFD model with the UDF was validated by experimental data and demonstrated its capability of predicting the transient filtration efficiency and pressure drop of uncoated and washcoated GPFs. Additional information about the dynamic wall properties and cake profile change can be extracted from this model, as compared to others.

Among all possible washcoating profiles considered in this study, the uniform washcoating showed the most promising performance regarding filtration efficiency and pressure drop. Washcoating overlaps in the middle of the channel can degrade the GPF performance by increasing the pressure drop too much as compared to the evenly washcoated GPF. Washcoating overlap is also inefficient with respect to cost.

Application of an ash membrane on top of the wall can effectively enhance its filtration capability and reduce the overall pressure drop achieved in the long term. Use of a 1.5 um thick ash membrane is recommended for the Blank1 sample to keep a balance between high filtration efficiency and low pressure drop for use in vehicles.

CHAPTER VI

CONCLUSIONS

GPFs will be required in the GDI exhaust aftertreatment system, in order to meet strict regulations for particulate matter emissions. In support of this assertion, this study explores approaches to improve the performance of GPFs with respect to the filtration efficiency and pressure drop. Four major conclusions are summarized below:

(1) DPFs are not sufficient for GDI engine particulates filtration. GDI specific GPFs with particular pore size and porosity characteristics are needed.

(2) The microstructure of the GPF substrate, specifically the pore size distribution, is proven to be impactful to performance. An optimized pore size distributions was found using pores small enough ($a < 10 \mu m$) to diverge the flow and large enough ($5 \mu m < a$) to allow a fraction of flow pass, which is a good balance for particle filtration without a large increase in pressure drop. A new GPF design was proposed with top 2/5 of the substrate wall consisting of small sized pores and the remainder large sized pores. Simulation of the new wall substrate design projects an 8% increase in filtration efficiency across all particle sizes, at the expense of only a 7 Pa higher pressure drop (17.5% increase on baseline).

(3) The throat unit collector was developed to better represent the pore size, cavity size and their connectivity in the GPF substrate. Simulations demonstrated its capability of predicting the GPF filtration efficiency at both initial and transient states. The throat unit collector model offers an extra degree of freedom compared to the classic unit cell model, by allowing the configuration of cavity size. The simulation results using the throat unit collector model show that the GPF wall

consisting of whole 1:1 diameter ratio throat unit collectors could potentially yield the highest initial overall filtration efficiency.

(4) GPF wall heterogeneity effects were investigated considering washcoating effects and the effect of an ash membrane. A 3D CFD model utilizing a novel UDF was developed to predict the GPF filtration and pressure drop behavior. The simulation results show that uniform washcoating has the most promising performance regarding the filtration efficiency and pressure drop. Washcoating overlap can produce a significant pressure drop increase compared to the uniformly washcoated GPF. Washcoating overlap is also inefficient with respect to cost due to the redundant precious metal application. An evenly distributed ash membrane on top of the GPF wall was shown to effectively enhance its filtration capability and reduce the pressure drop in a long term. 2.6 g/L of ash load (1.5um ash membrane or "cake" thickness) is recommended to keep a balance between high filtration efficiency and low pressure drop.

The 3D CFD model alongside the UDF is a powerful and versatile tool that can be used for not only GPF modeling, but also DPF modeling with minor modifications. In addition to the common axial direction particle deposition profile, the UDF is also able to predict the particle deposition profile on the channel in the lateral direction. This may be quite beneficial to gaining insight of the locations of soot/ash deposition during loading, considered the inlet channel corner effects. The UDF could be used to further expand the GPF channel discretization and split the GPF wall into more zones, to offer higher simulation resolution at little additional computation time cost. If computational resources allow, a smaller time step could be used in the GPF transient simulation. Moreover, the UDF has the potential to apply the artificial ash membrane in different profiles, which may yield better performance. Finally, our research group is planning to convert the UDF into CONVERGE code that is compatible with the CONVERGE CFD software by

Convergent Science. CONVERGE features autonomous meshing, adaptive mesh refinement and coupled chemistry, which makes it a suitable tool for GPF soot loading and regeneration simulation. CONVERGE along with the custom UDF would also make it possible to evaluate the catalytic conversion performance of GPFs with different washcoating profiles.

REFERENCES

1. Gladstein, N., *Ultrafine particulate matter and the benefits of reducing particle numbers in the United States.* A report to the manufacturers of Emissions Controls Association (MECA), 2013.

2. Maricq, M. *How are emissions of nuclei mode particles affected by emission control.* in *HEI-conference May.* 2009.

3. Johnson, T., *Vehicular emissions in review.* SAE International Journal of Engines, 2016. **9**(2016-01-0919): p. 1258-1275.

4. Johnson, T. and A. Joshi, *Review of Vehicle Engine Efficiency and Emissions.* 2017, SAE Technical Paper.

5. Heyder, J., *Deposition of inhaled particles in the human respiratory tract and consequences for regional targeting in respiratory drug delivery.* Proceedings of the American Thoracic Society, 2004. **1**(4): p. 315-320.

6. Donaldson, K., et al., *Nanoparticles and the cardiovascular system: a critical review.* Nanomedicine, 2013. **8**(3): p. 403-423.

7. Lambert, C.K., et al., *Analysis of High Mileage Gasoline Exhaust Particle Filters.* SAE International Journal of Engines, 2016. **9**(2016-01-0941): p. 1296-1304.

8. Badshah, H., D. Kittelson, and W. Northrop, *Particle Emissions from Light-Duty Vehicles during Cold-Cold Start.* SAE International Journal of Engines, 2016. **9**(2016-01-0997): p. 1775-1785.

9. Bissett, E.J., *Mathematical model of the thermal regeneration of a wall-flow monolith diesel particulate filter.* Chemical Engineering Science, 1984. **39**(7-8): p. 1233-1244.

10. Konstandopoulos, A.G. and J.H. Johnson, *Wall-flow diesel particulate filters—their pressure drop and collection efficiency*. 1989, SAE Technical Paper.

11. Sheppard, J., P. Yang, and A. Strzelec, *Modeling and Experimentation of GDI-sized Particulate Filtration and Pressure-drop Behavior in Uncoated Commercial DPF Substrates*. 2019, SAE International.

12. Liati, A., et al., *Microscopic investigation of soot and ash particulate matter derived from biofuel and diesel: implications for the reactivity of soot.* Journal of Nanoparticle Research, 2012. **14**(11): p. 1224.

13. Konstandopoulos, A.G., et al., *Fundamental studies of diesel particulate filters: transient loading, regeneration and aging*. 2000, SAE Technical Paper.

14. Konstandopoulos, A.G., E. Skaperdas, and M. Masoudi, *Inertial contributions to the pressure drop of diesel particulate filters*. 2001, SAE Technical Paper.

15. Konstandopoulos, A.G., *Flow resistance descriptors for diesel particulate filters: definitions, measurements and testing*. 2003, SAE Technical Paper.

16. Sheppard, J., *Size-dependent filtration of cakeless diesel particulate filters*, in *Mechanical Engineering*. 2014, Texas A&M University: College Station, TX.

17. Dalla Nora, M., T.D.M. Lanzanova, and H. Zhao, *Effects of valve timing, valve lift and exhaust backpressure on performance and gas exchanging of a two-stroke GDI engine with overhead valves.* Energy Conversion and Management, 2016. **123**: p. 71-83.

18. Payatakes, A.C., C. Tien, and R.M. Turian, *A new model for granular porous media: Part I. Model formulation.* AIChE Journal, 1973. **19**(1): p. 58-67.

19. Lee, K.W. and J.A. Gieseke, *Collection of aerosol particles by packed beds.* Environmental Science & Technology, 1979. **13**(4): p. 466-470.

20.   Kuwabara, S., *The forces experienced by a lattice of elliptic cylinders in a uniform flow at small Reynolds numbers.* Journal of the Physical Society of Japan, 1959. **14**(4): p. 522-527.

21.   Gong, J. and C.J. Rutland, *Filtration characteristics of fuel neutral particulates using a heterogeneous multiscale filtration model.* Journal of Engineering for Gas Turbines and Power, 2015. **137**(11): p. 111507.

22.   Gong, J., et al., *Importance of filter's microstructure in dynamic filtration modeling of gasoline particulate filters (GPFs): Inhomogeneous porosity and pore size distribution.* Chemical Engineering Journal, 2018.

23.   Jorgensen, J., et al. *The Effect of Ash Accumulation on Gasoline Particulate Filters: A Comparison Between Laboratory and Field Aged Samples.* in *ASME 2014 Internal Combustion Engine Division Fall Technical Conference.* 2014. American Society of Mechanical Engineers.

24.   Sappok, A., et al., *Theoretical and experimental analysis of ash accumulation and mobility in ceramic exhaust particulate filters and potential for improved ash management.* SAE International Journal of Fuels and Lubricants, 2014. **7**(2014-01-1517): p. 511-524.

25.   Custer, N., et al., *Lubricant-derived ash impact on gasoline particulate filter performance.* SAE International Journal of Engines, 2016. **9**(2016-01-0942): p. 1604-1614.

26.   Lambert, C.K., et al., *Analysis of Ash in Low Mileage, Rapid Aged, and High Mileage Gasoline Exhaust Particle Filters.* SAE International Journal of Engines, 2017. **10**(2017-01-0930).

27.   Meng, Z., et al., *Experimental Study on the Influence of DPF Micropore Structure and Particle Property on Its Filtration Process.* Journal of Combustion, 2016. **2016**.

28. Opris, C. and J. Johnson, *A 2-D computational model describing the flow and filtration characteristics of a ceramic diesel particulate trap.* papers.sae.org, 1998.

29. Attfield, M.D., et al., *The diesel exhaust in miners study: a cohort mortality study with emphasis on lung cancer.* Journal of the National Cancer Institute, 2012. **104**(11): p. 869-883.

30. Mathis, U., M. Mohr, and R. Zenobi, *Effect of organic compounds on nanoparticle formation in diluted diesel exhaust.* Atmospheric Chemistry and Physics Discussions, 2004. **4**(1): p. 227-265.

31. Pei, Y.-Q., J. Qin, and S.-Z. Pan, *Experimental study on the particulate matter emission characteristics for a direct-injection gasoline engine.* Proceedings of the Institution of Mechanical Engineers, Part D: Journal of Automobile Engineering, 2014. **228**(6): p. 604-616.

32. Bensaid, S., et al., *Modelling of diesel particulate filtration in wall-flow traps.* Chemical Engineering Journal, 2009. **154**(1): p. 211-218.

33. Bukowiecki, N., et al., *Real-time characterization of ultrafine and accumulation mode particles in ambient combustion aerosols.* Journal of Aerosol Science, 2002. **33**(8): p. 1139-1154.

34. Harris, S. and M. Maricq, *Signature size distributions for diesel and gasoline engine exhaust particulate matter.* Journal of Aerosol Science, 2001. **32**(6): p. 749-764.

35. Saito, C., et al., *New particulate filter concept to reduce particle number emissions*. 2011, SAE Technical Paper.

36. Chan, T.W., et al. *Reducing Particulate Emissions for Future Gasoline Direct Injection Vehicles with a Gasoline Particulate Filter*. in *ETH Conference on Combustion Generated Nanoparticles*. 2012.

37. Ito, Y., et al., *Advanced Ceramic Wall Flow Filter for Reduction of Particulate Number Emission of Direct Injection Gasoline Engines*. 2013, SAE Technical Paper.

38. Parks, J.E., et al., *Filter-based control of particulate matter from a lean gasoline direct injection engine*. 2016, SAE Technical Paper.

39. Richter, J.M., et al., *Application of catalyzed gasoline particulate filters to GDI vehicles*. SAE International Journal of Engines, 2012. **5**(2012-01-1244): p. 1361-1370.

40. Bissett, E., *Mathematical model of the thermal regeneration of a wall-flow monolith diesel particulate filter*. Chemical Engineering Science, 1984. **39**(7-8): p. 1233-1244.

41. Elimelech, M., J. Gregory, and X. Jia, *Particle deposition and aggregation: measurement, modelling and simulation*. 2013: Butterworth-Heinemann.

42. Wang, X., et al., *Particle deposition on the wall driven by turbulence, thermophoresis and particle agglomeration in channel flow*. Proceedings of the Combustion Institute, 2011. **33**(2): p. 2821-2828.

43. Vaden, T.D., et al., *Extending the capabilities of single particle mass spectrometry: I. Measurements of aerosol number concentration, size distribution, and asphericity*. Aerosol Science and Technology, 2011. **45**(1): p. 113-124.

44. Yang, J., et al., *Single wall diesel particulate filter (DPF) filtration efficiency studies using laboratory generated particles*. Chemical Engineering Science, 2009. **64**(8): p. 1625-1634.

45. Rumpf, H. and A. Gupte, *Einflüsse der porosität und korngrößenverteilung im widerstandsgesetz der porenströmung*. Chemie Ingenieur Technik, 1971. **43**(6): p. 367-375.

46.   Johnson, T. and A. Joshi, *Review of Vehicle Engine Efficiency and Emissions*. 2017, SAE International.

47.   Johnson, T. and A. Joshi, *Review of Vehicle Engine Efficiency and Emissions*. 2018, SAE International.

48.   Johnson, T., *Vehicular Emissions in Review*. SAE International Journal of Engines, 2016. **9**(2): p. 1258-1275.

49.   Gong, J. and C.J. Rutland, *Based Heterogeneous Multiscale Filtration Model*. Environmental science & technology, 2015. **49**(8): p. 4963-4970.

50.   Rumpf, H. and A. Gupte, *The influence of porosity and grain size distribution on the permeability equation of porous flow*. NASA STI/Recon Technical Report N, 1975. **75**.

51.   Viswanathan, S., et al., *Experimental investigation of the effect of inlet particle properties on the capture efficiency in an exhaust particulate filter*. Journal of Aerosol Science, 2017. **113**: p. 250-264.

52.   Chen, L., et al., *Characterizing particulate matter emissions from GDI and PFI vehicles under transient and cold start conditions*. Fuel, 2017. **189**: p. 131-140.

53.   Huang, X., et al., *Assembly of large area crack free clay porous films*. RSC Advances, 2018. **8**(2): p. 1001-1004.

54.   Xiayun Huang, N.I., Andrea Strzelec, Nicole Zacharia, *Assembly of Large Area Crack Free Clay Porous Films*. RSC Advances, 2017.

55.   Van Setten, B.A., M. Makkee, and J.A. Moulijn, *Science and technology of catalytic diesel particulate filters*. Catalysis Reviews, 2001. **43**(4): p. 489-564.

56.   Penner, J., C. Chuang, and K. Grant, *Climate forcing by carbonaceous and sulfate aerosols*. Climate Dynamics, 1998. **14**(12): p. 839-851.

57.   Cohen, A.J., et al., *Estimates and 25-year trends of the global burden of disease attributable to ambient air pollution: an analysis of data from the Global Burden of Diseases Study 2015.* The Lancet, 2017. **389**(10082): p. 1907-1918.

58.   Lambert, C., et al., *Gasoline Particle Filter Development.* Emission Control Science and Technology, 2017. **3**(1): p. 105-111.

59.   Chan, T.W., et al., *Characterization of Real-Time Particle Emissions from a Gasoline Direct Injection Vehicle Equipped with a Catalyzed Gasoline Particulate Filter During Filter Regeneration.* Emission Control Science and Technology, 2016. **2**(2): p. 75-88.

60.   Chan, T.W., et al., *Assessment of the fuel composition impact on black carbon mass, particle number size distributions, solid particle number, organic materials, and regulated gaseous emissions from a light-duty gasoline direct injection truck and passenger Car.* Energy & Fuels, 2017. **31**(10): p. 10452-10466.

61.   Yapaulo, R., et al., *Impact of filtration velocities and particulate matter characteristics on diesel particulate filter wall loading.* International Journal of Engine Research, 2009. **10**(5): p. 287-304.

62.   Kamimoto, T., et al., *Light scattering technique for estimating soot mass loading in diesel particulate filters.* International Journal of Engine Research, 2009. **10**(5): p. 323-336.

63.   Merkel, G.A., et al., *Effects of microstructure and cell geometry on performance of cordierite diesel particulate filters*. 2001, SAE Technical Paper.

64.   Gong, J. and C.J. Rutland, *PDF-based Heterogeneous Multiscale Filtration Model.* Environmental science & technology, 2015. **49**(8): p. 4963-4970.

65.   Kočí, P., et al., *3D reconstruction and pore-scale modeling of coated catalytic filters for automotive exhaust gas aftertreatment.* Catalysis Today, 2017.

66.   Izadi, H., et al., *Application of full set of two point correlation functions from a pair of 2D cut sections for 3D porous media reconstruction.* Journal of Petroleum Science and Engineering, 2017. **149**: p. 789-800.

67.   Soyarslan, C., et al., *3D stochastic bicontinuous microstructures: Generation, topology and elasticity.* Acta Materialia, 2018. **149**: p. 326-340.

68.   Feng, J., et al., *Reconstruction of three-dimensional heterogeneous media from a single two-dimensional section via co-occurrence correlation function.* Computational Materials Science, 2018. **144**: p. 181-192.

69.   Yang P., S.A., *Numerical study of pore size and distribution effects on gasoline particulate filter performance.* ECST (Under Review), 2018.

70.   Porter, Q. and A. Strzelec, *Benchtop Investigation of Filtration Efficiency and Pressure Drop Behavior of Commercial High Porosity Gasoline Particulate Filters*. 2019, SAE International.

71.   Inoda, S., et al., *Development of new coating technology optimized for each function of coated GPF*. 2017, SAE Technical Paper.

72.   Tanaka, A., N. Miyoshi, and A. Sato, *Development of Low Pressure and High Performance GPF Catalyst*. 2018, SAE Technical Paper.

73.   Xia, W., et al., *Catalyzed gasoline particulate filter (GPF) performance: effect of driving cycle, fuel, catalyst coating*. 2017, SAE Technical Paper.

74.   Ito, Y., et al., *Next generation of ceramic wall flow gasoline particulate filter with integrated three way catalyst*. 2015, SAE Technical Paper.

75.   Richter, J.M., et al., *Application of catalyzed gasoline particulate filters to GDI vehicles.* SAE International Journal of Engines, 2012. **5**(3): p. 1361-1370.

76. Lambert, C.K., et al., *Analysis of ash in low mileage, rapid aged, and high mileage gasoline exhaust particle filters.* SAE International Journal of Engines, 2017. **10**(2017-01-0930): p. 1595-1603.

77. Jorgensen, J., et al. *The effect of ash accumulation on gasoline particulate filters: a comparison between laboratory and field aged samples.* in *ASME 2014 Internal Combustion Engine Division Fall Technical Conference*. 2014. American Society of Mechanical Engineers.

78. Custer, N., et al., *Lubricant-derived ash impact on gasoline particulate filter performance.* SAE International Journal of Engines, 2016. **9**(3): p. 1604-1614.

79. Sappok, A., et al., *Theoretical and experimental analysis of ash accumulation and mobility in ceramic exhaust particulate filters and potential for improved ash management.* SAE International Journal of Fuels and Lubricants, 2014. **7**(2): p. 511-524.

80. Liu, X., et al., *Gasoline Particulate filter efficiency and backpressure at very low mileage*. 2018, SAE Technical Paper.

81. Sappok, A., S. Munnis, and V.W. Wong. *Individual and synergistic effects of lubricant additive components on diesel particulate filter ash accumulation and performance*. in *ASME 2012 Internal Combustion Engine Division Spring Technical Conference*. 2012. American Society of Mechanical Engineers.

82. Morcos, M., P. Ayyappan, and T. Harris, *Characterization of dpf ash for development of dpf regeneration control and ash cleaning requirements*. 2011, SAE Technical Paper.

83. Konstandopoulos, A., et al., *Fundamental studies of diesel particulate filters: transient loading, regeneration and aging.* papers.sae.org, 2000.

84.   Pozzato, G., M.A. Hoffman, and S. Onori. *Multi-channel physics-based modeling and experimental validation of an uncoated Gasoline Particulate Filter in clean operating conditions*. in *American Control Conference (ACC), 2017*. 2017. IEEE.

85.   Liu, Y., et al., *Nanoparticle motion trajectories and deposition in an inlet channel of wall-flow diesel particulate filter*. Journal of Aerosol Science, 2009. **40**(4): p. 307-323.

86.   Piscaglia, F., C.J. Rutland, and D.E. Foster, *Development of a CFD model to study the hydrodynamic characteristics and the soot deposition mechanism on the porous wall of a diesel particulate filter*. 2005, SAE Technical Paper.

87.   Piscaglia, F., et al., *Multi-dimensional modeling of the soot deposition mechanism in diesel particulate filters*. SAE International Journal of Fuels and Lubricants, 2009. **1**(1): p. 210-230.

88.   Opris, C.N. and J.H. Johnson, *A 2-D computational model describing the flow and filtration characteristics of a ceramic diesel particulate trap*. 1998, SAE Technical Paper.

APPENDIX

User Defined Function (UDF) allows users to integrate custom design C code into FLUENT solver so as to achieve certain functions that are not preset in FLUENT. FLUENT uses either the in-house compiler or third party complier to compile and debug the C code before it can be called by the solver.

In this study, 3D GPF simulations are conducted to investigate the wall heterogeneity effects. The filtration efficiency of injected particles need to be solved. UDF is a must tool for this study since FLUENT itself does not possess capability of simulating particle filtration. UDF is also implemented to define and update the GPF wall properties. Initial wall porosity and permeability profiles on axial direction are assigned by UDF. UDF is responsible to update the wall permeability at each time step, which has direct impact on the channel flow field in the next time step. Therefore, the correct and efficient application of UDF is crucial.

Three major type of UDF functions (Macros) are used in this study. "DEFINE_SOURCE(Source_X,c,t,dS,eqn)" is used to define properties of the sample GPF porous wall. Here in this study, permeability is the target wall property to define and monitor throughout the simulation. "DEFINE_DPM_PROPERTY(carbon_density,c,t,p,T)" is a Macro that can define particle properties (density) prior to injection. For typical GDI particulates at size of 75nm, they are proven to be aggregations of numerous small particulates. This particulate cluster thus has a lower density than a single carbon particulate. Last but not the least, "DEFINE_DPM_PROPERTY(carbon_density,c,t,p,T)" is the core of this UDF. This Macro allows FLUENT solver to record all the particle and local flow data when particles hit the porous

wall. Then user can access all these data as filtration model inputs. FLUENT solver will take care

of the rest of filtration efficiency calculation.

The flowchart listed in **Figure 79** demonstrates the major functions of the UDF in transient
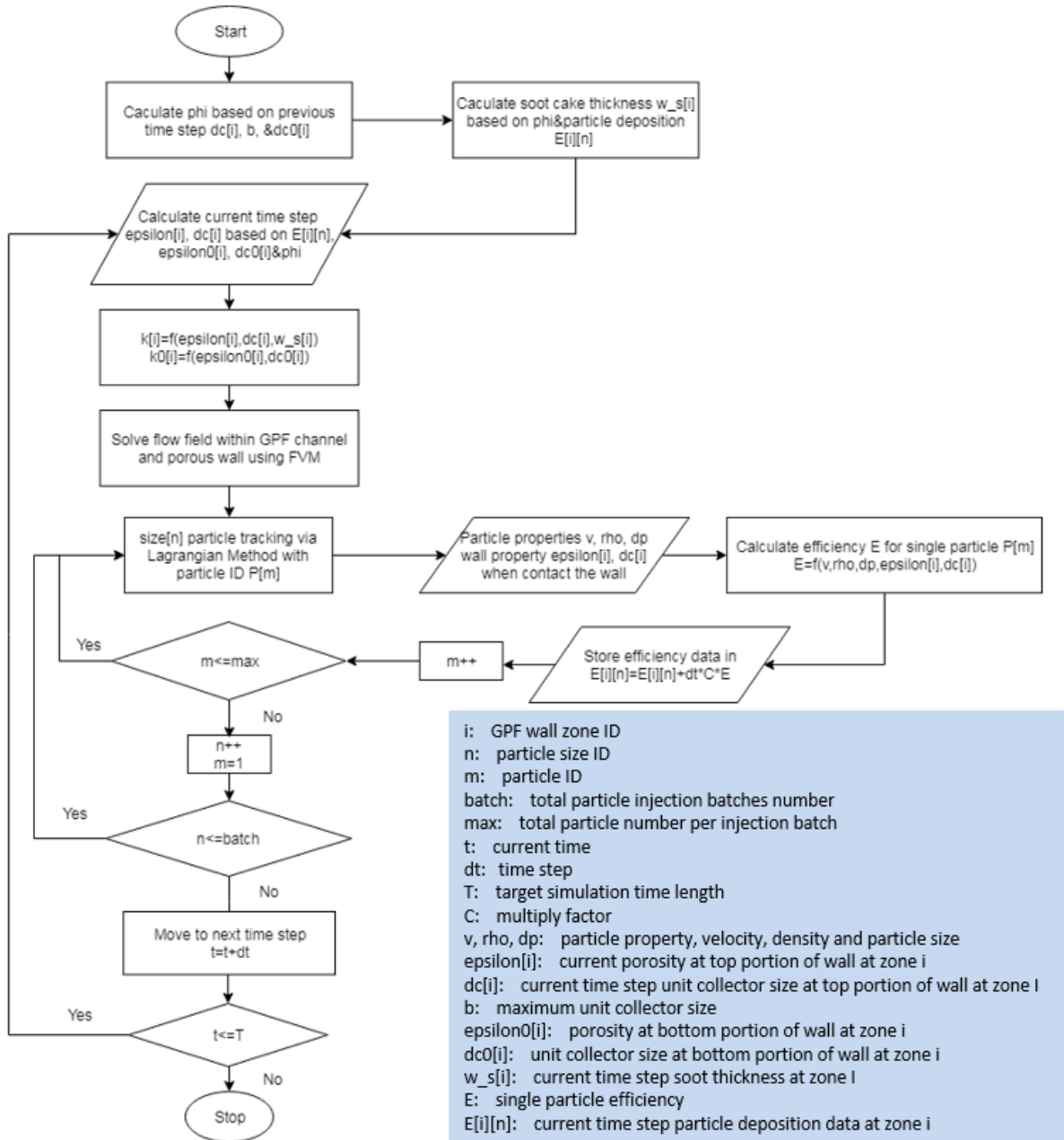
GPF simulation.

Figure 79. The UDF flowchart demonstrating its functionalities.